
This item was submitted to [Loughborough's Research Repository](#) by the author.
Items in Figshare are protected by copyright, with all rights reserved, unless otherwise indicated.

Brillouin and neutron scattering study of hexagonal ABX₃ ternary halides

PLEASE CITE THE PUBLISHED VERSION

PUBLISHER

© Dayang Maryani Awang Hashim

LICENCE

CC BY-NC-ND 4.0

REPOSITORY RECORD

Hashim, Dayang M.A.. 2019. "Brillouin and Neutron Scattering Study of Hexagonal ABX₃ Ternary Halides".
figshare. <https://hdl.handle.net/2134/12085>.

This item was submitted to Loughborough University as a PhD thesis by the author and is made available in the Institutional Repository (<https://dspace.lboro.ac.uk/>) under the following Creative Commons Licence conditions.



For the full text of this licence, please go to:
<http://creativecommons.org/licenses/by-nc-nd/2.5/>

LOUGHBOROUGH
UNIVERSITY OF TECHNOLOGY
LIBRARY

AUTHOR/FILING TITLE

HASHIM, D.W.A.

ACCESSION/COPY NO.

040116986

VOL. NO.

CLASS MARK

26 ... 1998

26 JUN 1998

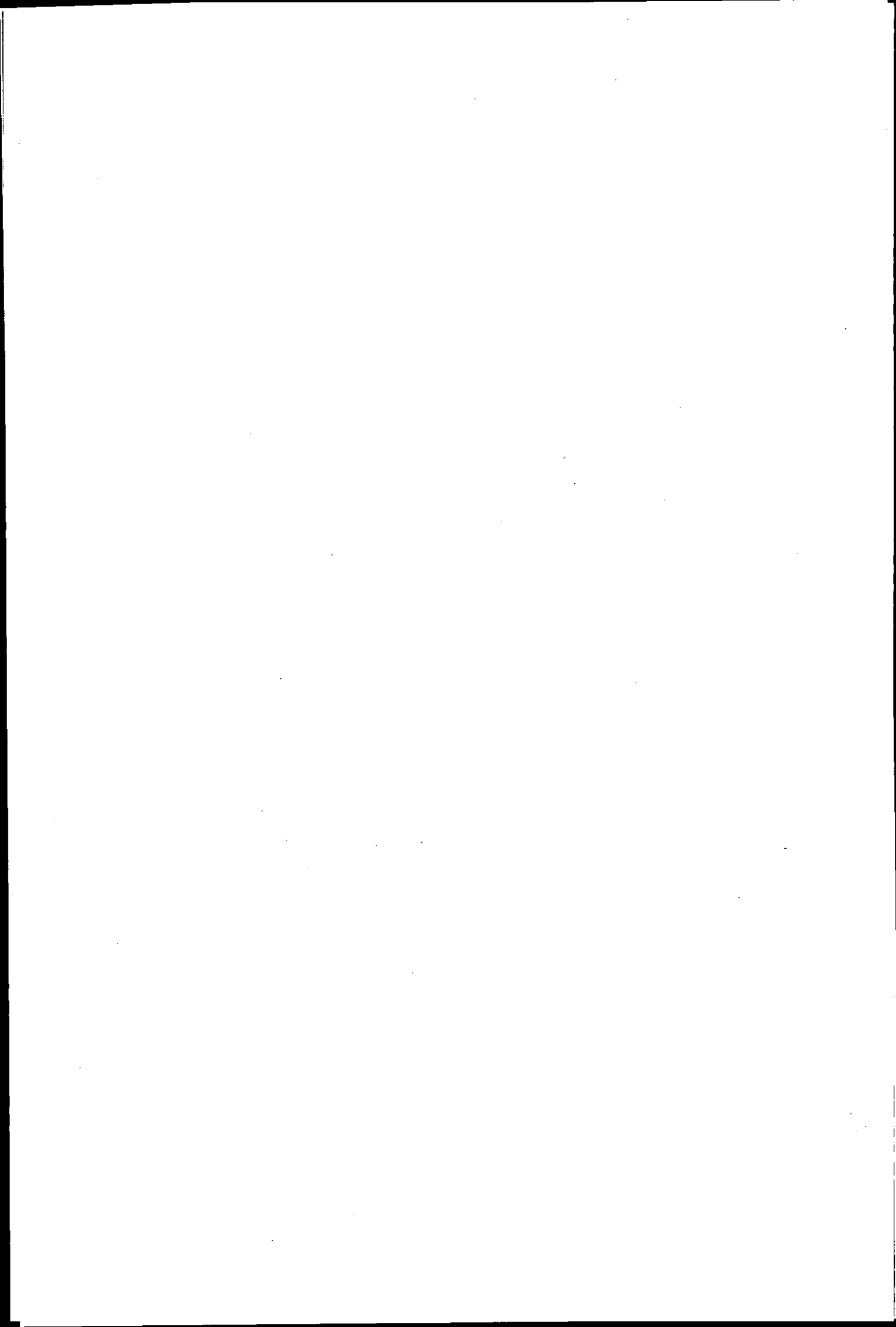
25 JUN 1999

LOAN COPY

0401169863



BADMINTON PRESS
18 THE HALFCROFT
SYSTON
LEICESTER LE7 1LD
ENGLAND



BRILLOUIN AND NEUTRON SCATTERING STUDY
OF
HEXAGONAL ABX₃ TERNARY HALIDES

BY

DAYANG MARYANI AWANG HASHIM

A Doctoral Thesis Submitted in Partial Fulfilment of the Requirements for the
Award of a Doctor Philosophy at Loughborough University of Technology

August 1995

© by Dayang Maryani Awang Hashim

Loughborough University of Technology Library	
Date	Jan 96
Class	
Acc. No.	040116986

9/3091629

بِسْمِ اللَّهِ الرَّحْمَنِ الرَّحِيمِ

IN THE NAME OF ALLAH THE MOST BENEFICIENT THE MOST
MERCIFUL

DEDICATION

To my husband Dr. Sinin Hamdan and children Saifuliwan Ezzedin and
Aaliyawani Ezzerin for all the sacrifices that they made in favour of my
education

♥♥♥♥

Acknowledgements

I would like to express my deepest thanks to Dr. D. Visser and Dr. R.T. Giles for the friendship and guidance throughout the whole period of my study in the Physics Department and I have thoroughly enjoyed it.

A very special thanks goes to Dr. G M Swallowe for his help and comments in performing the DSC experiments and also to Prof. K.R.A. Ziebeck for his advice.

I would like to thank the Hahn-Meitner Institute, Berlin, Germany for the opportunity to use the facilities available for neutron scattering experiments and also to Dr. A. Krimmel who made this work possible and my stay in Berlin enjoyable.

Thank you to all the Physics Department staff for their cooperation and understanding during my stay at the department and not least to my colleagues.

Lastly, to The Government of Malaysia and Universiti Pertanian Malaysia for being my sponsor throughout my study.

ABSTRACT

The interest in one dimensional (1D) magnetism has been strongly renewed with the synthesis of many magnetic compounds which exhibit a quasi one dimensional magnetic behaviour. One of the peculiarities of this 1D system is the absence of a long range magnetic ordered phase at any finite temperature for the ideal 1D system with short range interaction.

Tetramethylammonium manganese chloride ($(\text{CH}_3)_4\text{NMnCl}_3$ (TMMC) exhibits the properties of an ideal one dimensional antiferromagnets for temperature above 1K, the transition to a three dimensional (3D) long range ordered state only occurs at 0.84K. In addition to its magnetic transition, TMMC exhibits structural phase transition due to the ordering of the tetramethylammonium (TMA) ions which makes also this compound very attractive from a lattice dynamical point of view.

Structural phase transitions of tetramethylammonium manganese chloride (TMMC), tetramethylammonium manganese bromide (TMMB) and tetramethylammonium manganese chloride doped with 8% Cu (TMMC:Cu) of the hexagonal type compounds are investigated using the Brillouin scattering method. These crystals show pronounced acoustic anomalies in the region of the structural phase transition. The acoustic anomalies were observed by measuring sound velocity and hence the elastic constant can be deduced. The phase transition temperatures were observed at 129.6K and 388.6K (TMMC), 114.6K and 377.6K (TMMB) and at 108.6K and 359.6K (TMMC:Cu). The elastic constant at room temperature were $C_{11} = 2.10$ (TMMC) and $C_{11} = 1.59$ (TMMB) in units of 10^{10} Nm^{-2} .

The phase transition of these compounds were further investigated macroscopically using the Differential Scanning Calorimetry (DSC) method. Activation energies of TMMC, TMMC:Cu, TMMB and deuterated TMMB at the phase transition were determined using this method. The values are 70.612 kJ/mol (TMMC), 49.224 kJ/mol (TMMC:Cu), 51.747 kJ/mol (TMMB) and 69.909 kJ/mol (d_{12} -TMMB).

The elastic constant of the linear chain antiferromagnet CsNiCl_3 and RbNiCl_3 was also determined using the Brillouin scattering method. The room

temperature measurements give $C_{11} = 3.77$ (3.71) and $C_{33} = 5.62$ (5.42) in units of 10^{10} Nm^{-2} for CsNiCl_3 and RbNiCl_3 respectively.

The phonon dispersion curves at room temperature in the hexagonal CsFeBr_3 have been studied using the inelastic neutron scattering technique. From the initial slope of the dispersion curve, the sound velocity was deduced which enable us to calculate the elastic constant of CsFeBr_3 at room temperature. The values obtained are $C_{11} = 7.33$, $C_{66} = 1.01$, $C_{33} = 2.58$ and $C_{44} = 0.56$ in units of 10^{10} Nm^{-2} .

BRILLOUIN AND NEUTRON SCATTERING STUDY OF HEXAGONAL ABX₃ TERNARY HALIDES

CONTENTS

ABSTRACT

CHAPTER 1 Background

	page
1.0 Introduction	1
1.1 General aspects of the structural phase transition	1
1.2 The Landau theory of phase transition	4
1.3 Phonons	5
1.4 Outline of the thesis	6

CHAPTER 2

The ABX₃ Compounds

2.1 Introduction	8
2.2 Phase transition of the TMMC-type crystals	9
2.3 Structure and properties of RbNiCl ₃ and CsNiCl ₃	14
2.4 The AFeX ₃ compounds	17
2.4.1 Crystal structure and magnetic properties of CsFeBr ₃ and related materials	17

CHAPTER 3

Brillouin scattering

3.0	Introduction	19
3.1	Energy and momentum conservation	20
3.2	Theory of the Fabry-Perot Interferometer	23
3.3	The development of the Brillouin scattering spectrometer	27
3.4	Brillouin scattering apparatus	34
3.4.1	The triple pass interferometer	34
3.4.2	The light source	35
3.4.3	Detectors	37
3.4.4	Vibration isolation	37
3.4.5	The cryogenics system	38
3.5	Alignment for the back-scattering configuration	41
3.6	Alignment of the optical system	41
3.7	Stabilising the Fabry-Perot	47
3.8	Brillouin scattering as a tool for the measurement of elastic and photoelastic constant	47
3.9	Experimental procedure	49
3.10	The spectrum	50
3.11	Results	54
3.11.1	TMMC, TMMB and TMMC:Cu	54
3.11.2	RbNiCl ₃ and CsNiCl ₃	73

CHAPTER 4

Differential Scanning Calorimetry

4.0	The differential scanning calorimetry-DSC	83
4.1	Introduction	83
4.2	Measuring principle	84
4.3	Theory	86

4.4 DSC measurement	89
4.5 Results	91

CHAPTER 5

Neutron scattering

5.0 Neutron scattering	107
5.1 Introduction	107
5.2 Neutron scattering theory	108
5.3 Neutron cross-section	111
5.4 Scattering by phonons	113
5.5 The triple axis spectrometer	114
5.6 The E7 triple axis spectrometer at HMI-Berlin	117
5.7 Experimental methods	119
5.8 Results	121
5.8.1 Longitudinal acoustic (LA) [001]	122
5.8.2 Transverse acoustic (TA) [001]	122
5.8.3 Longitudinal acoustic (LA) [110]	122
5.8.4 Transverse acoustic (TA) [110]	122

CHAPTER 6

Discussion

Discussion	150
Conclusion	158

References	160
-------------------	------------

CHAPTER 1

BACKGROUND

1.0 Introduction:

1.1 General aspects of the structural phase transitions:

The study of phase transitions, both theoretically and experimentally have found widespread interest among physicists during the past few years. Phase transitions are now appreciated to be of fundamental importance in the study of all condensed matter, whether it be insulating crystals, semiconductors, metals or polymers and other non-crystalline substances.

Structural phase transitions occur when a material changes its crystallographic structure. The first studies of these transitions were measurements of macroscopic properties; specific heat, dielectric susceptibility or thermal expansion. It was through these measurements that the transitions were discovered and initially characterised. Because the macroscopic properties change at the transition, their study is of importance for the various different applications of these materials. For example the ferroelectrics can be used as piezoelectric components and as pyroelectric detectors [Cowley 1981]. There has also been a great deal of effort devoted to explaining the nature of structural phase transitions at a more microscopic level. This work began with the careful determination of the crystal structure of the phases on both sides of the transition.

Figure 1.1 shows the low temperature phase of the cubic perovskite BaTiO_3 . At $T < 393\text{K}$ the Ti and O atoms are displaced away from the centrosymmetric position that they occupy in the high temperature cubic phase [Harada 1970]. In ferroelectric BaTiO_3 , the static displacements of the atoms in every unit cell of the distorted phase are the same and the unit cell retains approximately the same volume. At other structural phase transitions the unit cells in the distorted phase consist of two, four or maybe more unit cells of the high temperature phase. An example of this type of transition is the structure of SrTiO_3 below the transition at 110K

(see Figure 1.2). In this case, the high temperature perovskite phase is distorted by an anti-phase rotation of neighbouring oxygen octahedra resulting in an enlargement of the unit cell size [Unoki 1967].

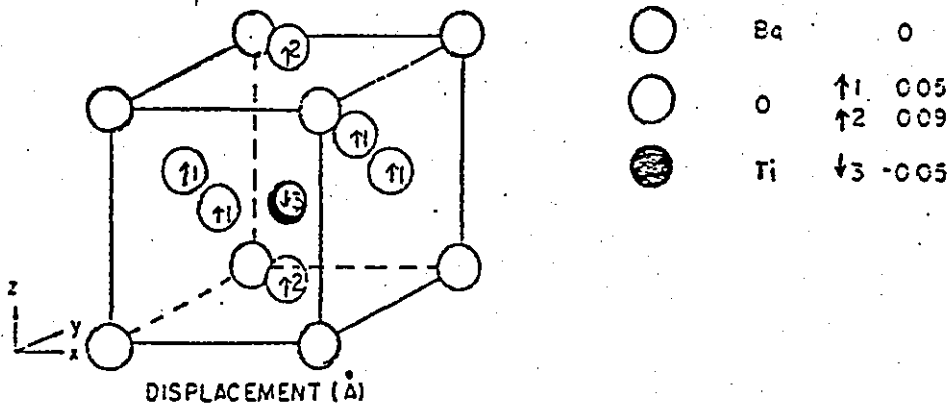


Fig. 1.1 The distorted perovskite structure of BaTiO₃

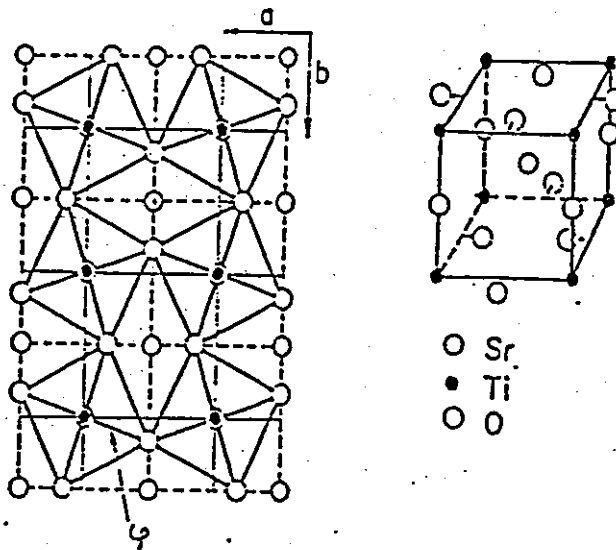


Fig. 1.2: A projection down a cube axis of the distorted phase of SrTiO₃ as deduced by Unoki [after Shirane1969].

These measurements showed that at least in some structural phase transitions, the atoms in the distorted phase are slightly displaced away from the equilibrium positions of the high temperature phase. Cochran [1960] suggested that these phase transitions might be the result of an instability of the crystal against a particular normal mode of vibration of the

high temperature phase. Since then, there has been numerous measurements of the so called 'soft-modes' associated with structural phase transitions [Scott 1974, Shirane 1974] and at least for these 'displacive' phase transition their existence is well established.

Other structural phase transitions are associated with an ordering of some variable that is disordered in the high temperature phase. An example of this 'order-disorder' type of behaviour is the ferroelectric phase transition in NaNO_2 . In the high temperature phase (paraelectric), the triangular NO_2 groups have the N ions along either the positive or negative b-axis with equal probability, but below 436K the N ion tends to align in the same direction as shown in Figure 1.3 [Hoshino & Montegi 1974]. The TMMex_3 compounds studied in this thesis falls into both categories.

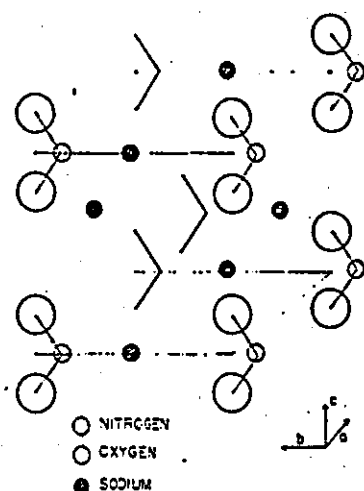


Fig. 1.3: The structure of ferroelectric NaNO_2 [after Sakurai et. al. 1970].

The simplest theory of structural phase transition is Landau's (1937) phenomenological theory. Landau theory involves a considerable number of parameters which at the phenomenological level, must be obtained from the experimental measurements.

1.2 The Landau theory of phase transition:

In 1937, Landau developed a theory of phase transitions that he applied to structural phase transitions. Landau assumes that the free energy of one unit cell of the crystal may be expanded in powers of η as follows: [Landau & Lifshitz 1959]

$$G = G_0 + \frac{1}{2}r\eta^2 + d\eta^3 + u\eta^4 \quad \text{.....1.1}$$

where G_0 is the free energy of the high temperature form, η is the order parameter, r , d and u are temperature independent coefficients.

A phase is stable only if

$$\left. \frac{\partial G}{\partial \eta} \right|_{\eta_0} = 0 \quad \left. \frac{\partial^2 G}{\partial \eta^2} \right|_{\eta_0} > 0 \quad \text{.....1.2}$$

The high symmetry phases $\langle \eta \rangle = \eta_0 = 0$ is then stable only if r is positive. The system is distorted if r is negative.

At a continuous phase transition G must increase with $|\eta|$ at T_c , $r=0$, so that $d=0$ and $u>0$. Landau's theory is then completed by the further assumptions that since r changes sign at T_c it can be written as an analytic function of T near T_c .

$$r = a(T - T_c) \quad \text{.....1.3}$$

The coefficient u is assumed to be independent of temperature for temperatures sufficiently close to T_c . The free energy of the simplest model then becomes

$$G = G_0 + 1/2a(T - T_c)\eta^2 + u\eta^4 \quad \text{.....1.4}$$

The stability conditions for the low temperature phase for $T < T_c$ is that the order parameter will have the value

$$\eta_0^2 = \frac{a}{4u}(T_c - T) \quad \text{...1.5}$$

while the free energy for the equilibrium displacement is given by

$$G_s = \langle G \rangle = G_0 - \frac{a^2}{16u}(T_c - T) \quad T < T_c \quad \text{.....1.6}$$

and consequently the change in specific heat is given by

$$\begin{aligned} \bar{C} &= -T \frac{\partial^2 G}{\partial T^2} = \frac{a^2 T}{8u} & T < T_c & \quad \text{.....1.7} \\ &= 0 & T > T_c & \end{aligned}$$

In equation 1.4 it was assumed that $d=0$; this is always the case when there is only one component of the order parameter, but it is not necessarily the case for a multicomponent system. When d is non zero, the transition is of first order; nevertheless, in many systems the transition is nearly continuous and the phase transition can be analysed using the Landau expansion.

1.3 Phonons:

Many interesting physical effects associated with the propagation of elastic waves arise from the quantization of their energy. The quantum of

energy in an elastic wave is called a phonon. Experimental evidence for phonons includes:

a. The lattice contribution to the heat capacity of solids can only be explained if the lattice oscillators are quantized. The lattice heat capacity always approaches zero as the temperature approaches zero. This observation was the earliest evidence for phonons, and it can be explained only if the oscillator energy is quantized.

b. X-rays and neutrons can be scattered inelastically by crystals, with energy and momentum changes corresponding to the creation or absorption of one phonon. By measuring the recoil of the scattered X-ray or neutron, the dynamical properties of individual phonons can be determined. Such experiments offer the best way of determining the dispersion relations of frequency versus wave vector for phonons, and is the strongest evidence for the existence of phonons.

c. In optical absorption by impurities in insulating crystals it is sometimes possible to see a structure of multiple spikes that accompanies the main absorption line. These discrete spikes may be interpreted consistently as arising from the emission of a number of phonons.

1.4 Outline of the thesis:

In this thesis we investigate structural phase transitions in some ABX_3 ternary halides which crystallise with the hexagonal perovskite structure. The $TMMex_3$ compounds show two types of phase transition (i) a second order phase transition at high temperature which is of the order-disorder type (ii) a first order phase transition at lower temperature which is of the displacive type as well as order-disorder type.

The influence of Cu doping, the introduction of Jahn-Teller active centres, the structural phase transition has been investigated. These phase transitions are characterised macroscopically by Differential Scanning Calorimetry (DSC) measurements (Chapter 4).

The microscopic characterisation of these phase transitions have been carried out by Brillouin scattering (temperature dependence), from which one derives the elastic constants in the principal directions of the Brillouin zone (Chapter 3).

The temperature dependence of the principal elastic constant C_{11} and C_{33} of the hexagonal perovskite CsNiCl_3 and RbNiCl_3 which show no structural phase transition have been determined too as a comparison with the TMMeX_3 compounds (Chapter 3).

Inelastic neutron scattering experiments on the hexagonal perovskite CsFeBr_3 have been carried out too. The dispersion curves of the longitudinal acoustic (LA) and transverse acoustic (TA) phonons were determined at room temperature. The elastic constant have been evaluated too. (Chapter 5)

A general overview of the properties of the hexagonal perovskite which are relevant in the thesis are provided in Chapter 2.

In the final discussion of the results obtained by the different characterisation methods, the complementarity of the methods involved is elaborated and the temperature dependent behaviour of the elastic constants are related to other physical measurements like magnetic susceptibility, phase comparison method (sound wave) and dilatation measurement.

CHAPTER 2

The ABX_3 compounds

2.1 Introduction:

Due to the rich variety of magnetic phases and potential for theoretical insight, there has been considerable and on going interest in the properties of quasi one-dimensional hexagonal magnetic materials with the formulae ABX_3 [Hatfield et. al. 1983, Steiner et. al. 1976, Harisson & Visser 1992]. Here A is a univalent cation, B is a magnetic transition metal ion, and X is a halide ion. These materials form linear chains of face-sharing BX_3 octahedra, which results in interesting magnetic anisotropy at low temperature. A variety of experimental studies have been carried out on the magnetic properties of these materials in an effort to accumulate a wide body of knowledge, and thus provide a theoretical proving ground for all sorts of aspects of linear magnetic chains systems [Affleck 1989].

Work has also focused on the nature of the structural phase transitions in some of the ABX_3 materials which generally take place between 700 and 30K. In many compounds, the phase transition is considered to be displacive in nature, related to unit cell doubling or structural distortions [Peercy et. al. 1973, Braud et. al. 1990, Visser et. al. 1989, Tsang & Utton 1976]. In materials with large polyatomic cations, transitions often of the order-disorder type are often driven by the ordering of these ions [Peercy et. al. 1973, Tsang & Utton 1976]. Furthermore, significant differences have been observed in the behaviour of chemically similar compounds; whilst interesting, such differences add a further level of complexity to the study of structural phase transitions in the ABX_3 materials [Berg & Skaarup 1978, Harrison et. al. 1991]. Consequently, despite previous studies on a wide variety of compounds, the nature of these structural phase transitions is not well understood.

2.2 Phase transitions of the TMMC-type crystal:

Tetramethylammonium first row transition metal trihalides compounds which have the common chemical formulae of $N(CH_3)_4MX_3$ (M:divalent metal, Mn, Ni, Cd, Cu, V, Pb; X:halogen, Cl, Br, I) have been known as quasi one-dimensional magnetic materials, and lots of investigations have been done with respect to their magnetic properties and magnetic phase transitions both experimentally and theoretically [Ackerman et. al. 1974, Renard et. al. 1987].

At room temperature most of these types of compounds crystallise with the hexagonal $P6_3/m$ ($Z=2$) structure (Phase I) [Morosin & Graeber 1967]. The structure is schematically shown in Figure 2.1.

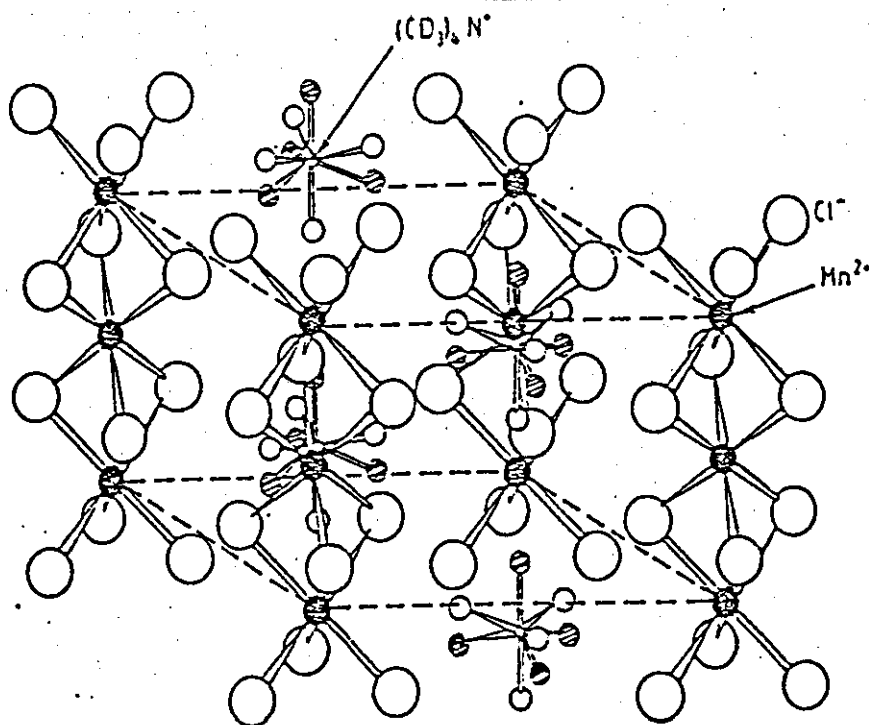


Fig. 2.1: Crystal structure of TMMC at room temperature [after Stucky 1968]

There are linear chains of MX_6 octahedra along the c-direction in which the adjacent octahedra commonly share one face. The $\text{N}(\text{CH}_3)_4$ ions that locate in the spaces between the MX_6 -octahedra chains, show an orientational disorder. In the structure shown in Figure 2.1, two orientations of the $\text{N}(\text{CH}_3)_4$ ions are occupied with equal probability. Recent studies, however have proposed a more complicated disorder model for the $\text{P6}_3/\text{m}$ structure of the TMMC-type compounds [Braud et. al. 1990].

In some compounds, the room temperature phases (phase I) transform to a prototypic structure of $\text{N}(\text{CH}_3)_4$ ions (phase I') at some elevated temperatures, at 389K (TMMC), 400K (TMCC) and 390K (TMCB) [Braud et. al. 1990, Levola & Laiho 1986, 1988]. The transition from phase I to I' is thought to be of second order [Braud et. al. 1990]. As the temperature is lowered, the TMMC-type crystals undergo structural phase transitions, and transform to the ordered structures of $\text{N}(\text{CH}_3)_4$ ions. The low temperature structural transitions and the structures of the ordered phases vary between among the compounds.

To date, the most extensive studies have been concerned with the crystal structures and the structural transitions of these compounds. Two structural phase transitions have been reported for TMMC at 398K and 126K [Braud et. al. 1990, Hutchings et. al. 1972, Peercy et. al. 1973, Levola & Laiho 1986]. The room temperature phase (phase I) of TMMC belongs to the hexagonal $\text{P6}_3/\text{m}$ structure ($Z=2$) with lattice constant $a=9.151 \text{ \AA}$ and $c=6.494 \text{ \AA}$ [Morosin & Graeber 1967]. In phase I', stable above 398K, the crystal structure is hexagonal $\text{P6}_1/\text{mmc}$ ($Z=2$), and the TMA ions are in another complicated disordered state [Braud et. al. 1990]. The lowest temperature phase (II) stable below 126K belongs to the monoclinic $\text{P2}_1/\text{b}$ structure. The b-lattice parameter of phase II is doubled ($Z=4$) in comparison with that of phase I [Braud et. al. 1990, Peercy et. al. 1973, Hutchings et. al. 1972]. The transition from phase I to II is promoted by an ordering process of the TMA ions. An additional transition at 40K has been suggested from a change in the proton NMR spectrum [Mangum & Utton 1972] but this transition was not confirmed by specific heat measurement [Dunn et. al. 1983].

The room temperature structures of TMMB, TMNC and TMNB were reported to be hexagonal $P6_3/m$ [Stucky 1968, Peercy et. al. 1973]. Structural phase transitions were reported at 144K (TMMB), 171K (TMNC) and 133K (TMNB) [Alcock & Holt 1978, Visser et. al. 1989, Peercy et. al. 1973, Kakurai et. al. 1990]. The lattice constant for TMMB at room temperature is $a=9.4142\text{\AA}$ and $c=6.7768\text{\AA}$ [Alcock & Holt 1978]. Alcock reported that for TMMB at the phase transition, the crystal lattice remains hexagonal only lowering its symmetry from $P6_3/m$ to $P6_3$, while the unit cell dimensions stay the same. However, a neutron scattering experiment on d_{12} -TMMB has shown that the symmetry of the low temperature phase is also monoclinic [Visser et. al. 1989]. The structural phase transition in TMMB has also been observed by magnetic susceptibility [Visser 1986] which show a distinct difference in behaviour at the phase transition between TMMC and TMMB.

There are two low temperature phase transitions at 118K and 104K in TMCC [Braud et. al. 1990, Peercy et. al. 1973, Mlik & Couzi 1982, Couzi & Mlik 1986, Tsang & Utton 1976]. The crystal structure of the intermediate II phase is reported to be monoclinic $P2_1/m$ without cell multiplication ($Z=2$) [Braud et. al. 1990, Peercy et. al. 1973]. According to recent work [Braud et. al. 1990], the lowest temperature phase III is of monoclinic $P2_1/b$ with a doubling of the b-lattice spacing and a tripling of the c-lattice spacing ($Z=12$). A new type of disordered state of $N(CH_3)_4$ ions is developed in phase II, while the completely ordered state is found in phase III [Braud et. al. 1990, Mlik & Couzi 1979].

The structural phase transitions in TMCuC are complicated because of the Jahn-Teller distortion of CuCl-octahedra [Haije & Maaskant 1988, Visser et. al. 1989]. At room temperature, TMCuC crystallise in the monoclinic $P2_1$ structure (phase III) with a quintupling of the c-lattice spacing ($Z=10$) in comparison with that of the prototypic hexagonal $P6_3/mmc$ structures [Haije & Maaskant 1988]. Above room temperature phase III transforms at 319K to another monoclinic structure of symmetry C_2/m ($Z=2$)(phase II) [Willet et. al. 1988]. The highest temperature phase that is stable above 373K is the prototypic hexagonal structure $P6_3/mmc$ (phase I') differing from the $P6_3/m$ structure that is commonly found in other TMMC-type compounds.

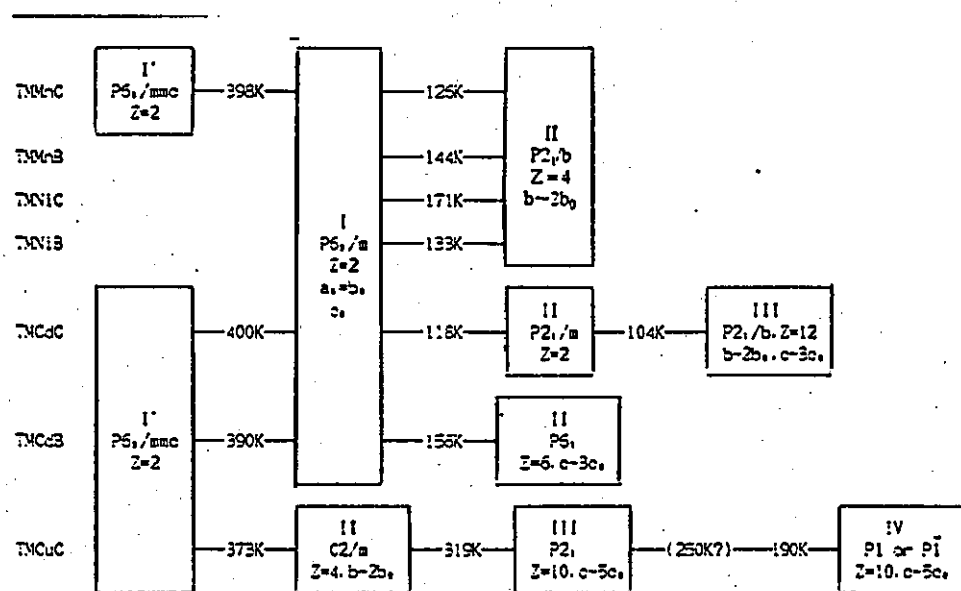
The order-disorder change in Jahn-Teller distortions of the CuCl_6 -octahedra and in the orientations of $\text{N}(\text{CH}_3)_4$ ion takes place successively and this corresponds to the complicated transition sequence in TMCuCl_3 [Haije et. al. 1988, Willet et. al. 1988, Visser et. al 1989]. In phase I' of TMCuCl_3 , both the Jahn-Teller distortions of CuCl_6 and the orientations of $\text{N}(\text{CH}_3)_4$ ions are fully distorted. In phase II, the $\text{N}(\text{CH}_3)_4$ ions are still disordered. At room temperature phase III is characterised by fully ordered Jahn-Teller distortions together with orientational disorder of the $\text{N}(\text{CH}_3)_4$ ions. In phase IV, both the Jahn-Teller distortions and the orientation of $\text{N}(\text{CH}_3)_4$ ions are ordered.

In Table 2.1 the room temperature structures and unit cell parameters of TMMC-type compounds are listed. In Table 2.2, the reported successive phase transitions sequence in TMMC-type compounds are shown.

Table 2.1: Room temperature structures and unit cell parameters of TMMC-type compounds

Compound	Space group	Unit cell parameters Å	Z	Reference
$\text{N}(\text{CH}_3)_4\text{MnCl}_3$ (TMMC)	$P6_3/m$	$a=9.151$ $c=6.490$	2	Braud 1990
$\text{N}(\text{CH}_3)_4\text{MnBr}_3$ (TMMB)	$P6_3/m$	$a=9.44$ $c=6.76$	2	Alcock 1978
$\text{N}(\text{CH}_3)_4\text{NiCl}_3$ (TMNC)	$P6_3/m$	$a=9.019$ $c=6.109$	2	Stucky 1968
$\text{N}(\text{CH}_3)_4\text{NiBr}_3$ (TMNB)	$P6_3/m$	$a=9.35$ $c=6.35$	2	Stucky 1966
$\text{N}(\text{CH}_3)_4\text{CdCl}_3$ (TMCdC)	$P6_3/m$	$a=9.139$ $c=6.723$	2	Braud 1990
$\text{N}(\text{CH}_3)_4\text{CdBr}_3$ (TMCdB)	$P6_3/m$	$a=9.404$ $c=6.990$	2	Asahi 1990
$\text{N}(\text{CH}_3)_4\text{CuCl}_3$ (TMCuCl_3)	$P2_1$	$a=9.151$ $b=6.095$ $c=32.390$ $\gamma=120.04$	10	Weenk 1976
$\text{N}(\text{CH}_3)_4\text{CrCl}_3$ (TMCrC)	$P6_3/m$	$a=9.129$ $c=6.512$	2	Bellitto 1984

Table 2.2: Structural phase transition in TMMC-type compounds.



RbNiCl₃ and CsNiCl₃

2.3 Structure and properties of RbNiCl₃ and CsNiCl₃

In hexagonal $ABCl_3$ -type compounds, in which A is represented by Cs or Rb, and B by Cu, Ni, Co or Fe, the space group is $P6_3/mmc$ except for $CsCuCl_3$ which has the space group $P6_1/2$ [Achiwa 1969]. Shown in Figure 2.2 is their crystal structure.

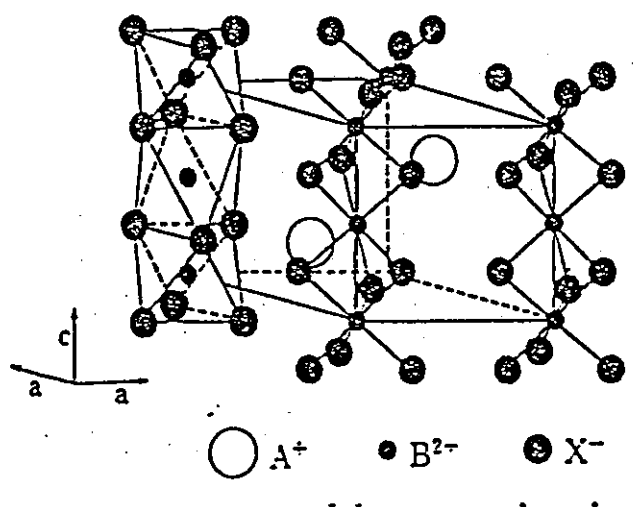


Fig. 2.2: Crystal structure of hexagonal $ABCl_3$ -type compounds where A:Cs⁺ or Rb⁺ and B:Cu²⁺, Co²⁺, Fe²⁺, Ni²⁺ or Mg²⁺.

In this structure, A ions and Cl ions form a hexagonal closed packed lattice and B ions occupy the octahedral interstices surrounded by six Cl ions, making a simple hexagonal lattice. Along the hexagonal c-axis, (BCl_6) octahedra share faces which makes infinite chains. Two kinds of exchange interaction should be considered in these compounds; one is the intrachain super exchange interaction J between the nearest neighbour magnetic ions along the c-axis, and the other is the interchain super exchange interaction J' through B-Cl-Cl-B path between linear chains, as shown in Figure 2.2.

Another important feature is the arrangement of magnetic B^{2+} ions, which form a triangular lattice in the c-plane. Since the interchain interaction is

anti ferromagnetic in almost all of the compounds, the present system is also regarded being 2D anti ferromagnetic triangular lattice. Thus, the magnetic ordering process is more or less under the influence of spin frustration.

CsNiCl_3 and RbNiCl_3 is an Ising-like Heisenberg antiferromagnet on a triangular lattice. Successive phase transitions and anomalous behaviour of some physical quantities in relation to the phase transition have been observed in many hexagonal ABX_3 antiferromagnets [Clark & Moulton 1971, Iio et. al. 1980, Adachi et. al. 1973]. Neutron diffraction studies have revealed that the transition that occurs at a higher temperature corresponds to a transition from the anti ferromagnetic phase to a phase in which the moments lying in a plane perpendicular to the basal plane form a modified triangular array [Yelon & Cox 1973].

According to recent theoretical studies [Mekata & Adachi 1978, Matsubara 1982, Wada et. al. 1982] the intermediate phases in compounds with successive phase transitions have somewhat dynamical characteristics associated with the partially disordered state or sub lattice switching. Partially disordered state means that the magnetic structure in the c-plane is composed of three sub lattices (three kinds of chains) and the spin moments in one third of the chains are not ordered and the spin moments in the rest of chains are ordered. The sub lattice switching denotes that the disordered chains and the ordered chains switch with one another as a function of time.

Successive phase transitions at $T_{N1} = 4.8\text{K}$ and $T_{N2} = 4.3\text{K}$ have been found in CsNiCl_3 from measurements of specific heat, NMR, thermal expansion and neutron scattering [Adachi & Mekata 1973, Clark & Moulton 1971, Rayne et. al. 1977, Yelon & Cox 1973, Kadowaki et. al. 1987]. The nature of the successive phase transitions in CsNiCl_3 is controversial. Clark & Moulton [1971] studied the NMR of ^{135}Cl and ^{133}Cs and considered that the high temperature transition at T_{N1} corresponds to an anti ferromagnetic ordering of the component of Ni^{2+} spins parallel to the c-axis while the perpendicular component is ordered at T_{N2} . Below T_{N2} the spins form the 120° structure in the ac-plane.

From neutron scattering experiments Yelon & Cox [1973] proposed a model in which the ordered 120° spin structure below T_{N1} reorientates by 90° rotation around the c-axis at T_{N2} , Kadowaki et. al. [1987] has shown that the sub lattice magnetisation M^{s+} is zero between T_{N1} and T_{N2} . The successive phase transitions can be understood by the successive freezing of the free rotations of the 120° spin structure [Maegawa et. al. 1988]. Below T_{N1} the rotation around the a-axis is frozen but the 120° structure has the quasi degeneracy in the ac-plane due to the small anisotropy and also it rotates freely around the c-axis due to the effects of frustration.

RbNiCl_3 an Ising-like Heisenberg antiferromagnet on a triangular lattice (HATL) has been reported to have only one phase transition at 11.11K [Johnson et. al. 1979, Rayne et. al. 1981, Collocott & Rayne 1987, Yelon & Cox 1972]. However a recent neutron scattering study [Oohara et. al. 1991] revealed two successive phase transitions in RbNiCl_3 at $T_{N1}=11.25\text{K}$ and $T_{N2}=11.11\text{ K}$ similar to those in other Ising-like HATL. Many theoretical and experimental studies [Matsubara 1982] have revealed that an Ising-like HATL has two successive phase transitions. Below the upper transition temperature T_{N1} and the lower T_{N1} spin components parallel and perpendicular to the c-axis are in ordered states respectively.

CsFeBr₃

2.4 The AFeX₃ compounds:

CsFeBr₃ is one of a series of isomorphous AFeX₃ compounds (A= Rb, Cs, Tl or NH₃ and X= Cl or Br) that have been used as a model magnets [Achiwa 1969, Yoshizawa et. al. 1980, Steiner et. al. 1981, Schmid et. al. 1992]. The magnetic behaviour of these materials is the result of a delicate balance between several competing interactions.

All the salts listed above crystallise in the hexagonal perovskite structure but have the following differences in magnetic properties:

a. The chlorides behave as pseudo one-dimensional ferromagnets, whereas the bromides that have been characterised so far (A=Rb, Cs, NH₃) [Visser & Harrison 1988, Harrison et. al. 1991] are pseudo one-dimensional antiferromagnets.

b. The caesium salts behave as singlet ground state (SGS) systems but the rubidium, ammonium and thallium salts that have been studied have magnetic ground states with long-range magnetic order at low temperature.

2.4.1 Crystal structure and magnetic properties of CsFeBr₃ and related materials:

The ternary compounds AFeX₃ (with A = Rb, Cs; X = Cl or Br) all have at room temperature the same hexagonal structure with space group P6₃/mmc. Chains of face sharing AX₆ octahedra running along the c-axis are separated by the Rb or Cs ions. Thus the magnetic interaction along the chains is stronger than the one between the chains.

In all cases the Fe²⁺ ion has an effective spin S=1 and locally a singlet ground state (SGS) with m=0 due to the single ion anisotropy. If the exchange interaction is small compared to this anisotropy, the whole system has a SGS at T→0. This is the case for CsFeCl₃ [Steiner et. al. 1981] and CsFeBr₃ [Dorner et. al. 1988], while in RbFeCl₃ [Yoshizawa et. al. 1981] and RbFeBr₃ [Harrison & Visser 1992, Adachi et. al. 1983] the

total exchange energy is large enough to produce magnetic long range order at low temperatures. Some characteristics of these four compounds are summarised by Visser [Visser & Harrison 1988].

Neutron investigations have shown that the Cl-compounds order ferromagnetically and the Br-compounds antiferromagnetically along the chains. The interaction between chains is anti ferromagnetic in all 4 compounds. If there is 3-dimensional magnetic order a frustrated 120° structure occurs in the hexagonal plane. A characteristic feature of these SGS systems is the softening of a magnetic excitation at the magnetic zone centre with decreasing T due to the correlations induced by the exchange interaction. Such a soft mode has been observed in all four compounds. In the Rb systems it condenses out and leads to long range static order. In the Cs compounds the soft mode approaches a finite value for $T \rightarrow 0$ as expected for SGS system.

The application of a magnetic field parallel to the c -axis in the SGS CsFeCl_3 [Steiner et. al. 1981] and CsFeBr_3 [Dorner et. al.1990] leads to a phase transition resulting in an ordered state. These experiments have shown that the phase transition is connected with the softening of a mode with a wave vector which specifies the ordered state. In CsFeCl_3 three consecutive phase transitions with increasing field have been observed at 0.7 K. The first two lead to incommensurate structures at 3.8 and 4.1 Tesla, at 4.5 Tesla a commensurate 120° structure appears [Knop et. al. 1983].

In CsFeBr_3 , the application of an external magnetic field along the c -axis leads immediately to a 120° structure. At a temperature $T=1.6$ K, a commensurate phase has been found at 4.1 Tesla [Dorner et. al. 1990]. The magnetic excitations of CsFeBr_3 have been studied by inelastic neutron scattering in the presence of an applied magnetic field, $H//c$ and $H \perp c$ [Visser et. al. 1991]. For a magnetic field applied parallel to the c -axis, the dispersion curve renormalises so that the exchange interaction has a decreasing influence with increasing field. With $H \perp c$ there is little or no effect on the dispersion of the magnetic excitations. It was also found that the lowest frequency mode softens with decreasing temperature but stabilizes at 0.11 THz below 2.5 K indicating that CsFeBr_3 remains a SGS systems for $T \rightarrow 0$ [Schmid et. al. 1992].

CHAPTER 3

Brillouin Scattering

3.0 Introduction:

Inelastic light scattering spectroscopy has been widely applied since its advent in the 1920's, and the advent of the laser source in the 1960's revitalised this technique making observable many new phenomena. Since the introduction of the multipass Fabry-Perot Interferometer, the technique of Brillouin Scattering has been finding widespread applications. These include the study of thermally induced excitations in a range of materials from insulators to semiconductors and metals [Sandercock 1979]. These studies yield a wealth of information on magnetic systems in terms of magneto-optics effects, exchange interaction, gyro magnetic ratio, anisotropy and spin wave lifetime [Wettling et. al. 1975, Catlow et. al. 1978, Ganot et. al. 1982]. Measurement of sound velocity, elastic constants and photo elastic constants on transparent and non transparent material using Brillouin scattering technique has also been performed [Sandercock 1971, Vacher & Boyer 1972].

The study of materials undergoing structural phase transitions has been developed in the last few years into one of the more active fields in solid state physics. The distortion occurring at a phase transition is characterised by an order parameter which couples to a greater or lesser extent to static strains in the system. For the case of linear coupling between strain and order parameter, an elastic constant is driven to zero at the phase transition. For weaker coupling, a correspondingly weaker elastic anomaly will appear [Sandercock 1975].

Clearly the determination of the anomalous elastic constant by Brillouin Scattering can be helpful in increasing the understanding of the

mechanism underlying the phase transition. Brillouin Scattering measurements at phase transition are limited to relatively transparent materials, since otherwise the small penetration depth of the laser light causes the phonon peaks to become very broad.

Many crystal shows pronounced acoustic anomalies in the region of structural phase transitions and in some cases the anomalies are due to interaction between soft optic modes and acoustic modes. The acoustic anomalies can be observed by measuring sound velocities (and hence elastic constant) by using Brillouin scattering techniques. The samples studied here were TMMC, TMMB, TMMC:Cu, RbNiCl₃ and CsNiCl₃ in the temperature range of 80-450K.

3.1 Energy and momentum conservation:

Consider an experimental situation as represented schematically in Figure 3.1. A monochromatic light of angular frequency ω_i is incident on the scattering medium with wave vector \vec{k}_i . The magnitude of \vec{k}_i is given by

$$\bar{k}_i = \frac{2\pi\eta_i}{\lambda_i} \quad \text{.....3.1}$$

where λ_i is the wavelength of the incident light and η_i is the corresponding refractive index of the medium.

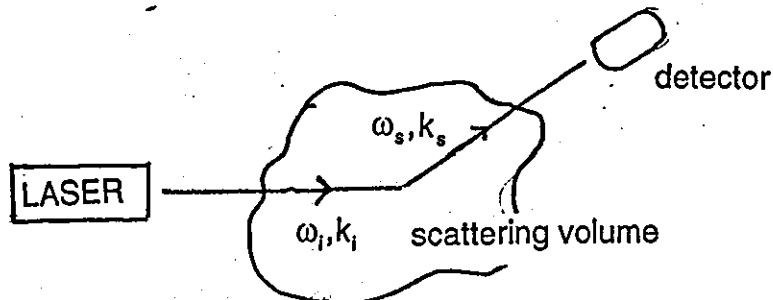


Fig. 3.1: Illustration of the light scattering geometry

The scattering process will be inelastic, because an incident photon of energy may take energy from, or give energy to an excitation in the medium in order to produce the scattered photon of energy $\hbar\omega_s$. The scattered light of wave vector $\bar{k}_s\lambda_s$, and frequency ω_s will arrive at the detector. By analogy with eq.3.1 ,

$$\bar{k}_s = \frac{2\pi\eta_s}{\lambda_s} \quad \text{.....3.2}$$

where λ_s is the wavelength of the scattered light and η_s the corresponding refractive index. The scattered intensity is usually distributed across a range of frequencies as shown in Figure 3.2.

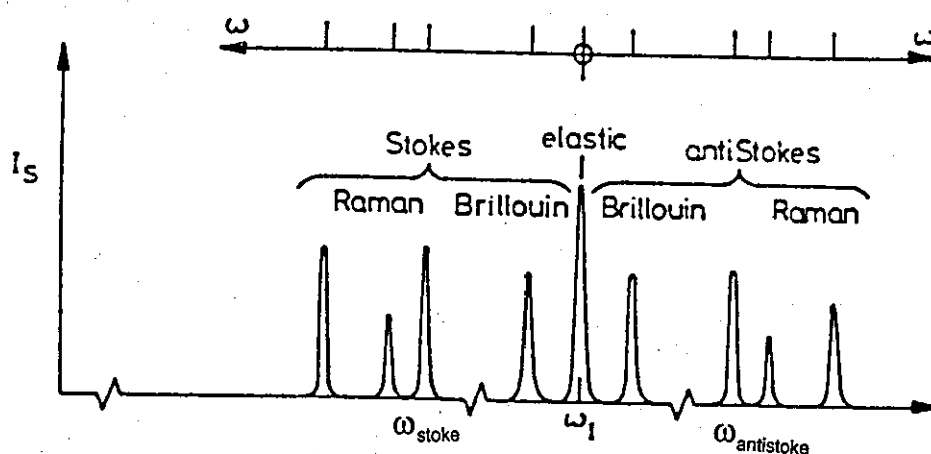


Fig. 3.2: Schematic spectrum of scattered light

The peak in the centre of the spectrum is the contribution of the incident photons that have been elastically scattered with no change in frequency. The remaining peaks correspond to inelastic scattering and their shifts ω_i normally occur in two different frequency ranges.

The Brillouin component, resulting from scattering by sound waves occurs close to the frequency of the incident light; typical shifts are approximately

1 cm⁻¹ or smaller. The Raman component resulting from scattering by internal vibrations of molecules or optic vibrations in crystals, lies at higher shifts, normally larger than 10 cm⁻¹ and often in the order of 100 - 1000 cm⁻¹. The inelastic contributions are further subdivided, those scattered with frequencies smaller than ω_i are denoted as ω_{stokes} , known as Stokes component, whilst those scattered with frequencies larger than ω_i are denoted as $\omega_{\text{antistokes}}$ known as anti-Stokes components. Each scattered photon in the Stokes component is associated with a gain in energy $\hbar\omega$ by the sample, where

$$\omega = \omega_i - \omega_{\text{stokes}} \quad \text{.....3.3}$$

Similarly, the sample loses energy $\hbar\omega$ for each scattered photon in the anti-Stokes components where

$$\omega = \omega_{\text{antistokes}} - \omega_i \quad \text{.....3.4}$$

Equation 3.3 and 3.4 express conservation of energy in the inelastic light scattering process where this process conserves momentum [Kittel 1976]. Figure 3.3 shows vector diagrams for the conservation of momentum in the two kinds of inelastic scattering. The wave vectors for the Stokes scattering shown in Figure 3.3i has the property

$$q^2 = k_i^2 + k_s^2 - 2k_i k_s \cos\psi \quad \text{.....3.5}$$

$$\text{with } \bar{k}_i = \frac{2\pi\eta_i}{\lambda_i} \quad \text{and} \quad \bar{k}_s = \frac{2\pi\eta_s}{\lambda_s}$$

The refractive indices η_i and η_s are defined for the directions of the incident and scattered light propagating with mutual angle ψ .

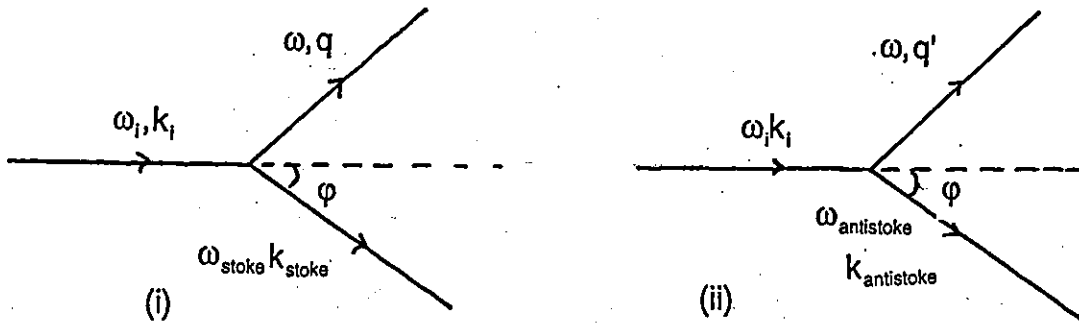


Fig. 3.3 Vector diagram for the conservation of momentum in (i) Stokes scattering (ii) anti-Stokes scattering

The Brillouin shifts ν , of the frequency of light resulting from inelastic scattering of light from acoustic phonons can be given in the form [Chandrasekharan 1951]

$$\nu = \frac{v}{\lambda} [\eta_i^2 + \eta_s^2 - 2\eta_i\eta_s \cos\psi]^{1/2} \quad \dots 3.6$$

where v is the velocity of the acoustic phonons and λ is the wavelength of the laser light used.

3.2 Theory of the Fabry-Perot Interferometer:

In the field of Brillouin scattering, the most satisfactory instrument available for the detection of the frequency shifted components is the Fabry Perot Interferometer. This instrument has a resolving power as high

as 10^8 and is thus well suited for resolving the Brillouin components from the central component where the frequency shifts are normally in the range 180 MHz to 100 GHz [Sandercock 1971].

A Fabry-Perot interferometer in principle consists of two plane mirrors mounted accurately parallel to one another with optical spacing d between them as shown in Figure 3.4.

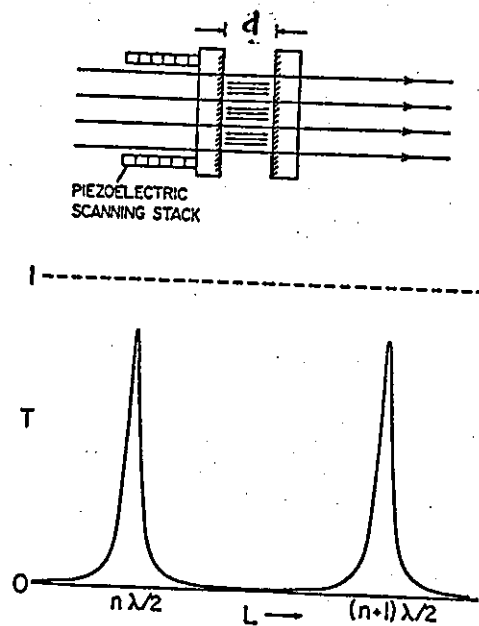


Fig. 3.4: Experimental arrangement and transmission function of a Fabry-Perot interferometer

The mirrors are optically coated so that the inner surface reflectivities are ≈ 0.95 . When incident parallel light falls onto these mirrors at an angle θ , the transmitted wavelength λ is given by the interference conditions [Jenkins & White 1957] as follows:

$$m\lambda = 2nd \cos \theta \quad \dots\dots\dots 3.7$$

where $m = 0, 1, 2, \dots$ in the order of the interference

η = refractive index of the medium between the mirrors (usually air $\eta = 1$)

d = separation between the reflecting surface

When $\theta=0$, the condition for a maximum transmission at wavelength λ of order m to coincide with a maximum at wavelength $\lambda + \Delta\lambda$ of order $m + 1$ is

$$\Delta\lambda = \frac{-\lambda^2}{2\eta d} \quad \dots\dots\dots 3.8$$

This separation $\Delta\lambda$ is known as the free spectral range (FSR) and in terms of $\sigma = 1/\lambda$, it is

$$\Delta\sigma = \frac{1}{2\eta d} \text{ cm}^{-1} \quad \dots\dots 3.9$$

It is evident that the FSR depends on the refractive index η and the mirror spacing d , and thus there are two ways to scan the interferometer. The first way is to vary η by changing the pressure of the gas between the mirror [Durvasula & Gammon 1978] and the second is to alter d mechanically by means of a piezoelectric drive on one of the mirrors [May et. al. 1978].

The full width at half maximum of the transmission light ($\delta\sigma$) determines the resolution of the interferometer and the finesse F is defined as

$$F = \frac{\Delta\sigma}{\delta\sigma} \quad \dots\dots 3.10$$

The finesse F is governed by several factors such as the reflectivity finesse, flatness finesse, pinhole finesse and instrumental finesse [Cottam & Lockwood 1986]. The reflectivity finesse for plane mirrors of reflectivity R is given by

$$F_R = \frac{\pi R}{(1-R)} \quad \text{.....3.11}$$

and the flatness finesse is

$$F_F = \frac{M}{2} \quad \text{.....3.12}$$

where $1/M$ is the deviation (expressed as a multiple of the wavelength) from true flatness or parallelism across the mirrors. The instrument finesse is obtained from

$$\frac{1}{F^2} = \frac{1}{F_R^2} + \frac{1}{F_F^2} \quad \text{.....3.13}$$

For the interferometer used for Brillouin scattering spectroscopy, the size of the pinhole P2 (Figure 3.9) determines the degree of collimation of the light that reaches the detector (photo multiplier). The associated pinhole finesse is

$$F_P = \frac{4\lambda f^2}{D^2 d} \quad \text{.....3.14}$$

where f is the focal length of lens L (Figure 3.9) and D is the pinhole diameter. Therefore the total finesse is given by

$$\frac{1}{F^2} = \frac{1}{F_f^2} + \frac{1}{F_p^2} \quad \text{.....3.15}$$

The contrast of the interferometer is an important factor for magnon studies where the stray light intensity can be high. The contrast C [Cottam & Lockwood 1986] is given as

$$C = 1 + \frac{4F_R^2}{\pi^2} \quad \text{.....3.16}$$

The single pass Fabry-Perot interferometer has proved useful for studying strong Brillouin features such as acoustic phonons in transparent solids. In surface magnon work on opaque solids, stray laser light can be very intense. In this case, the contrast of the interferometer may be too low to allow the Brillouin scattering to be seen.

3.3 The development of the Brillouin scattering spectrometer:

Brillouin scattering using a Fabry-Perot interferometer has been a well-established method for investigation of thermally excited sound waves in liquids and solids. However, it was recognised early in the field of Brillouin scattering that the standard Fabry-Perot interferometer has too low a contrast to allow the weak Brillouin signal to be observed in the presence of the normally extremely intense elastically scattered light.

Although index matching techniques and resonant absorption of the elastically scattered light somewhat alleviated this problem, it was the high contrast of the multipass interferometer [Sandercock 1971] which reduced

Brillouin scattering to a relatively simple and widely applicable technique. For an experiment involving a measurement on a large transparent crystal, the Fabry-Perot is a satisfactory instrument [Sandercock 1975]. When the crystal is opaque or small and imperfect, it was found that the light scattered elastically from defects, particularly at the surfaces, maybe more intense than the Brillouin peaks by four to nine or more orders of magnitude. To overcome this problem, Sandercock has designed an efficient multipass Fabry Perot interferometer, in which the beam of light passes several times (up to five) through the same interferometer to increase the contrast of the interferometer. It can be seen that the contrast [Sandercock 1971] is:

$$C_n = C_1^n \quad \dots 3.17$$

where n is the number of passes of the beam through the Fabry-Perot interferometer, C_1 is the contrast due to one pass.

The success of Sandercock's design was determined to a great extent, by the fact that he used a corner cube to reflect the beam of light under its multiple propagation. A corner cube represents a triangular pyramid, which is obtained if a portion of a cube is cut-off by a plane normal to the spatial diagonal. The section plane forms the base of this pyramid. A beam of light comes out of the pyramid strictly parallel to the incident beam irrespective of the inclination of the pyramid axis relative to the incident beam of light. Incident and reflected beams can be separated in space and this makes it possible to construct a multipass interferometer shown schematically in Figure 3.5.

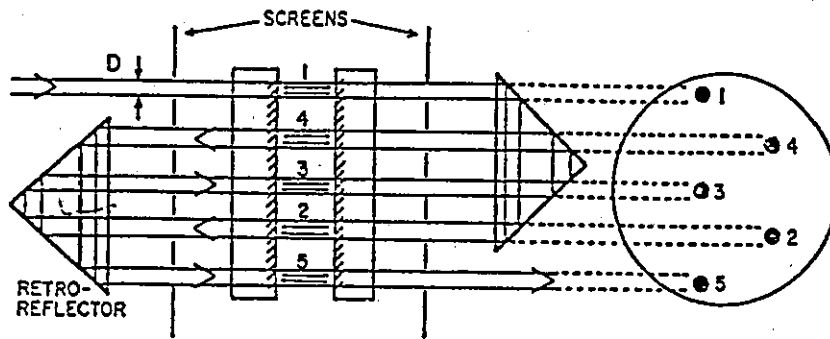


Fig. 3.5: Experimental arrangement for a five pass interferometer showing screens used to reduce scattered light.

The use of multipass interferometers permitted the increase in the contrast and in the case of a five pass FPI [Sandercock 1971] up to 10^{12} . The other parameters vary not so significantly. Comparison of the one pass and multipass interferometers for the finesse F , contrast C and transmittance T are as follows: [Borovnik & Kreines 1982]

One pass

$$\frac{1}{F_1^2} = \frac{1}{F_R^2} + \frac{1}{F_s^2}$$

$$C_1 = 1 + (4/\pi^2)F_1^2$$

$$T_1 = 1 - \left(\frac{u}{1-R} \right)^2$$

Multipass

$$F_n = \frac{F_1}{\sqrt{2^{1/n} - 1}}$$

$$C_n = C_1^n$$

$$T_n = T_1^n$$

Table 3.1 shows the comparison of the numerical values of the parameters for one, three and five pass interferometers with the absorption coefficient of the mirror $u=0.2\%$ and $u=0.5\%$.

Table 3.1 Characteristics of one, three and five-pass FPI

R	0.98	0.94			0.87		
Number of passes	1	1	3	5	1	3	5
F_s	84	45	88	116	22	43	57
C_s	2.9×10^3	0.82×10^3	5.5×10^8	3.7×10^{14}	1.96×10^3	7.5×10^6	2.9×10^{11}
$T_s^{(1)}$	81%	93%	82%	71%	97%	91%	86%
$T_s^{(2)}$	56%	84%	59%	42%	92%	79%	68%

(1) $u = 0.2\%$

(2) $u = 0.5\%$

In 1980, a practical tandem combination of multipassed interferometer was introduced by Sandercock based on a common translation stage [Sandercock 1980]. This instrument offers the highest resolution, contrast and free spectral range, combined with ease of use of any available spectrometer for Brillouin scattering.

The principle of the interferometer construction is shown in Figure 3.6. A scanning stage consisting of a deformable parallelogram rides on top of a roller translation stage. The former, actuated by a piezoelectric transducer, provides completely tilt-free movement of the interferometer mirror over scan lengths of up to $10 \mu\text{m}$ or more. The latter enables the coarse mirror spacing to be set to the desired value in the range 0-50 mm. The roller translation stage is sufficiently collinear that a movement of several mm leaves the mirrors aligned parallel to better than 1 fringe across the total mirror diameter.

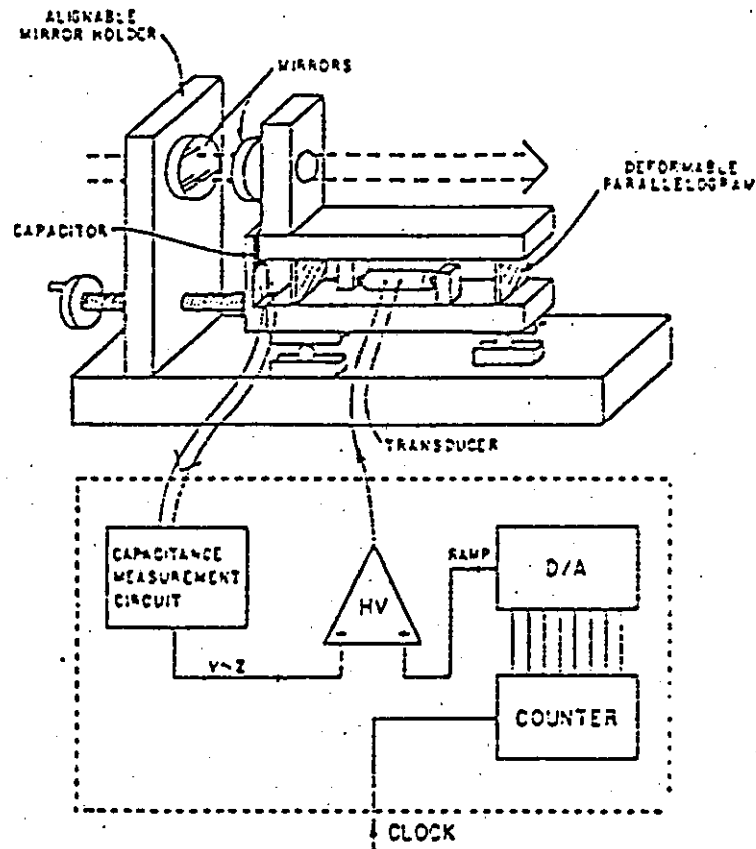


Fig. 3.6 Principle of interferometer construction

The novelty of the construction is the use of a small parallel plate capacitor to measure the scan displacement. The associated electronics produces a voltage accurately proportional to the capacitor spacing. This voltage being used in a feedback loop in order to linearise the scan displacement with respect to the applied scan voltage.

By a slight modification to the scanning stage of the instrument depicted in Figure 3.6, it is possible to make a synchronously scanning tandem interferometer [Sandercock 1980, Lindsay et. al. 1981, Mock et. al. 1987]. The new scanning stage viewed from above is shown in Figure 3.7.

The first interferometer FP1 is arranged to lie in the direction of the translation stage movement. One mirror sits on the translation stage, the other on a separate angular orientation device. The second interferometer

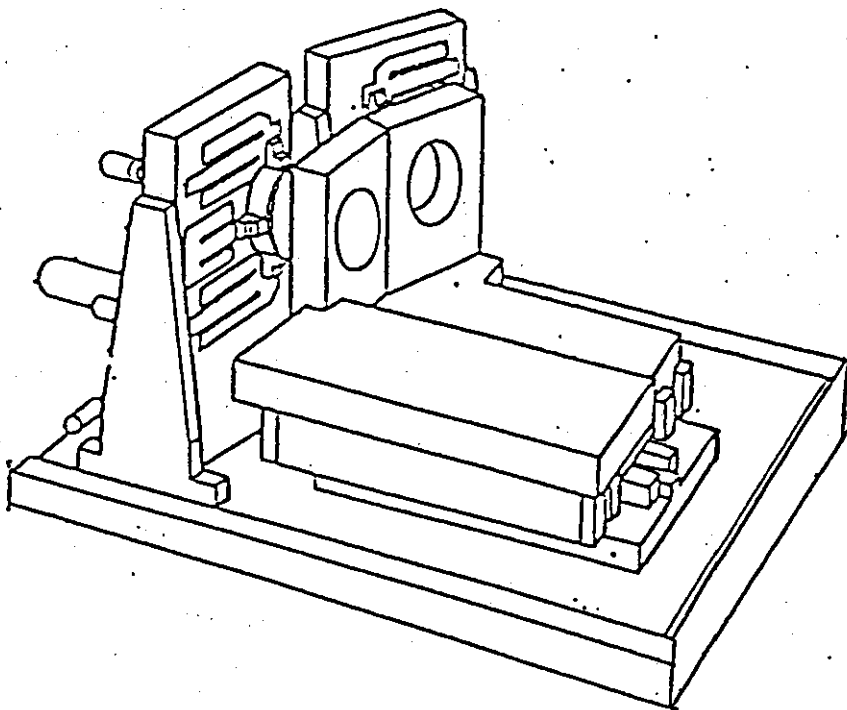
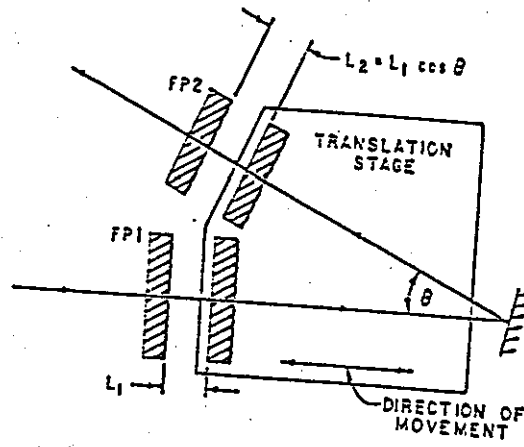


Fig. 3.7: Tandem scanning stage

FP2 lies with its axis at an angle θ to the scan direction. One mirror is mounted on the translation stage in close proximity to the mirror of FP1, the second mirror on an angular orientation device that can also allow a small translation of the mirror for adjustment purposes. The relative spacing of the mirrors are set so that a movement of the translation stage to the left brings both sets of mirrors into simultaneous contact.

The transmission curves for the individual interferometers FP1 and FP2 as a function of wavelength are shown in Figure 3.8 where the transmitted wavelength satisfies the conditions

$$\lambda_1 = \frac{2d_1}{p_1} \quad \text{and} \quad \lambda_2 = \frac{2d_2}{p_2} \quad \dots\dots 3.18$$

where p is an integer, d is the mirror spacing and the indices refer to the two interferometers.

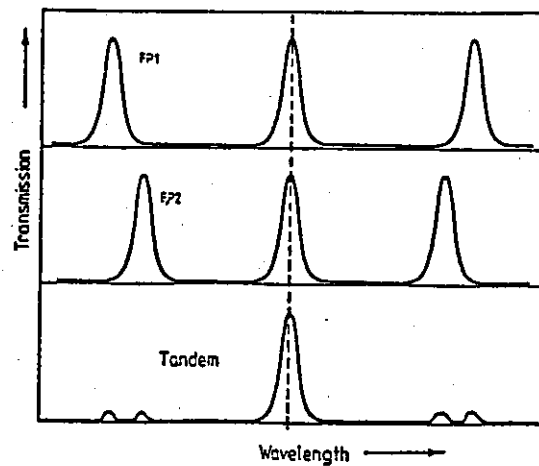


Fig. 3.8 Illustration of the principle of vernier tandem operation of two Fabry-Perot interferometers

A given wavelength λ will be transmitted by both interferometers if the ratio d_1 / d_2 is chosen so that

$$\frac{d_1}{d_2} = \frac{p_1}{p_2} \quad \text{.....3.19}$$

In order to scan the transmitted wavelength both d_1 and d_2 must be changed in such a manner that their ratio remains constant and equal to p_1 / p_2 . This is automatically achieved by the scanning stage shown in Figure 3.7 which supports the scanning mirrors of both interferometers.

The scanning stage is a combination of a roller translation stage, to allow easy setting of the desired mirror spacing, together with a deformable parallelogram stage to allow a very precise scanning movement. The axis of FP1 is parallel to the scanning direction while the axis of FP2 is rotated by about 18° . It is clear that if the ratio d_1 / d_2 is correctly adjusted at small mirror spacing, it will remain constant at all mirror spacing and so the scan synchronisation is assured ($d_1 / d_2 = \cos 18^\circ = 0.95$).

3.4 Brillouin scattering apparatus:

The main element for Brillouin scattering measurements consist of the laser source, the spectrometer (Fabry-Perot Interferometer), detector, signal processing devices and computer control system.

3.4.1 The triple pass interferometer:

The spectrometer used for this Brillouin scattering study is a triple pass tandem interferometer that was purchased from J.R. Sandercock, RCA Laboratories, Switzerland. The optical system allows the interferometer to

be used in the high contrast triple pass tandem mode. The system has been designed using a minimum number of components and is shown schematically in Figure 3.9.

The scattered light enters the system at an adjustable pinhole P1 (pinhole diameter can be adjustable for 100, 200 and 400 μm). The aperture A1 then defines the cone of light that is accepted and mirror M1 reflects the light towards lens L1 where it is collimated and directed via mirror M2 to FP1. From here, the light will pass through aperture 1 of the mask A2 and is directed via mirror M3 to FP2. After transmission through FP2 the light falls onto the cornercube CC1 where it is reflected downwards and returned parallel to itself towards FP2 where it continues through the aperture 2 of A2 to FP1. After transmission through FP1 it passes through lens L1, underneath mirror M1 and is focused onto mirror M4. This mirror will return the light through lens L1 where it is again collimated and directed through FP1.

After the final pass through the interferometer, through the aperture 3 of A2 the light will strike mirror M5 where it is directed to the prism PR1. This prism in combination with lens L2 and the output pinhole P2, forms a bandpass filter with a width determined by the size of the pinhole. Mirror M2 sends the light to the output pinhole P2.

The combination of lens L1 and mirror M4 lying at its focus is known as a catseye, and is optically equivalent to a cornercube but has the advantage that it also acts as a spatial filter that filters out unwanted beams such as the beams reflected from the rear surface of the interferometer mirrors.

3.4.2 The light source:

A laser provides an intense, monochromatic, highly collimated, highly polarised beam of light that is ideal for light scattering studies. Lasers come in a multitude of forms, and for this Brillouin scattering work an

Fig. 3.9. Optical element for tandem operation in the transmission mode

Argon-ion laser was used (Spectra-Physics Model 165) which produces an intense output in the blue (488.0 nm) and green (514.5 nm) wavelength with maximum power output of 0.8W. This laser is capable of operating in the single TEM_{00} mode, the single frequency output power is obtained with an addition of an etalon. The beam diameter is 1.25 mm and its beam divergence is 0.69 mrad.

3.4.3 Detectors:

The main light detector is a Philips XP2252 photo multiplier tube. This is a twelve stage tube with a maximum gain of 10^{+8} ; it has a bialkali photo cathode giving it a quantum efficiency of about 15% at 514nm. It is used as a photon counter in conjunction with an EMI 604-A amplifier discriminator.

To make sure the tube performance is not affected by the surroundings such as the magnetic and electric field, it is shielded. The tube is wrapped in an aluminium foil and connected to an earth potential to shield it from electric fields. The assembly is housed in an iron tube to exclude the magnetic field.

3.4.4 Vibration Isolation:

The interferometer requires a vibration free environment. In order to scan a Fabry-Perot through a single transmission peak, a change in mirror spacing of about 25 Å is required, so any external influence that distorts the mirror spacing by more than a few Å will seriously degrade the spectrum.

An enclosure is built around the interferometer to protect it from thermal fluctuations and sound as well as stray light from the surroundings. The whole assembly for this experiment was mounted on a compressed air

cushioned table (Anaspec Zero-G) in order to decouple the spectrometer from vibrations. The design employed by this system is a twin chamber pneumatically damped air cushion operating as integral part of the four support legs. Air supply to the isolator pressure chambers is controlled by way of these independent control valves activated by a unique valve system.

3.4.5 The cryogenics system:

For low temperature measurements, a cryostat (Oxford Instrument model CF1104) was used. This continuous flow cryostat operates on the principle of a continuous and controlled transfer of coolant from a separate storage vessel to the continuous flow cryostat. The coolant flows through the heat exchanger of the continuous flow cryostat where the temperature is measured and a heater is used to control the temperature. The sample temperature is continuously variable from 3.8K up to 500K when using liquid helium or from about 77K up to 500K when using liquid nitrogen.

Figure 3.10 shows the main parts of the cryostat. The sample is mounted in vacuum on a copper finger and cooled or heated by conduction. To change the sample, the cryostat must be at room temperature before the vacuum case and radiation shield are removed. A RhFe resistance sensor is used for temperature sensing on the heat exchanger.

The temperature is controlled by a temperature controller (Oxford Instrument ITC4). The sample temperature is monitored by a sensor namely RhFe thermocouple. The ITC4 is operated manually that is by means of front panel push buttons and associated status lamps. The sample temperature is varied by balancing the cooling power of the liquid coolant with a heater in a flow cryostat. Figure 3.11 shows a schematic flow diagram for this cryogenics system.

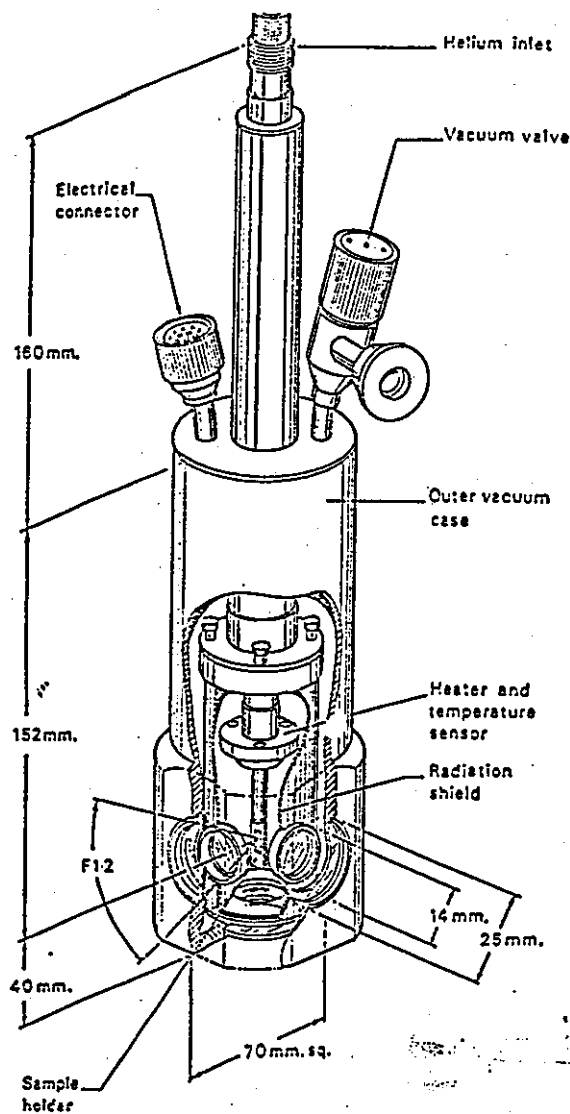


Fig. 3.10: The CF1104 cryostat

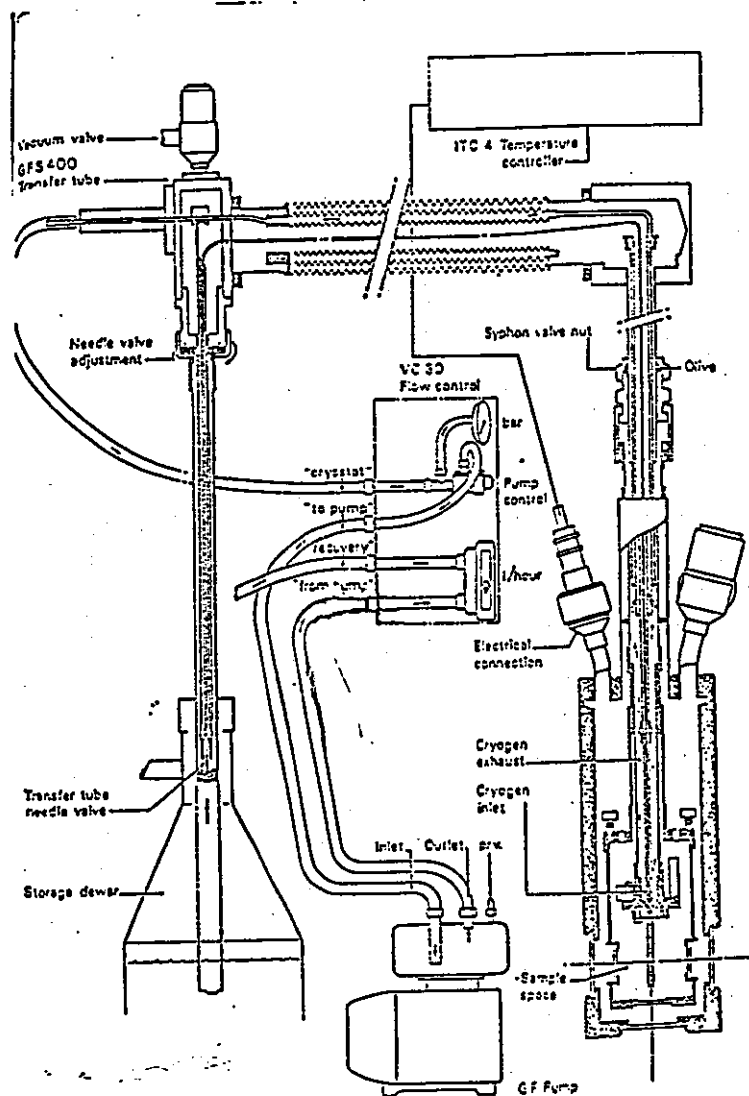


Fig. 3.11 The schematic flow diagram

3.5 Alignment for the back-scattering configuration:

A diagram for the back-scattering configuration is as shown in Figure 3.12. The procedures for the alignment are as follows:

1. A suitable height for the laser light is chosen, 15 cm above the table. To avoid unexpected beam paths or reflections, the laser power used should be as small as possible (< 1 mW)
2. Mirrors M1, M2 and M3 are arranged to get the laser light to hit prism P.
3. Light from prism P will be reflected onto mirror M4 and M5 and onto sample S in the cryostat. At this stage the laser light from M5 to sample S must be horizontal and on the axis of the sample.
4. M4 and M5 can be adjusted to get the light onto the surface of the sample, and to ensure that the scattered light falls onto the centre of mirrors M4 and M5 to avoid the scattered light being cut-off.
5. Once this is done, lens L1 is introduced. The scattered light from the sample can now be focused into the pinhole P1 by adjusting mirror M6 and M7.
6. A properly focused scattered light can be seen on mirror M1 (see Figure 3.9), which should suddenly and evenly become fainter when one of the mirrors M6 or M7 (or lens L2) is moved.

3.6 Alignment of the optical system:

The interferometer is normally used in a multipass tandem mode. The system can only be made to operate in this mode if both interferometers have been pre-aligned parallel and with correct relative spacing. The following description provides the procedure for achieving correct alignment of the optical system. Refer to Figure 3.9 and 3.13.

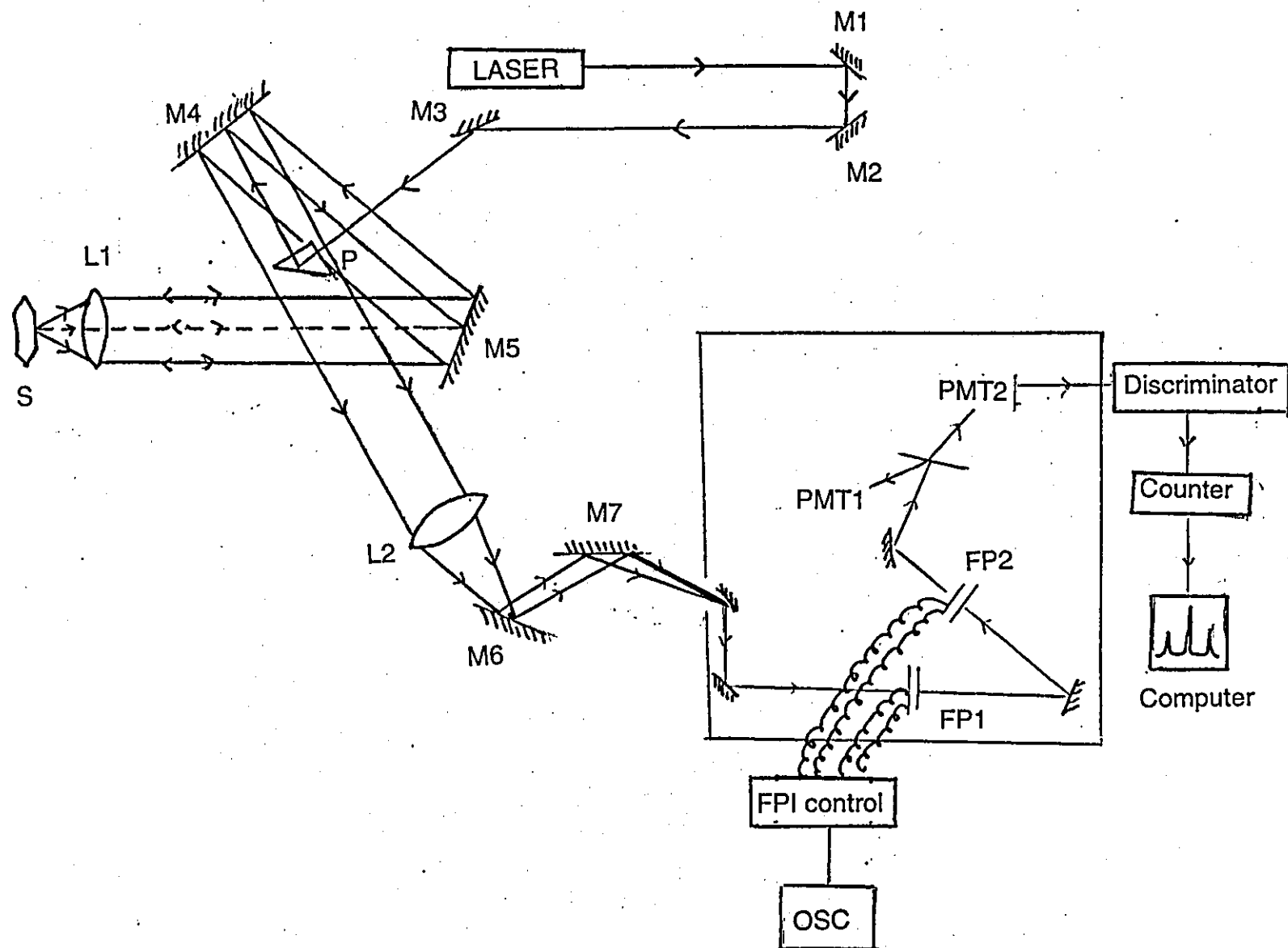


Fig. 3.12 Experimental layout for Brillouin scattering experiment (backscattering configuration)

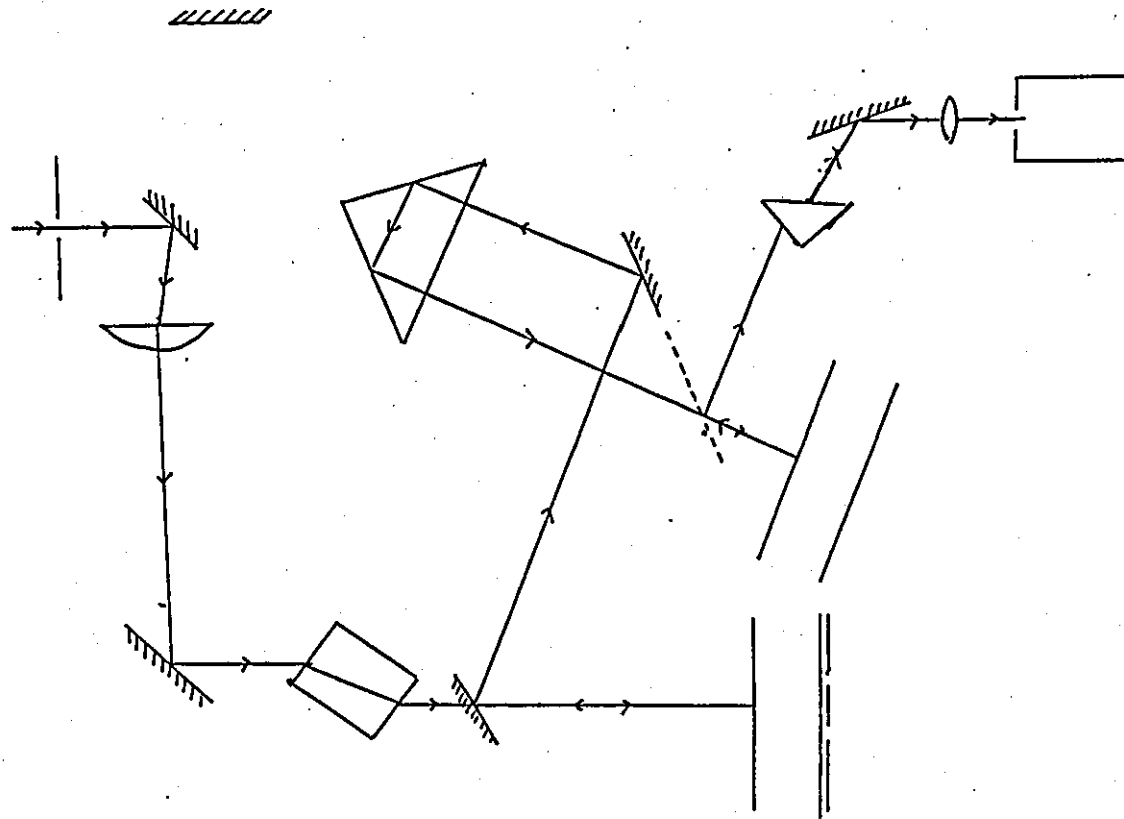
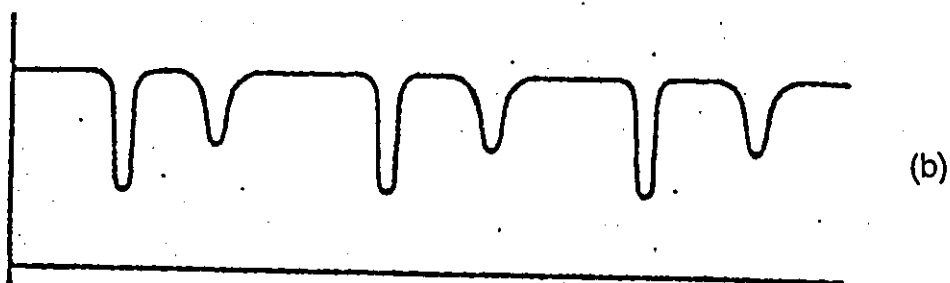
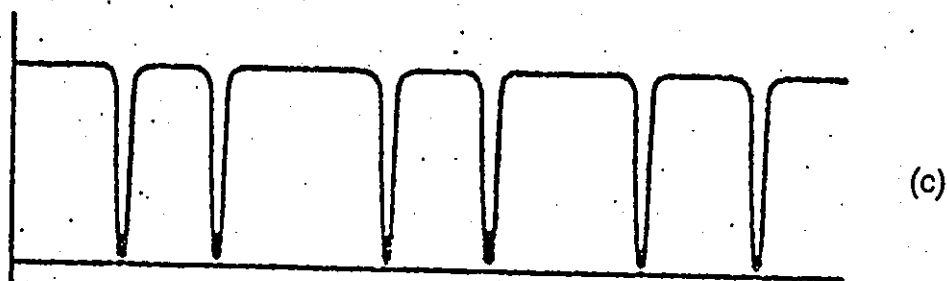


Fig. 3.13a Basic optical system used for achieving alignment in reflection mode



b) The measured reflected intensity for two imperfectly aligned interferometers



c) The intensity after correct adjustment but before synchronisation

For our alignment, we use light scattered from a sandblasted aluminium block, focused by a 6 cm focal length lens onto the input pinhole P1 (400 μm) and adjusted to fill the aperture A1. The first aim is to make sure that the beam falling on FP1 is collimated, perpendicular to the mirror surface, and at the right location.

1. Adjust M1 so that the right hand edge of the mirror is about 41 mm from the aperture A1 and at the same time slide the base of M1 so that the input beam strikes M1 about 1 mm from its right hand edge. Orient M1 so that the beam now passes through lens L1 - the vertical diameter of L1 should touch the right hand edge of the beam.

2. Use a mirror to reflect the beam after L1 onto a distant wall. Adjust the focus of L1 for parallel light. Temporarily place the corner cube CC just after L1. Adjust the orientation of M1 so as to centre the reflected beam on the catseye. Remove the corner cube.

3. Slide the base of M2 so that the beam passes through the appropriate aperture of A2 and so that at the same time the reflected beam from FP1 approximately folds back to itself. It will be necessary to keep FP1 aligned - the z control is used to obtain transmission .

The front end optics have been crudely aligned. Precise adjustment are as follows:

4. Adjust M1 so that the beam cleanly fills the aperture A2.

5. Look for the beam reflected from FP1. It should strike the rear surface of A1 as a bright spot, use M2 to send the bright spot back through A1. Repeat 4 and 5 if necessary.

6. The reflected beam should now pass back out through the pinhole and be observable on a piece of card. Optimise the focus of L1 and adjust M2 as required. Repeat steps 4 to 6 if necessary.

The multiple passes through the interferometers are adjusted as follows:

7. With FP1 aligned and adjusted for steady transmission (zero scan amplitude) use M2 to direct the beam 1 onto FP2 so that the reflected beam returns through the aperture 1 of A2. Look for fringes on the surface of M3, adjust M2 to give five fringes.

8. Align FP2 and using the ΔZ control, adjust for steady transmission. Beam 3 should now be visible. Check that it falls cleanly on the aperture 2 of A2. If necessary, translate the corner cube CC1. The corner cube should be rotated slightly so that the front surface reflections do not return to FP2.

9. Adjust the interferometer alignment controls to achieve good transmission of beam 4. This should strike M4. Rotate M4 so that the beam 5 becomes visible after aperture 3 of A2. Translate M4 so that the bright spot seen on its surface is as small as possible. Check beam 5 again and if necessary re-orient M4.

10. Realign the interferometers so that beam 6 is clearly visible. Rotate mirror M5 so that the beam strikes the middle of the side of the prism PR1. Slide M5 so that the beam 6 strikes the mirror near its right hand edge. Rotate PR1 to the minimum deviation position - the transmitted beam will then be circular in cross-section.

11. With aperture A3 centred, orient mirror M6 so that the beam passes through the output pinhole P2. The height of aperture A3 can be adjusted if necessary. If the beam is displaced to the left or right of A3, correct by rotating M5 and realigning M6. Check focus of L2 and adjust if necessary. The tandem multipass optical system is now correctly aligned.

3.7 Stabilising the Fabry-Perot:

In order to obtain long time stability of an interferometer, it is necessary to apply some form of dynamic control in order to maintain both parallel alignment of the mirrors and correct spacing. After aligning the Fabry-Perot interferometer (as in section 3.6), with the scattered light focused into the pinhole P2; switch on reflection mode (as shown in Figure 3.13a). The transmitted signal is detected by a photo multiplier (using the low sensitivity photo multiplier) and after suitable amplification is displayed on an oscilloscope.

Two dips will be present in voltage (on the oscilloscope). A poorly aligned interferometer is illustrated in Figure 3.13b. The two dips are maximised by varying the tilt of the mirrors of FP1 and FP2. This is achieved by changing the voltage on the piezoelectric crystals which controls X1, Y1, X2 and Y2 (for each interferometer there is one mirror which can be rotated by two axes, that is the x-axis and y-axis). This is done by varying X1, Y1, X2 and Y2 on the interferometer control box.

When the dips are maximised (Figure 3.13c), they have to be brought to the same wavelength by changing ΔZ on the interferometer box. ΔZ adjusts the bias voltage of X2 and Y2, therefore causes a translation in the z direction, which adjust the mirror spacing). Once this is achieved, switch on to transmission mode (Figure 3.9) and the spectrum signal should achieve a maximum amplitude of 5V (as seen on the oscilloscope), and the switches for automatic synchronisation can be activated in order to maintain the peak exactly at the midpoint of the scan.

3.8 Brillouin scattering as a tool for the measurement of elastic and photo elastic constant:

The measurement of the frequency shifts of the Brillouin line permits the determination of the propagation velocity of elastic waves; this method has

recently been improved, so that technical applications such as the determination of the elastic constants of crystal can be easily performed. This method has the advantage of avoiding the creation of important disturbances in the medium, thermal fluctuations provide the necessary elastic waves of small amplitude, and the crystal is studied in conditions near the mechanical equilibrium [Vacher & Boyer 1972].

Photo elastic constants may be calculated from the measurement of the Brillouin line intensities. However, the necessity of using a transparent material restricts the application of the technique (although measurement of elastic constant of a non transparent crystal by means of the Brillouin effect has been performed by Sandercock [1971]).

The components of the displacement U of an elemental volume of density ρ satisfy the following equation

$$\rho \ddot{U}_i = C_{ijkl} \frac{\partial^2 U_l}{\partial x_j \partial x_k} \quad \text{.....3.17}$$

with C_{ijkl} being the components of the tensor of the elastic constants. With solutions in the form of plane sinusoidal waves, equation 3.17 becomes

$$\rho v^2 U_i = C_{ijkl} \bar{q}_j \bar{q}_k U_l \quad \text{....3.18}$$

where v is the phase velocity , ρ is the density and $C_{ijkl} = C_{mn}$ with ($i, j, k, l = 1, 2, 3; m, n = 1, \dots, 6$)

where the arrays of C_{ij} can be written out in squares, thus, [Nye 1957]

$$\begin{bmatrix} C_{11} & C_{12} & C_{13} & C_{14} & C_{15} & C_{16} \\ C_{21} & C_{22} & C_{23} & C_{24} & C_{25} & C_{26} \\ C_{31} & C_{32} & C_{33} & C_{34} & C_{35} & C_{36} \\ C_{41} & C_{42} & C_{43} & C_{44} & C_{45} & C_{46} \\ C_{51} & C_{52} & C_{53} & C_{54} & C_{55} & C_{56} \\ C_{61} & C_{62} & C_{63} & C_{64} & C_{65} & C_{66} \end{bmatrix}$$

So, the elastic constants that govern the [100] direction will be C_{11} , C_{66} or C_{55} where C_{11} is longitudinal acoustic mode (LA) and C_{66} or C_{55} is the transverse acoustic mode (TA). For the [001] directions, the elastic constant is governed by C_{33} and C_{44} where C_{33} is the longitudinal acoustic (LA) mode and C_{44} is the transverse acoustic (TA) mode.

3.9 Experimental procedure:

The experimental arrangement of the equipment used for these Brillouin scattering studies is as shown in Figure 3.12. The Brillouin spectrum is excited using $\lambda = 514.5$ nm of single mode argon-ion laser equipped with intra-cavity etalon to reduce the line width of the laser. The back scattering configuration was used with the laser light incident along [1 0 0] direction (perpendicular to the crystal c-axis) and [001] direction (parallel to the c-axis).

The spectrum of the scattered light was analysed by using a triple pass interferometer and the detection of the light was made by a photo multiplier followed by photon counting electronics and multichannel analyser in which the spectrum of the scattered light was registered. At each measuring temperature, an average value of the frequency, intensity and half-width of the Stokes and anti- Stokes peaks were calculated by fitting a Lorentzian line shape to them.

The crystal samples supplied to be used in this experiment (TMMC, TMMC:Cu,TMMB. RbNiCl_3 and CsNiCl_3) were grown from solutions by

slow evaporation at room temperature. The crystals used were not cut nor polished due to lack of these facilities, initial samples with good surface were chosen from the crystals as received. The sample was mounted in the cryostat, and the temperature could be varied from 80 K to 500 K. Whilst collecting the spectrum the temperature of the cryostat could be controlled within ~ 1 K with a laser power 50 mW.

The heating due to the laser beam can be taken into account. Comparing the results for different illuminating power allows us to estimate the real temperature of the sample. From Figure 3.14, (for TMMC) the temperature of the sample should be corrected by +4.6K for laser power of 50mW. We apply the same correction for TMMB, TMMC:CU, RbNiCl_3 and CsNiCl_3 .

3.10 The spectrum:

When the transmission mode is ready to be used, the photo multiplier, discriminator and counter system will measure the intensity of the signal by counting single photons. A typical spectrum is shown in Figure 3.16

The intensity is expressed in counts per second (Hz) indicated by the vertical axis. The frequency of the measured intensity is the horizontal axis that is expressed in channel numbers. In the middle of the spectrum (channel 0) is always a peak (this is the elastically scattered light with no change in frequency) and there are Stokes and anti-Stokes components on the left and right of the spectrum. Phonons and magnons peaks can be observed in between this Stoke and anti-Stokes components.

From the printout of the spectrum we get information such as:

- date and time of the measurement [start time is 11:44:21 and the date is 4/1/95]
- the total measured time and time per channel [32 sec; 0.064 s/channel]
- the wavelength of laser light used [514.5 nm]
- power of laser light used [50 mw]
- pinhole used [400 μ m]
- temperature of the sample measured[273K]
- mirror spacing d of FPI [2.0 mm]
- free spectral range [75.0 GHz]
- the average signal $\langle f \rangle$ [2.06E+04 with error $\pm 3.0E+01$]
- voltage of the photo multiplier [1700V]

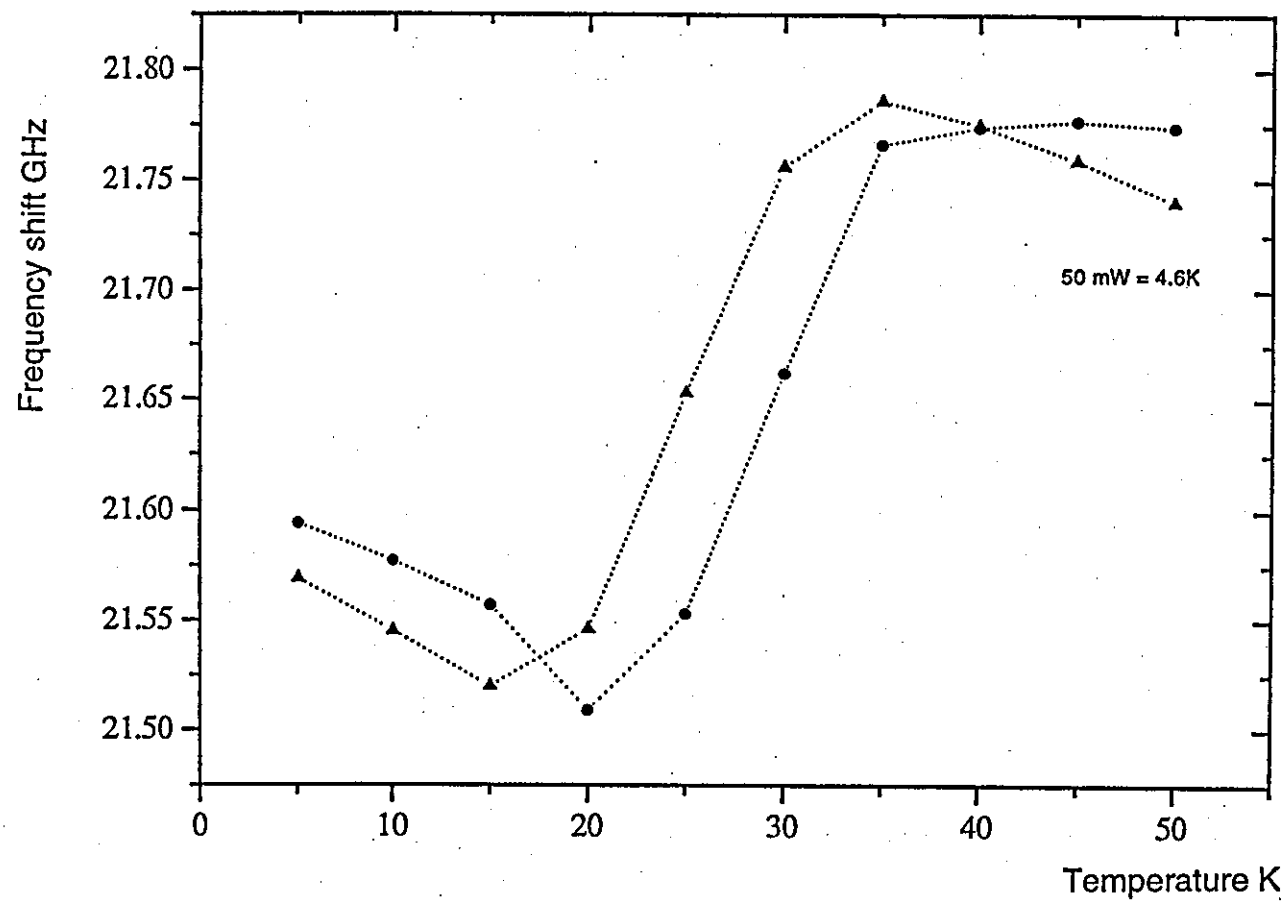


Fig. 3.14 Comparison of laser power 50mW and 100mW

Start 11:44:21 on 4/ 1/1995. 32s (0.064s/channel) 514nm. 50mW. 100mic. 293K.
 2.000mm (75.0 GHz). $\langle f \rangle = 2.06E+04 \pm 3.E+01$. $f(-257)=0.00E-01$ (was 0.00E-01).
 tmbb , +HV=1700V. Newly aligned.
 Calibration : 228.98 3.0E+12. Peak : 0.00E-01 0.00E-01 -16.377 0.000
 chi2/dof= 0.0 0.00E+00 0.00E+00 0.000 0.000

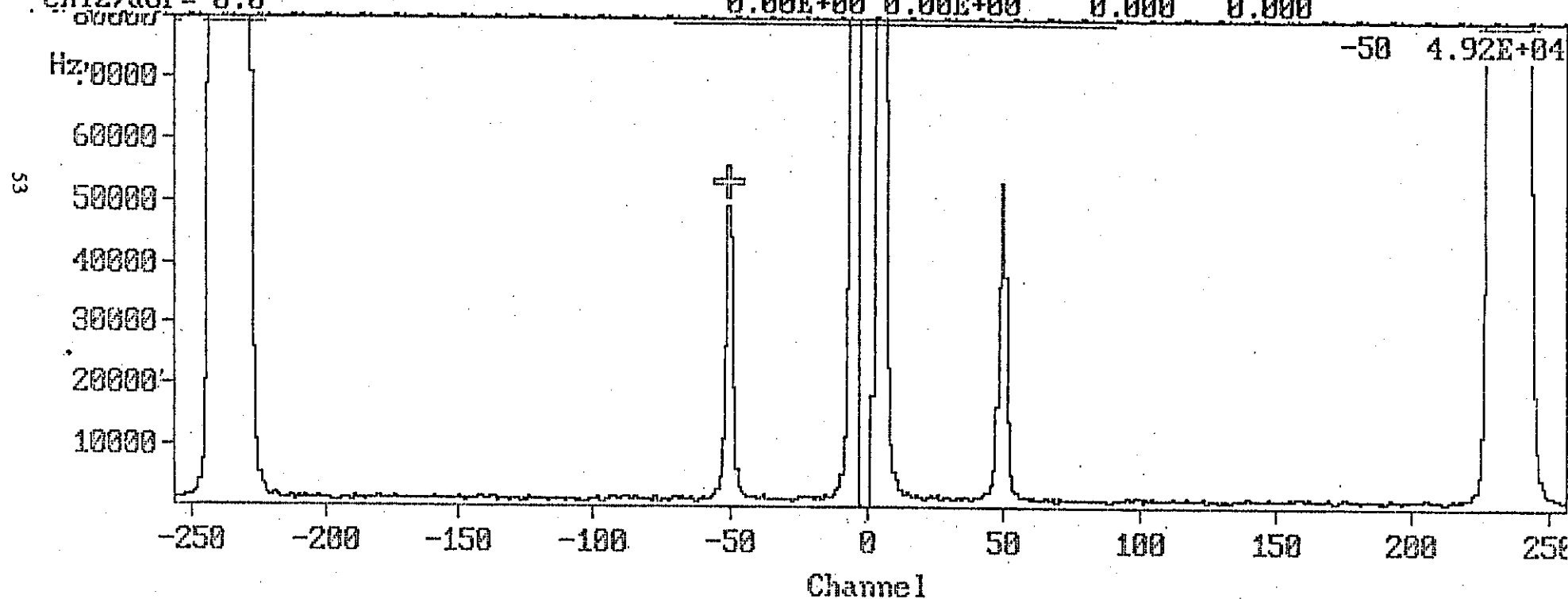


Fig. 3.15 A typical spectrum

3.11 Results:

3.11.1 TMMC, TMMB and TMMC:Cu:

The changes in frequency shift ν of the phonons propagating perpendicular to the c-axis with temperature are listed in Table 3.2-3.4 for TMMC, TMMB and TMMC:Cu. Figure 3.16-3.18 shows the temperature dependence of the longitudinal acoustic phonons frequencies as functions of temperature from 80K to 450K. The Brillouin spectra was reproducible even after several experimental cycles as shown in Figure 3.19. Transition temperatures observed are as shown in Table 3.5.

Table 3.5 Transition temperature observed with Brillouin scattering

Compound	T_{c1} Kelvin	T_{c2} Kelvin
TMMC	129.6	388.6
TMMB	142.6	377.6
TMMC:Cu	108.6	359.6

The values obtained here with the Brillouin scattering technique agrees well with other reported values [Hutchings et. al. 1983, Levola & Laiho 1986, Visser et. al. 1989, Braud et. al. 1990].

Levola & Laiho [1986] claims that doping TMMC with Cu not only shifts the transition temperature but gives rise to other transitions that are at 90K, 124K and 130K. However, our results only show one transition at 108.6K. The effects observed by Levola are probably due to non homogenous doping of TMMC by Cu. Another transition occurs at 359.6K whereas in pure TMMC it occurs at 390K.

The elastic constant which governs the [100] LA mode is C_{11} . The Brillouin shift ν which is given in equation 3.6 is;

$$v = \frac{v}{\lambda} (\eta_i^2 + \eta_s^2 - 2\eta_i\eta_s \cos\phi)^{1/2}$$

where v is the sound velocity and λ the wavelength of the incident light beam. Refractive indices η_i and η_s are defined in the direction of the incident and scattered beam and depend not only on the scattering symmetry employed but also on which phonon mode, LA or TA mode. Here we assumed an isotropic behaviour ($\eta = \eta_i = \eta_s$) throughout. Under these conditions,

$$v = \frac{2\eta v}{\lambda}$$

and the elastic constant $C = \rho v^2 = \rho \left(\frac{v\lambda}{2\eta} \right)^2$

To calculate the velocity of phonons from equation 3.6, the following values of refractive index (room temperature) $\eta_a=1.583$ [Levola 1986] (TMMC), $\eta_a=1.671$ [Janzen 1989] (TMMB) together with the value of $\rho = 1678.6 \text{ kgm}^{-3}$ [Morosin & Graeber 1967] and $\rho=2350 \text{ kgm}^{-3}$ [Alcock & Holt 1972] for TMMC and TMMB respectively. These values will be used to calculate the elastic constant C_{11} as shown in Table 3.2 and 3.3. Figure 3.20 and 3.21 shows the temperature dependence of the elastic constant C_{11} using the back scattering geometry.

We assume that the temperature dependence of density ρ and those of the refractive index compensate each other with an accuracy sufficient for our purpose when calculating C_{11} . We are unable to calculate the elastic constant for TMMC:Cu due to no reported value of refractive index concern. Table 3.6 shows the value of the elastic constant obtained.

Table 3.6: Brillouin scattering measurement made at $\lambda=514.5$ nm at room temperature in TMMC and TMMB for LA phonon (C_{11})

Compound	ν GHz	ν ms ⁻¹	$\rho\nu^2$ (C_{11}) 10 ¹⁰ Nm ⁻²
TMMC	21.805	3543	2.10
TMMB	16.884	2603	1.59

The present value of elastic constant C_{11} for TMMC agrees within 10% with those determined by Hutchings et. al. [1983] and Levola & Laiho [1986]. No values of elastic constant for TMMB have been reported so far.

From the Brillouin scattering results (Figure 3.18, 3.20 and 3.21) of TMMC, TMMB and TMMC:Cu through the $I' \leftrightarrow I$ transition exhibit a marked elastic anomaly at the phase transition $\sim(129.6 \pm 1.0)K$, $(142.6 \pm 1.0)K$ and $(108.6 \pm 1.0)K$ for TMMC, TMMB and TMMC:Cu respectively; consistent with the weakly first order phase transition as reported before [Hutchings et. al. 1983, Levola & Laiho 1985, Braud et. al. 1990, Visser et. al. 1989].

A well defined step-like anomaly of C_{11} was observed at the $I' \leftrightarrow I$ transition temperature in all three compounds studied. The half width (Figure 3.22-3.24) of the Brillouin line exhibits a lambda shaped anomaly at this temperature. Similar results have been obtained for TMMC and TMMC:Cu [Braud et. al.1990, Levola & Laiho 1986] but no results for TMMB have been reported. A step-like variation of C_{11} at the $I' \leftrightarrow I$ transition temperature is characteristic of linear-quadratic coupling existing between the strain components and the order parameter [Rehwald 1973]. A linear temperature dependence is observed for temperatures between 300 and 380K, as well above 400K.

The phase transition $I' \leftrightarrow I$ is confirmed to be continuous (nearly continuous) by Braud et. al. [1990]. Weissenberg photographs, containing reflections from (hk1), (h1l) or (1kl) planes shows that

reflections of the hhl type with odd l are present in phase I but disappear in phase I'. Then, the space group of phase I' is unambiguously determined as $P6_3/mmc$ ($Z=2$) i.e. a subgroup of $P6_3/m$ (phase I), as it should be of the transition $I' \leftrightarrow I$ is of second order.

Table 3.2: Frequency shift (ν), Full width half maximum (FWHM) and elastic constant (C_{11}) obtained from Brillouin scattering experiment for TMMC

Temp. K	$-\nu$ GHz	$+\nu$ GHz	ν GHz	FWHM MHz	$C_{11} \times 10^{10} \text{ Nm}^{-2}$
90	21.868	21.910	21.889	1369	2.122
92	21.633	21.856	21.775	1189	2.100
100	21.632	21.801	21.717	1378	2.089
105	21.557	21.752	21.657	1456	2.077
110	21.543	21.657	21.600	1296	2.066
115	21.436	21.464	21.450	1497	2.038
120	21.067	21.199	21.133	878	1.978
125	21.031	21.072	21.052	800	1.963
130	21.054	21.159	21.107	758	1.973
135	21.037	21.243	21.140	717	1.979
140	21.105	21.309	21.207	745	1.992
150	21.172	21.365	21.269	706	2.004
160	21.363	21.449	21.406	805	2.029
170	21.395	21.431	21.413	611	2.031
180	21.355	21.537	21.446	779	2.057
190	21.459	21.643	21.551	694	2.072
200	21.647	21.717	21.632	728	2.078
210	21.575	21.746	21.661	791	2.080
220	21.584	21.753	21.669	793	2.101
230	21.646	21.918	21.782	708	2.104
240	21.708	21.875	21.792	791	2.097
250	21.664	21.857	21.761	866	2.101
260	21.713	21.847	21.780	848	2.109
270	21.761	21.885	21.823	748	2.1-3
280	21.713	21.873	21.793	718	2.109
285	21.762	21.879	21.821	720	2.110
290	21.748	21.907	21.828	782	2.113
295	21.748	21.931	21.840	836	2.108
300	21.723	21.913	21.818	816	2.089
305	21.666	21.772	21.719	759	2.092
310	21.686	21.780	21.733	739	2.101
315	21.730	21.832	21.781	765	2.098
320	21.708	21.823	21.766	829	2.089
325	21.662	21.778	21.720	708	2.085

continue (Table 3.2)

330	21.606	21.784	21.695	807	2.082
335	21.613	21.746	21.680	850	2.083
340	21.589	21.783	21.686	809	2.081
345	21.596	21.754	21.675	782	2.072
350	21.554	21.700	21.627	824	2.065
360	21.531	21.660	21.596	865	2.066
365	21.521	21.626	21.574	945	2.061
370	21.516	21.580	21.548	860	2.056
375	21.470	21.551	21.511	925	2.049
380	21.540	21.575	21.558	956	2.058
385	21.498	21.578	21.538	995	2.055
390	21.572	21.681	21.627	1046	2.072
395	21.666	21.809	21.738	756	2.093
400	21.699	21.823	21.761	787	2.097
405	21.674	21.844	21.759	743	2.097
410	21.699	21.832	21.766	826	2.098
415	21.670	21.821	21.746	754	2.094
420	21.634	21.785	21.710	725	2.087
425	21.582	21.745	21.664	767	2.079
430	21.633	21.783	21.708	692	2.087
435	21.659	21.745	21.702	785	2.086
440	21.573	21.699	21.621	676	2.070
445	21.669	21.632	21.651	756	2.076
450	21.636	21.715	21.676	722	2.081

Table 3.3: Frequency shift (ν), Full width half maximum (FWHM) and elastic constant (C_{11}) obtained from Brillouin scattering experimet for TMMB

Temp. K	$-\nu$ GHz	$+\nu$ GHz	ν GHz	FWHM MHz	$C_{11} \times 10^{10} \text{ Nm}^{-2}$
100	16.564	16.628	16.596	605	1.534
105	16.291	16.651	16.471	657	1.511
110	16.363	16.534	16.449	620	1.507
115	16.631	16.530	16.446	604	1.507
120	16.343	16.526	16.434	634	1.504
124	16.408	16.404	16.412	600	1.500
126	16.404	16.412	16.395	654	1.497
130	16.330	16.438	16.371	668	1.493
132	16.186	16.394	16.290	683	1.478
136	16.262	16.309	16.286	887	1.477
138	16.304	16.438	16.234	668	1.468
150	16.329	16.488	16.409	726	1.499
160	16.441	16.424	16.433	721	1.504
170	16.542	16.756	16.649	547	1.528
180	16.598	16.642	16.620	667	1.539
190	16.589	16.818	16.704	707	1.554
200	16.717	16.937	16.827	775	1.577
210	16.726	16.911	16.819	660	1.575
220	16.789	16.941	16.865	703	1.584
230	16.878	16.945	16.866	560	1.584
240	16.848	16.981	16.915	532	1.594
250	16.821	16.965	16.893	612	1.589
260	16.824	16.958	16.891	598	1.589
270	16.817	16.954	16.886	609	1.588
280	16.854	16.936	16.895	571	1.589
290	16.820	16.942	16.881	613	1.587
300	16.847	16.921	16.884	574	1.587
305	16.861	16.830	16.846	595	1.580
320	16.877	16.855	16.866	485	1.584
325	16.846	16.842	16.844	463	1.580
330	16.896	16.891	16.894	446	1.589
335	16.849	16.849	16.849	464	1.581
340	16.824	16.806	16.815	641	1.574
343	16.835	16.834	16.835	496	1.578
346	16.807	16.821	16.814	564	1.575
349	16.791	16.826	16.809	482	1.574
352	16.786	16.791	16.789	580	1.570
355	16.766	16.786	16.776	541	1.568

continue (Table 3.3)

358	16.783	16.767	16.775	597	1.567
361	16.756	16.781	16.769	579	1.566
367	16.733	16.743	16.738	620	1.560
370	16.726	16.729	16.728	666	1.559
373	16.697	16.685	16.691	723	1.551
376	16.718	16.709	16.714	729	1.556
379	16.790	16.797	16.794	680	1.571
382	16.821	16.797	16.809	618	1.574
385	16.813	16.884	16.849	590	1.581
388	16.853	16.853	16.853	492	1.582
391	16.802	16.881	16.842	562	1.579
394	16.825	16.865	16.845	469	1.581
397	16.820	16.842	16.831	444	1.578
400	16.833	16.869	16.851	485	1.581
403	16.812	16.861	16.837	465	1.579
406	16.800	16.836	16.818	479	1.575

Table 3.4: Frequency shift (ν) and Full width half maximum (FWHM) obtained from Brillouin scattering experiments for TMMC:Cu

Temp. K	$-\nu$ GHz	$+\nu$ GHz	ν GHz	FWHM MHz
85	22.447	22.250	22.349	1832
90	22.105	22.304	22.205	1851
95	21.661	21.929	21.795	1108
98	21.416	21.537	21.477	602
100	21.482	21.415	21.449	809
104	21.358	21.474	21.414	586
110	21.312	21.542	21.427	563
115	21.332	21.581	21.457	519
120	21.334	21.648	21.491	554
125	21.378	21.745	21.562	568
128	21.518	21.721	21.620	536
134	21.616	21.754	21.685	518
140	21.606	21.789	21.698	513
146	21.654	21.841	21.746	582
152	21.609	21.892	21.751	441
158	21.683	21.841	21.762	630
164	21.745	21.932	21.839	513
170	21.716	21.914	21.815	496
176	21.741	21.940	21.841	419
182	21.789	21.971	21.880	504
186	21.877	21.944	21.911	461
188	21.850	22.014	21.932	526
200	21.895	22.048	21.972	525
206	21.876	22.053	21.965	493
212	21.890	22.077	21.984	548
218	21.963	22.006	21.985	473
221	21.961	22.016	21.989	487
228	21.964	21.933	21.949	593
230	22.003	21.999	22.001	535
235	21.960	22.063	22.012	494
236	21.964	22.012	21.988	443
242	21.931	22.125	22.029	512
248	21.982	21.997	21.990	490
249	21.923	22.041	21.982	441
254	21.984	21.999	21.992	576
256	21.909	22.033	21.972	485
260	21.982	21.963	21.974	464
263	21.982	22.051	22.016	444
266	21.965	22.117	22.041	509
270	21.898	22.029	21.964	503

Continue (Table 3.4)

272	21.888	21.982	21.935	568
278	21.953	21.971	21.962	603
280	21.926	22.061	21.994	567
284	21.910	21.949	21.930	469
290	21.860	21.934	21.897	599
298	21.941	21.990	21.966	503
300	21.827	22.040	21.934	503
302	21.892	21.979	21.936	543
304	21.795	22.000	21.898	537
308	21.752	22.072	21.912	515
312	21.820	21.986	21.903	535
316	21.798	21.967	21.883	556
320	21.797	21.913	21.855	558
324	21.768	21.866	21.817	559
328	21.730	21.843	21.787	641
332	21.688	21.861	21.775	601
336	21.676	21.848	21.762	597
340	21.720	21.834	21.777	653
344	21.679	21.794	21.737	735
347	21.658	21.802	21.730	814
352	21.663	21.783	21.723	788
356	21.564	21.745	21.655	718
360	21.710	21.847	21.779	764
364	21.755	21.927	21.841	773
368	21.844	22.043	21.944	509
372	21.832	22.044	21.938	516
376	21.793	21.993	21.893	541
382	21.844	22.003	21.924	536
384	21.794	22.024	21.909	461
388	21.765	21.975	21.870	472
392	21.759	21.954	21.857	479
396	21.761	21.932	21.847	489
400	21.737	21.937	21.835	518
404	21.725	21.911	21.818	483
408	21.749	21.910	21.830	488
412	21.706	21.898	21.802	555
416	21.641	21.907	21.774	539
420	21.573	21.902	21.738	526
424	21.611	21.750	21.681	488
430	21.596	21.793	21.695	507
440	21.511	21.856	21.684	532

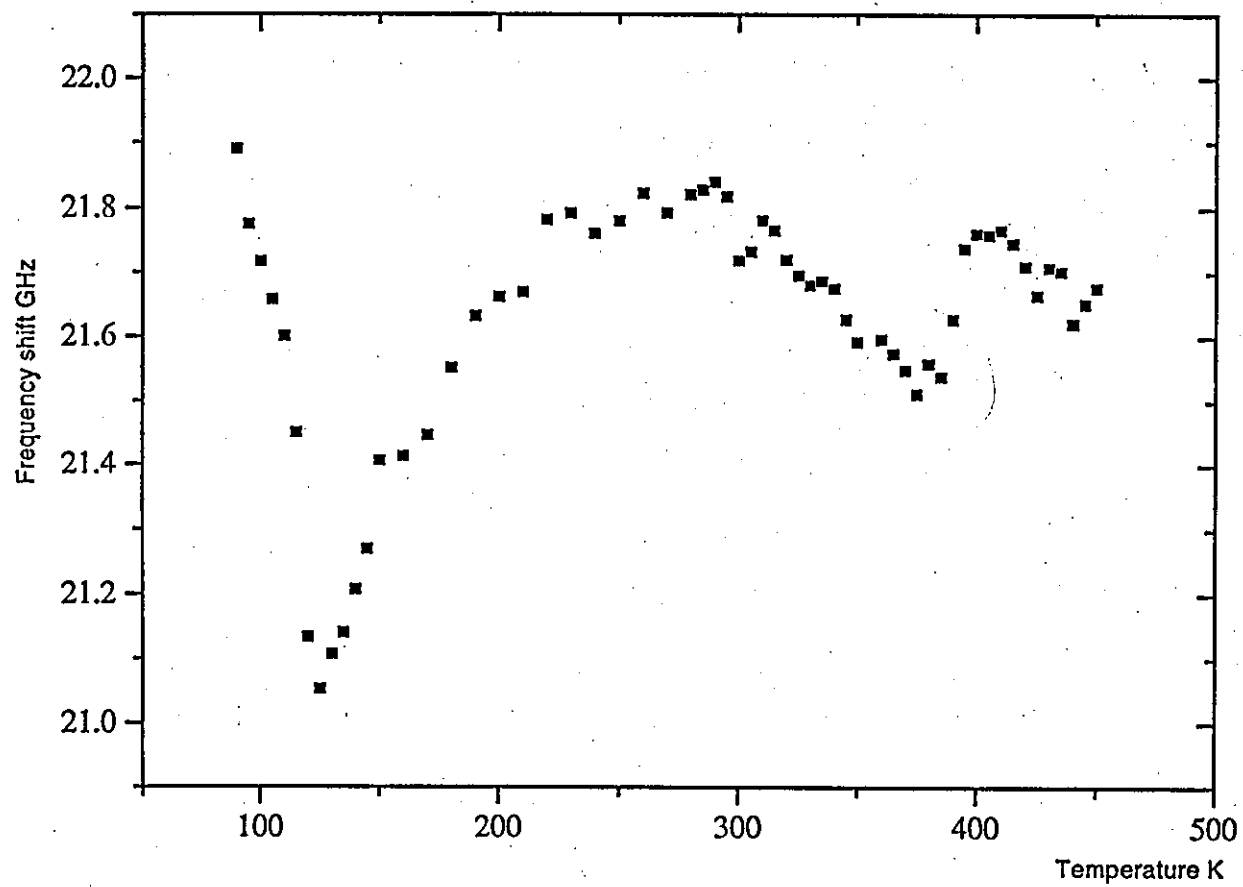


Fig. 3.16 Frequency shift vs temperature for TMMC

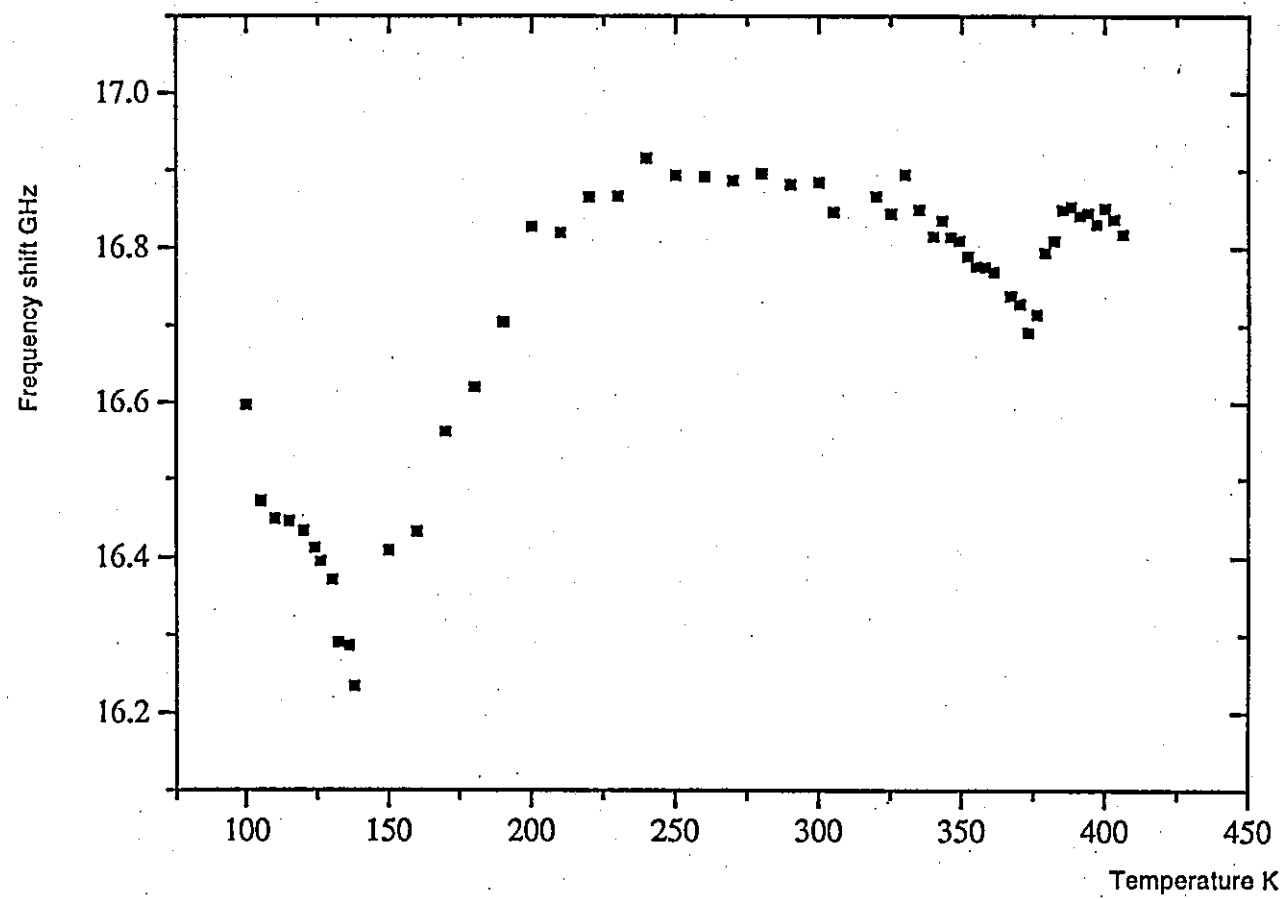


Fig. 3.17 Frequency shift vs temperature for TMMB

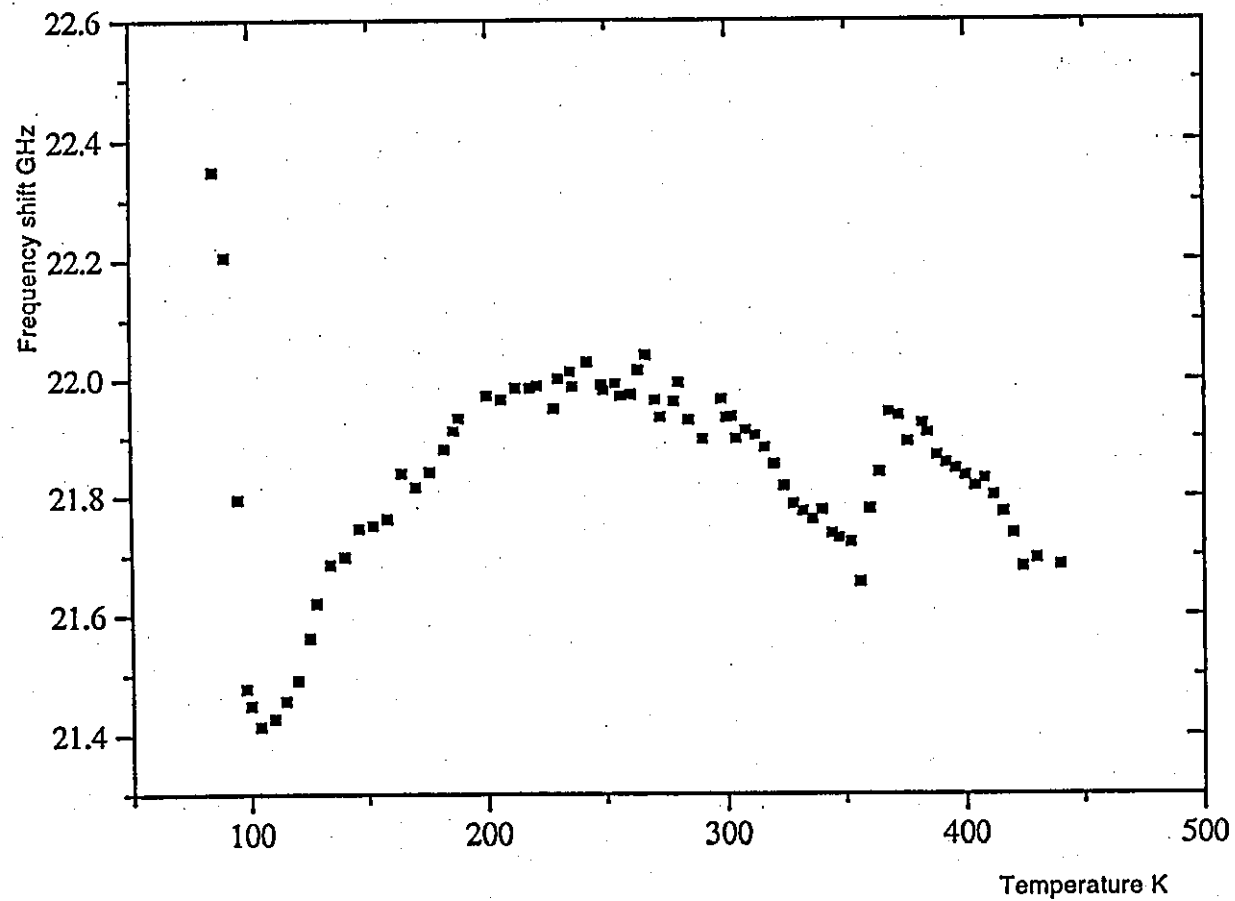


Fig. 3.18 Frequency shift vs temperature for TMMC:Cu

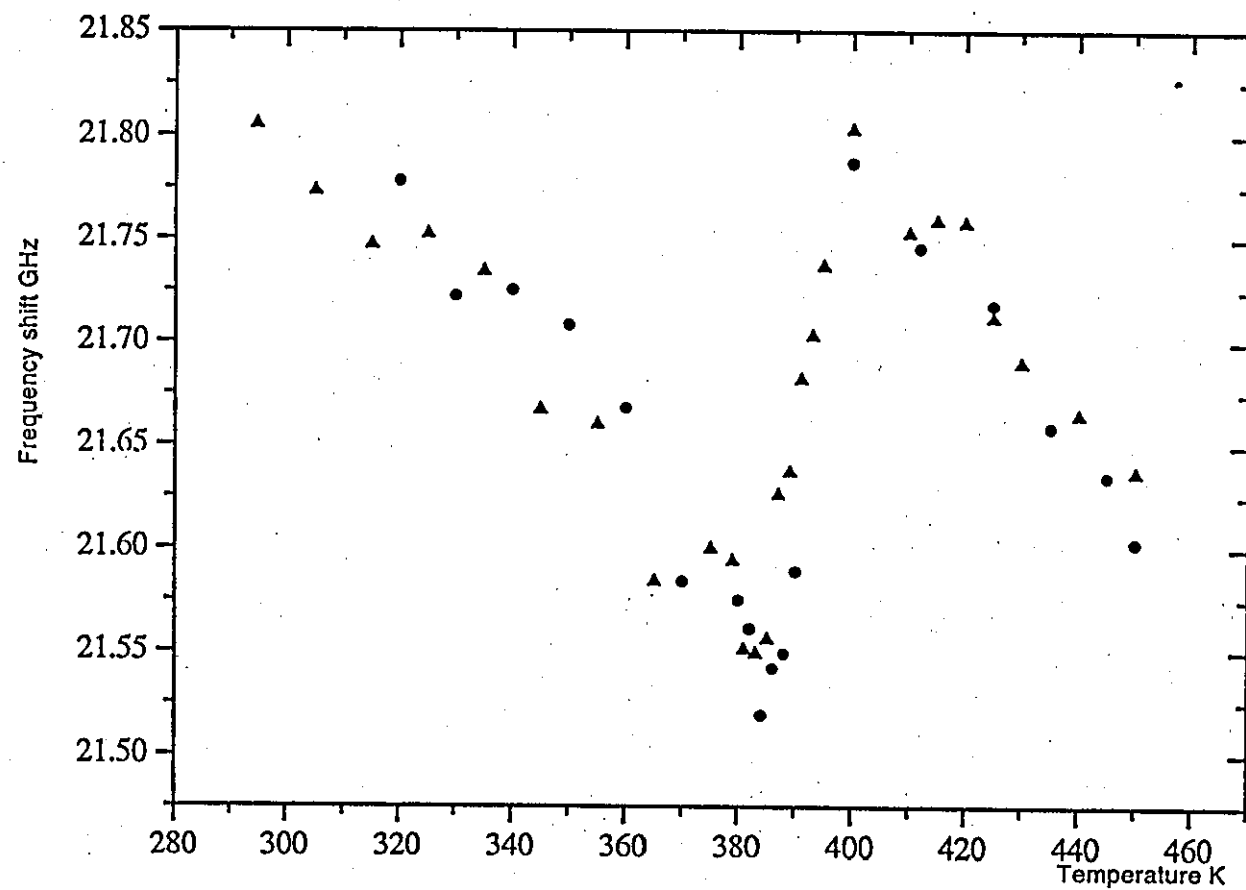


Fig. 3.19 Temperature dependence of the LA phonon for repeated measurements and the result are presented by different symbols

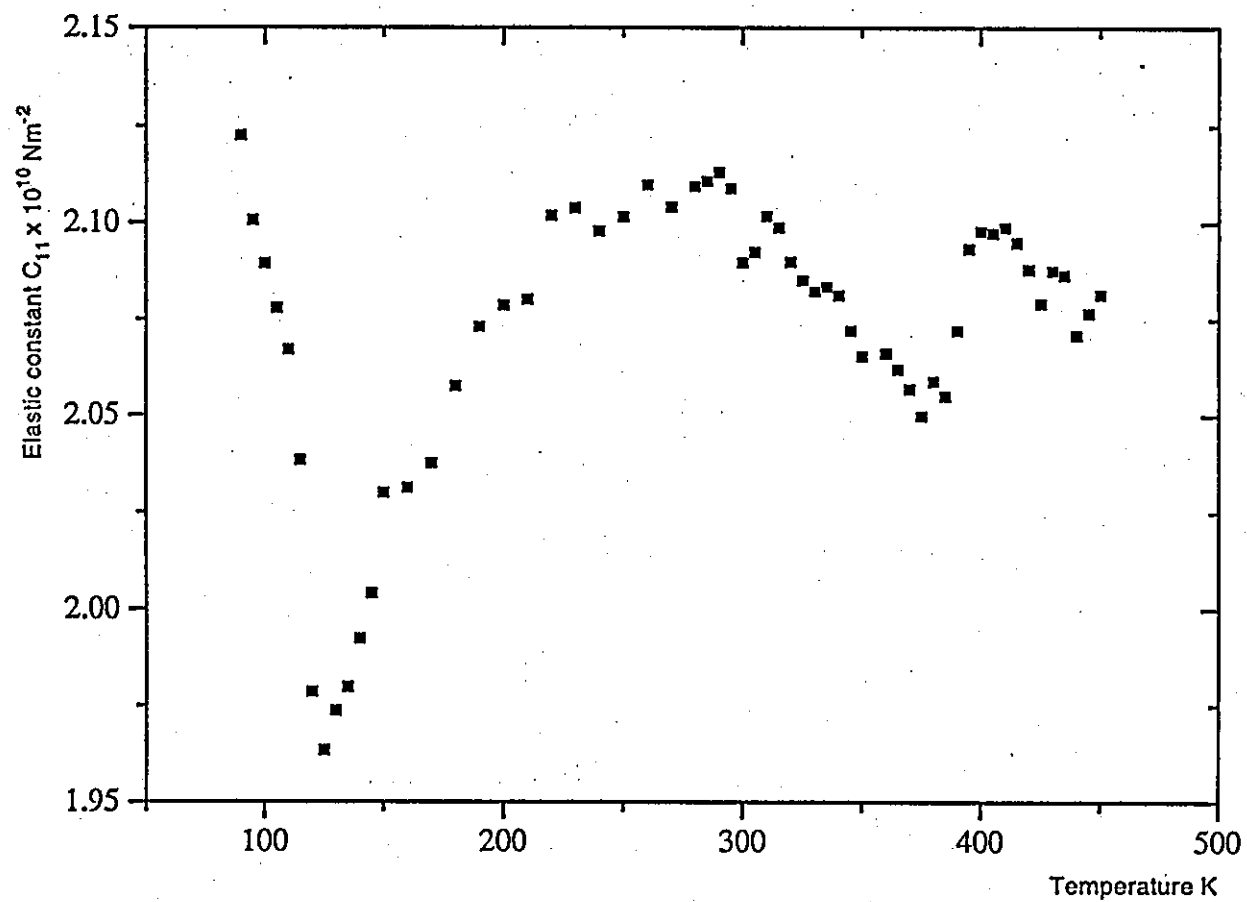


Fig. 3.20 Temperature dependence of elastic constant C_{11} for TMMC

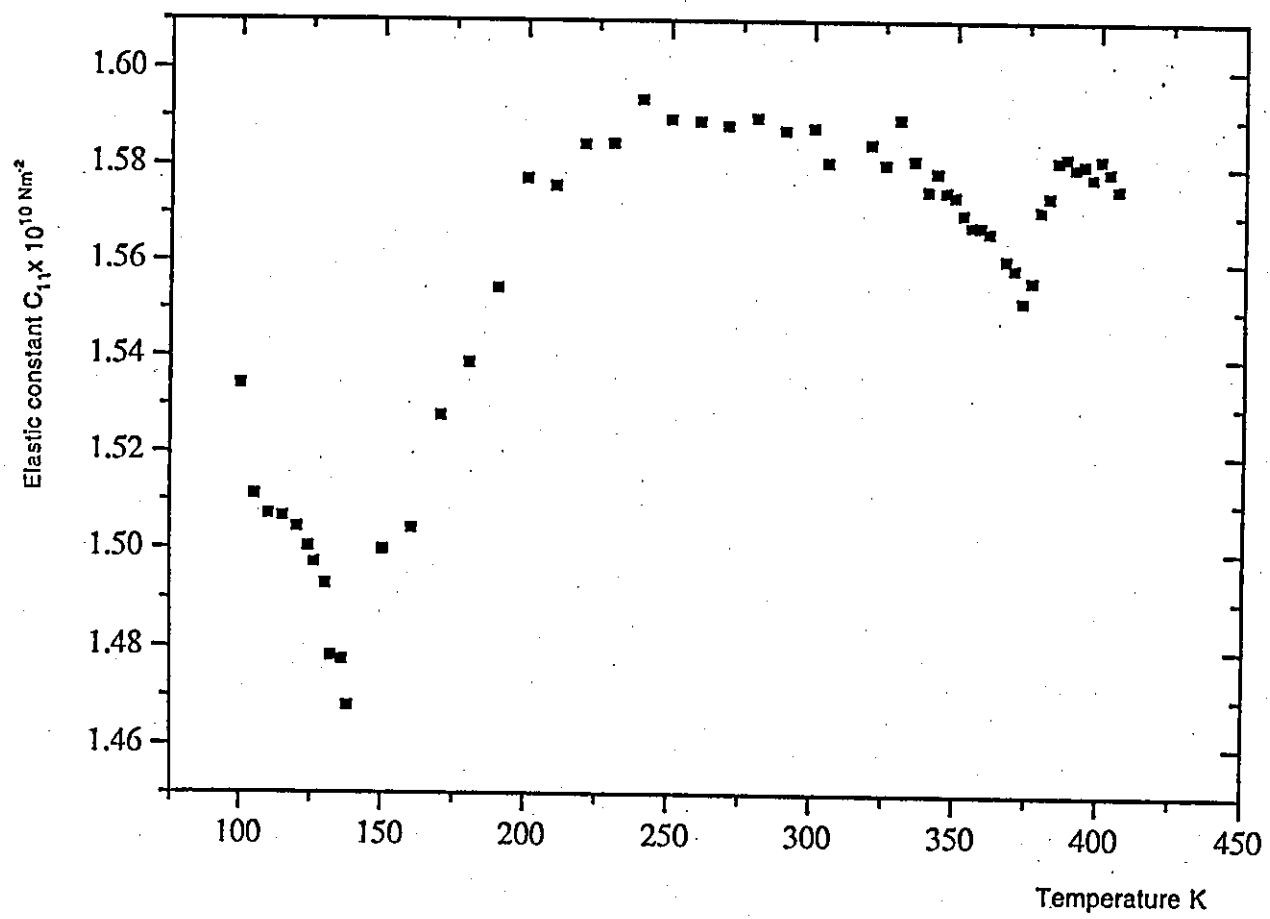


Fig. 3.21 Temperature dependence of elastic constant C_{11} for TMMB

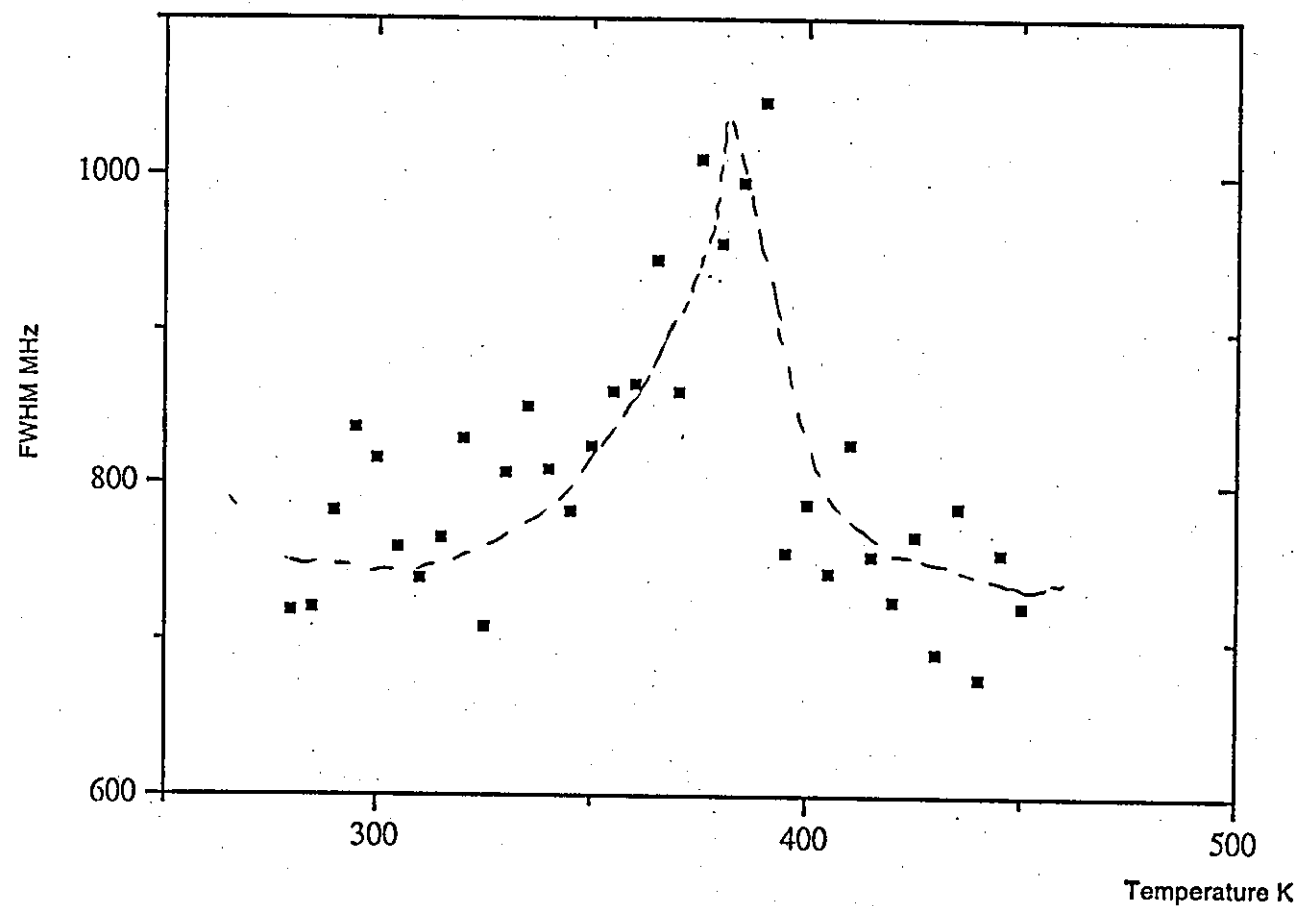


Fig. 3.22 Full width half maximum (FWHM) of the Brillouin peak corresponding to the elastic constant C_{11} of TMMC (line as guide to the eye)

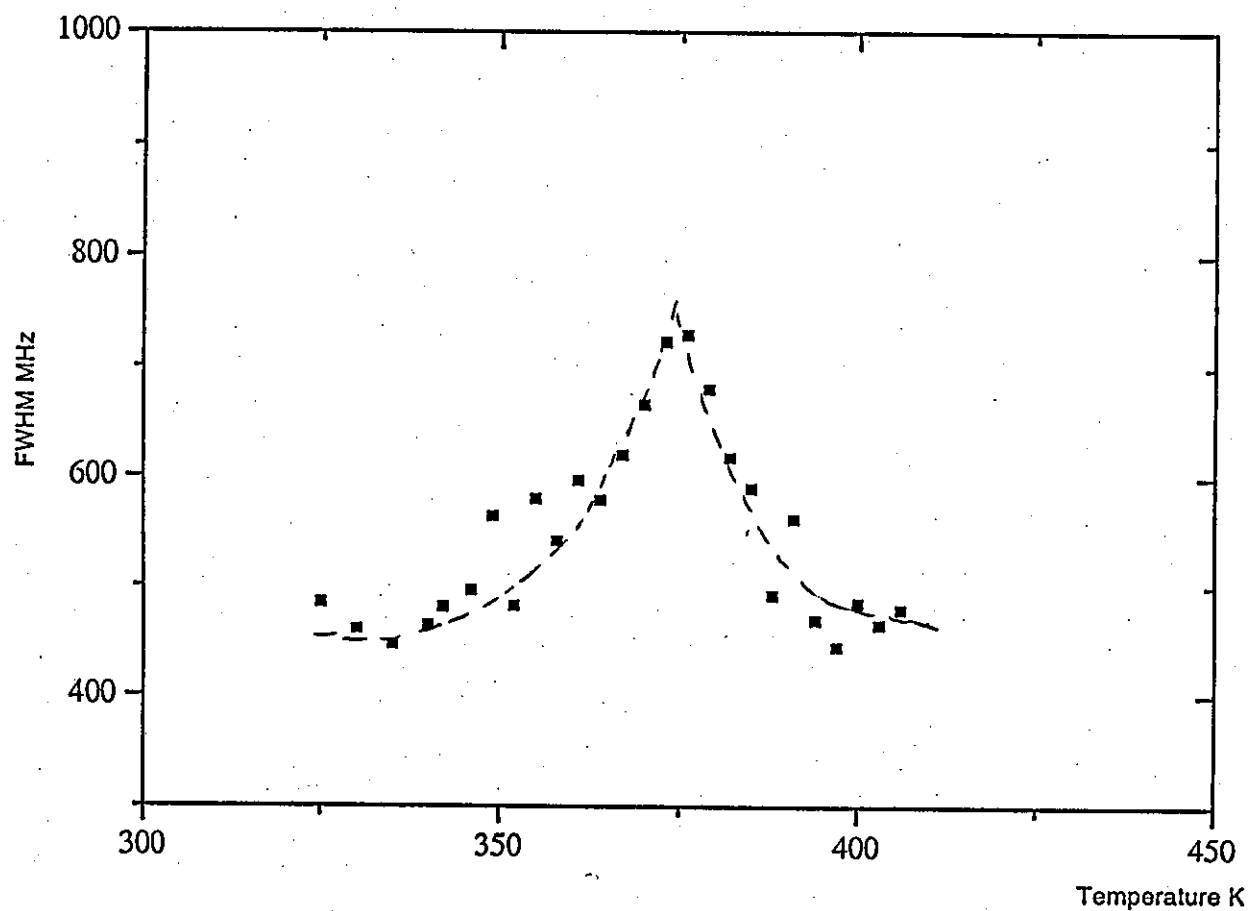


Fig. 3.23 Full width half maximum (FWHM) of the Brillouin peak corresponding to the elastic constant C_{11} of TMMB (line as guide to the eye)

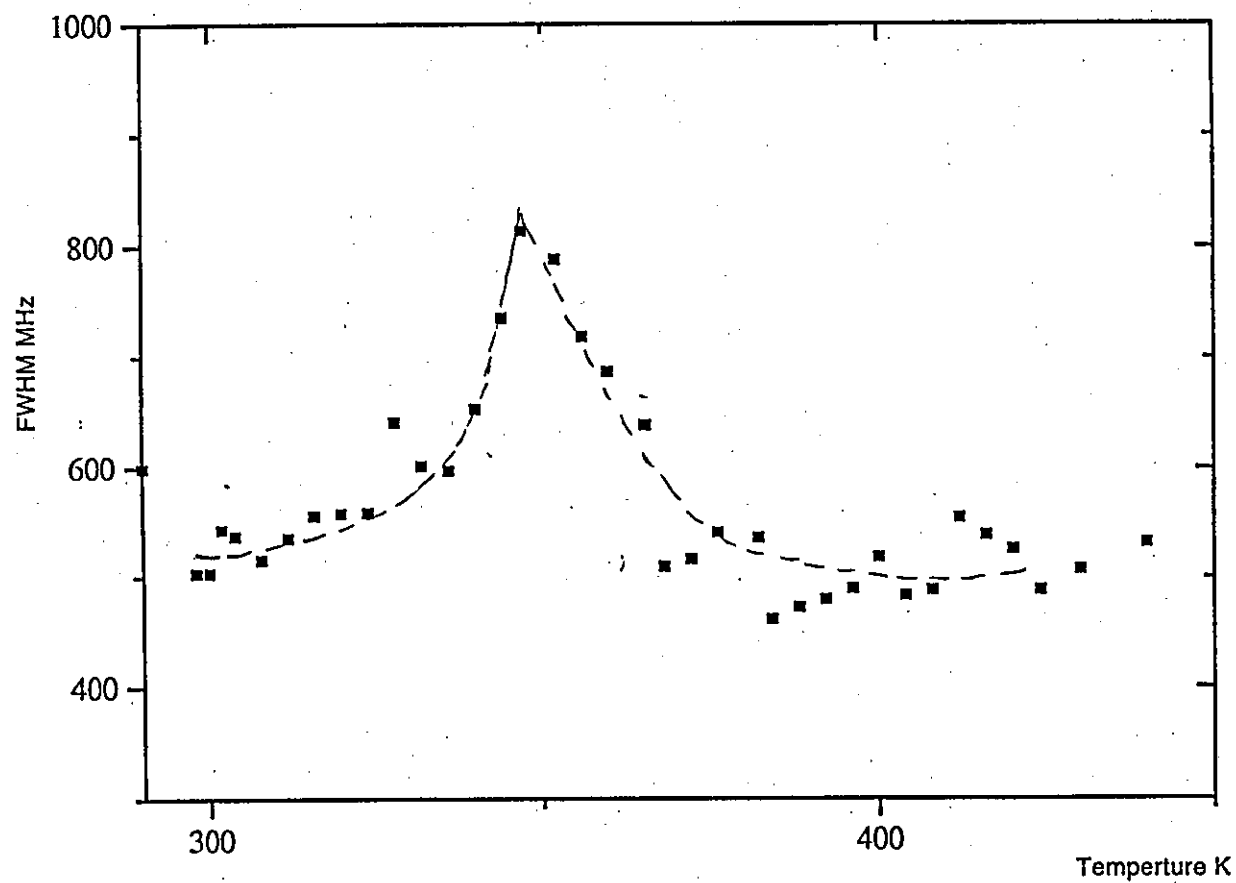


Fig. 3.24 Full width half maximum (FWHM) of the Brillouin peak corresponding to the elastic constant C_{11} of TMMC:Cu (line as guide to the eye)

3.11.2 RbNiCl₃ and CsNiCl₃:

The changes in frequency shift of the phonons propagating parallel and perpendicular to the c-axis with temperature are listed in Table 3.7-3.10.

Figure 3.25 and 3.26 presents the phonons frequencies in two direction (parallel and perpendicular to the c-axis) as a function of temperature from 80K to 450K. As can be seen from those figures, the [100] and [001] LA mode is governed by elastic constants C_{11} and C_{33} respectively. It exhibits only a monotonic and weak decrease in frequency as the temperature is increased.

Here again we assume an isotropic behaviour ($\eta=\eta_l=\eta_s$). The value of refractive index and density ρ used to calculate the sound velocity in RbNiCl₃ and CsNiCl₃ are as shown in Table 3.11 [Iio 1980]. Calculated elastic constant for both compounds are as shown in Table 3.7 - 3.10.

Table 3.11: Refractive index and density of CsNiCl₃ and RbNiCl₃ at room temperature

Compound	n_a	n_c	ρ kgm ⁻³
RbNiCl ₃	1.678	1.783	3505
CsNiCl ₃	1.707	1.797	3886

Figure 3.27 and 3.28 shows the temperature dependence of the elastic constant C_{11} and C_{33} for RbNiCl₃ and CsNiCl₃. The value of the elastic constant at room temperature is tabulated in Table 3.12.

Table 3.12: Brillouin scattering measurement made at $\lambda = 515.4$ nm and at room temperature in RbNiCl₃ and CsNiCl₃

Compound	Mode	ν GHz	V ms ⁻¹	$\rho V^2(C_{11}) \times 10^{10} \text{Nm}^{-2}$
RbNiCl ₃	C_{11} (L)	21.753	3317	3.86
	C_{33} (L)	27.794	4010	5.64
CsNiCl ₃	C_{11} (L)	21.075	3176	3.92
	C_{33} (L)	27.091	3878	5.84

Elastic constant of CsNiCl_3 has been measured using a phase comparison method [Mountfield & Rayne1981]. The value of the elastic constant at room temperature is reported as $C_{11}=3.58$ and $C_{33} = 6.25$ in units of 10^{10} Nm^{-2} . This value seems to agree quite well with the values obtain with our Brillouin scattering measurements.

Table 3.7: Frequency shift (ν) and elastic constant (C_{33}) obtained from Brillouin scattering experiments for RbNiCl_3 (parallel to the chain axis)

Temp.K	$-\nu$ GHz	$+\nu$ GHz	ν GHz	$C_{33} \times 10^{10} \text{ Nm}^{-2}$
80	28.535	28.478	28.507	5.929
90	28.386	28.313	28.350	5.864
100	28.244	28.372	28.308	5.847
110	28.326	28.258	28.292	5.840
120	28.188	28.210	28.199	5.802
130	28.308	27.991	28.150	5.781
140	28.162	28.209	28.186	5.796
150	28.143	28.220	28.182	5.795
160	28.169	28.253	28.211	5.807
170	28.258	28.214	28.236	5.817
180	28.127	27.152	28.140	5.777
190	28.257	28.145	28.201	5.802
200	28.171	28.237	28.204	5.816
210	28.084	28.162	28.123	5.770
220	27.997	28.108	28.053	5.742
230	27.943	28.086	28.015	5.726
240	28.011	28.015	28.013	5.725
250	27.930	28.113	28.022	5.729
260	27.949	28.032	27.991	5.716
270	27.859	27.869	27.864	5.665
280	27.820	27.741	27.781	5.631
290	27.812	27.776	27.794	5.636
300	27.749	27.802	27.776	5.629
304	27.661	27.674	27.668	5.585
312	27.639	27.663	27.651	5.578
320	27.619	27.628	27.624	5.567
328	27.555	27.541	27.548	5.537
336	27.517	27.585	27.551	5.538
344	27.527	27.468	27.498	5.517
354	27.480	27.444	27.462	5.502
364	27.421	27.387	27.404	5.479
374	27.382	27.369	27.376	5.468
384	27.348	27.412	27.380	5.469
394	27.377	27.261	27.319	5.445
404	27.343	27.338	27.341	5.454
414	27.271	27.255	27.263	5.423
424	27.332	27.261	27.297	5.436

Table 3.8: Frequency shift (ν) and elastic constant (C_{11}) obtained from Brillouin scattering experiment for RbNiCl_3 (perpendicular to the chain axis)

Temp K	$-\nu$ GHz	$+\nu$ GHz	ν GHz	$C_{11} \times 10^{10} \text{ Nm}^{-2}$
116	22.892	23.005	22.949	4.338
126	22.873	22.941	22.910	4.323
136	22.777	22.881	22.829	4.293
146	22.720	22.813	22.767	4.269
156	22.669	22.750	22.710	4.248
166	22.615	22.643	22.629	4.217
176	22.557	22.608	22.583	4.201
186	22.663	22.537	22.585	4.202
196	22.588	22.460	22.524	4.179
206	22.457	22.484	22.471	4.159
216	22.344	22.438	22.391	4.129
226	22.390	22.357	22.374	4.123
236	22.284	22.222	22.253	4.079
246	22.164	22.039	22.102	4.024
256	22.023	22.106	22.065	4.010
266	21.924	21.945	21.935	3.963
276	21.833	21.821	21.827	3.924
286	21.868	21.759	21.814	3.919
296	21.802	21.704	21.753	3.897
307	21.723	21.498	21.611	3.847
317	21.549	21.374	21.462	3.794
327	21.461	21.304	21.383	3.766
337	21.362	21.187	21.275	3.728
347	21.215	21.133	21.174	3.693
357	21.205	21.136	21.171	3.692
367	21.198	21.027	21.113	3.672
377	21.018	20.918	20.968	3.612
387	20.932	21.034	20.983	3.627
397	20.879	20.869	20.874	3.589
407	20.793	20.865	20.829	3.574
417	20.773	20.779	20.776	3.555
427	20.745	20.635	20.690	3.526
437	20.690	20.731	20.711	3.533
447	20.523	20.634	20.579	3.488

Table 3.9: Frequency shift (ν) and elastic constant (C_{11}) obtained from Brillouin scattering experiment for CsNiCl_3 (parallel to the chain axis)

Temp. K	$-\nu$ GHz	$+\nu$ GHz	ν GHz	$C_{33} \times 10^{10}\text{Nm}^{-2}$
77	27.750	27.948	27.849	6.177
87	27.747	27.922	27.835	6.170
97	27.572	27.947	27.760	6.137
107	27.608	27.905	27.757	6.136
117	27.646	27.911	27.779	6.146
127	27.528	27.870	27.699	6.110
137	27.509	27.834	27.672	6.098
147	27.535	27.741	27.638	6.083
157	27.520	27.734	27.627	6.079
167	27.551	27.645	27.598	6.066
177	27.527	27.671	27.557	6.048
187	27.354	27.647	27.521	6.032
197	27.449	27.590	27.520	6.031
207	27.422	27.605	27.514	6.029
217	27.316	27.547	27.432	5.993
227	27.366	27.462	27.414	5.985
237	27.273	27.479	27.376	5.969
247	27.313	27.518	27.416	5.986
257	27.147	27.425	27.286	5.929
267	27.204	27.242	27.223	5.902
277	27.265	27.279	27.272	5.923
287	27.069	27.187	27.128	5.861
297	26.987	27.194	27.091	5.845
299	26.991	27.256	27.124	5.859
305	27.118	27.261	27.190	5.888
311	27.092	27.239	27.166	5.877
317	27.049	27.305	27.177	5.882
323	26.979	27.278	27.129	5.861
329	26.944	27.205	27.075	5.838
335	26.908	27.224	27.066	5.834
341	26.917	27.210	27.064	5.833
347	26.752	27.155	26.954	5.786
353	26.695	27.131	26.913	5.768
359	26.668	27.098	26.883	5.756
365	26.597	27.024	26.811	5.725
371	26.669	27.101	26.846	5.740
377	26.599	27.083	26.841	5.738
383	26.865	27.134	26.959	5.788
389	26.665	26.924	26.795	5.718
395	26.684	27.046	26.865	5.748
401	26.565	27.026	26.796	5.718

Table 3.10: Frequency shift (ν) and elastic constant (C_{33}) obtained from Brillouin scattering experiment for CsNiCl_3 (perpendicular to chain axis)

Temp. K	$-\nu$ GHz	$+\nu$ GHz	ν GHz	$C_{11} \times 10^{10} \text{ Nm}^{-2}$
80	22.178	22.180	22.179	4.342
90	22.311	22.264	22.288	4.384
105	22.284	22.043	22.134	4.324
120	22.099	22.099	22.099	4.310
135	21.850	22.074	21.962	4.257
150	21.892	21.997	21.945	4.250
165	21.780	21.734	21.757	4.178
180	21.704	21.865	21.785	4.189
195	21.739	21.666	21.703	4.157
210	21.538	21.532	21.535	4.093
225	21.471	21.547	21.509	4.083
240	21.435	21.463	21.449	4.060
255	21.364	21.367	21.366	4.029
270	21.177	21.193	21.185	3.961
285	21.135	21.148	21.142	3.945
300	20.978	21.172	21.075	3.920
306	21.037	20.934	20.986	3.887
316	20.975	20.925	20.950	3.874
326	20.913	20.846	20.880	3.848
336	20.894	20.784	20.839	3.833
346	20.694	20.672	20.683	3.776
356	20.686	20.680	20.681	3.775
366	20.603	20.659	20.631	3.757
376	20.556	20.608	20.582	3.739
386	20.519	20.603	20.561	3.731
396	20.351	20.415	20.383	3.667
406	20.364	20.407	20.386	3.668
416	20.320	20.377	20.349	3.656
426	20.088	20.357	20.223	3.609
436	20.155	20.241	20.198	3.601

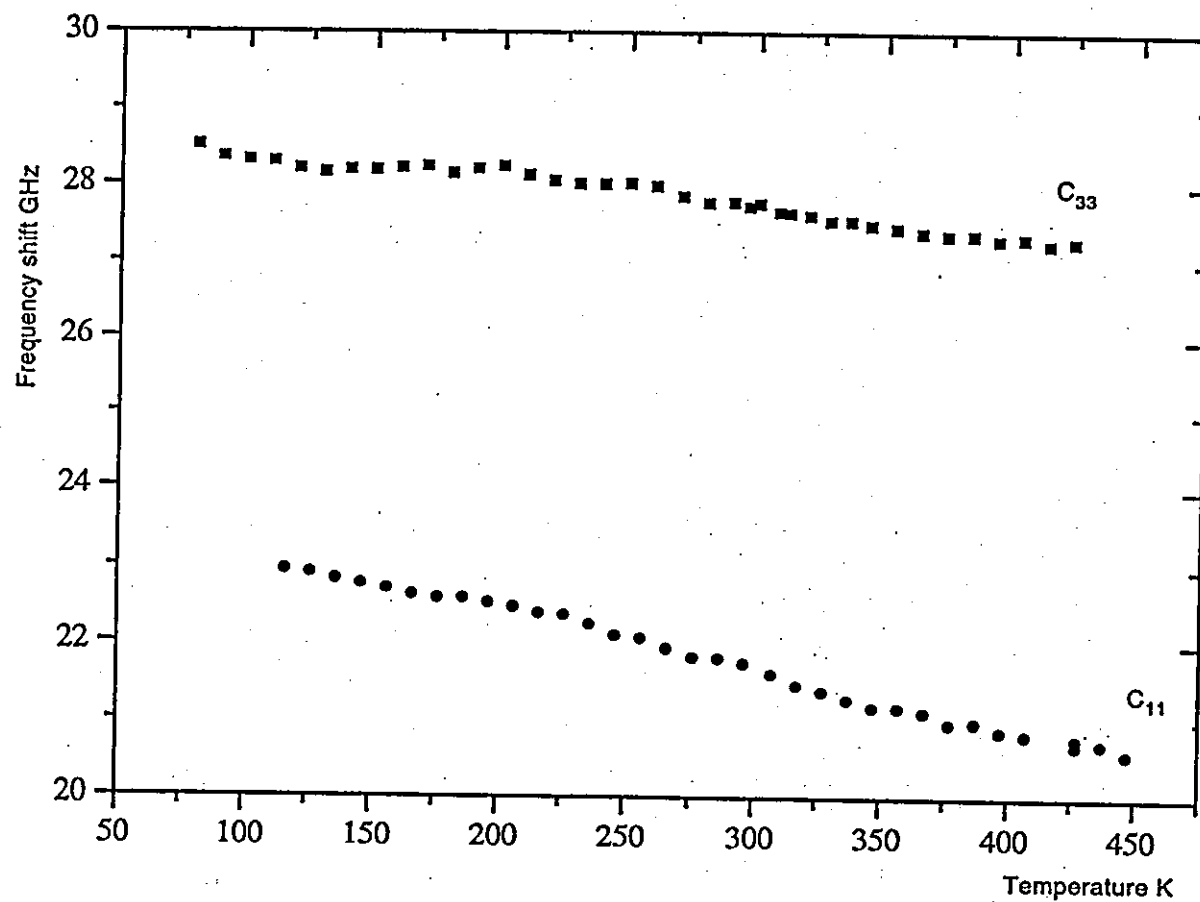


Fig. 3.25 Frequency shift vs temperature for RbNiCl_3

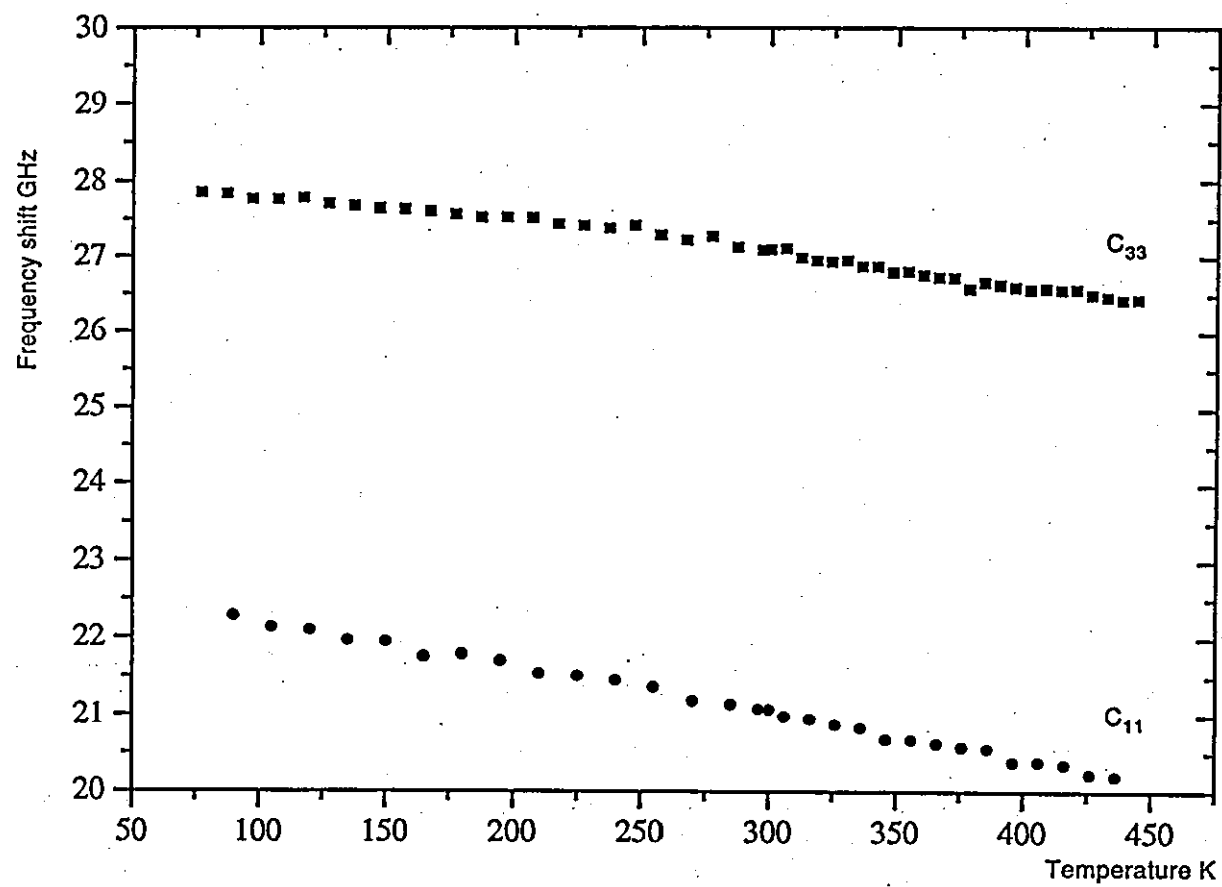


Fig. 3.26 Frequency shift vs temperature for CsNiCl_3

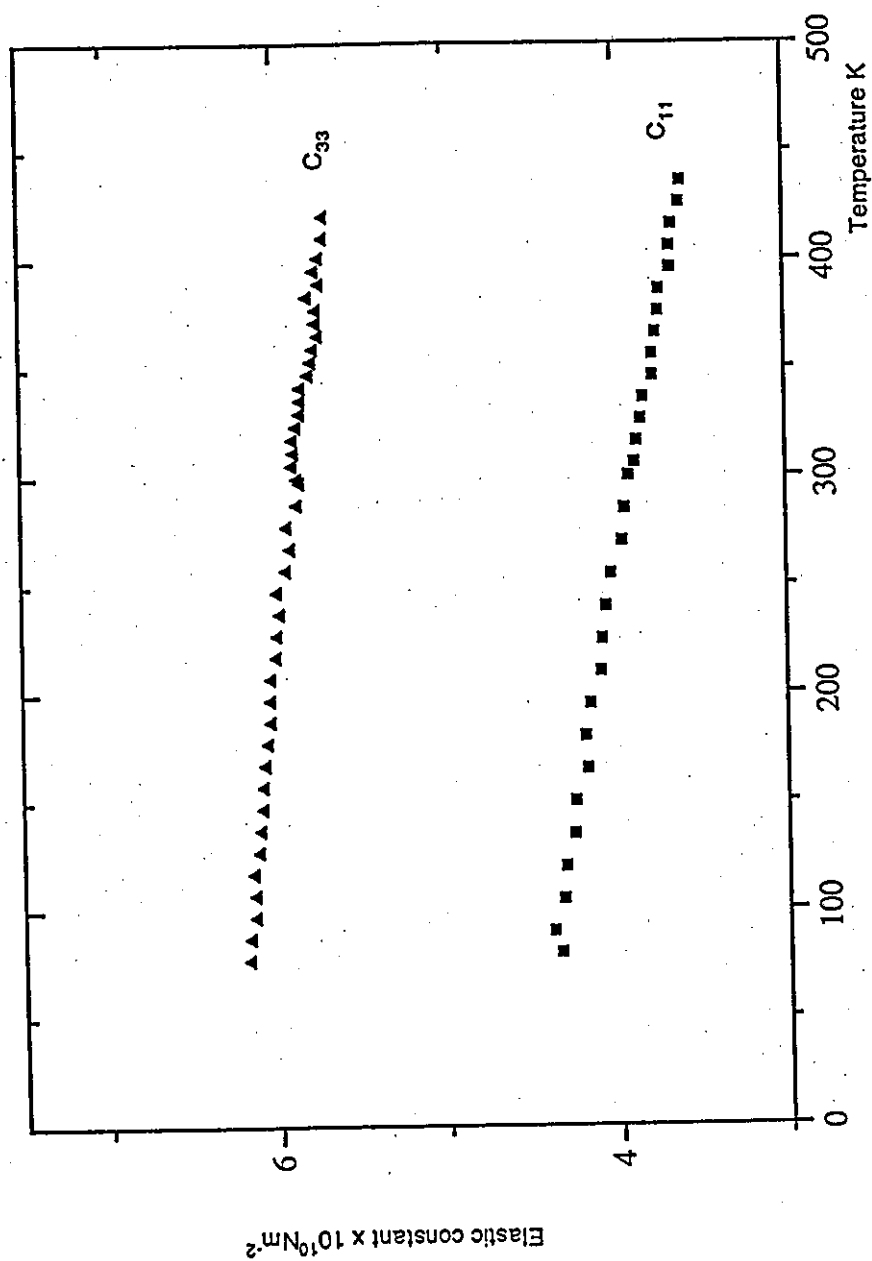


Fig. 3.27 Temperature dependence of elastic constant C_{11} and C_{33} for CsNiCl_3

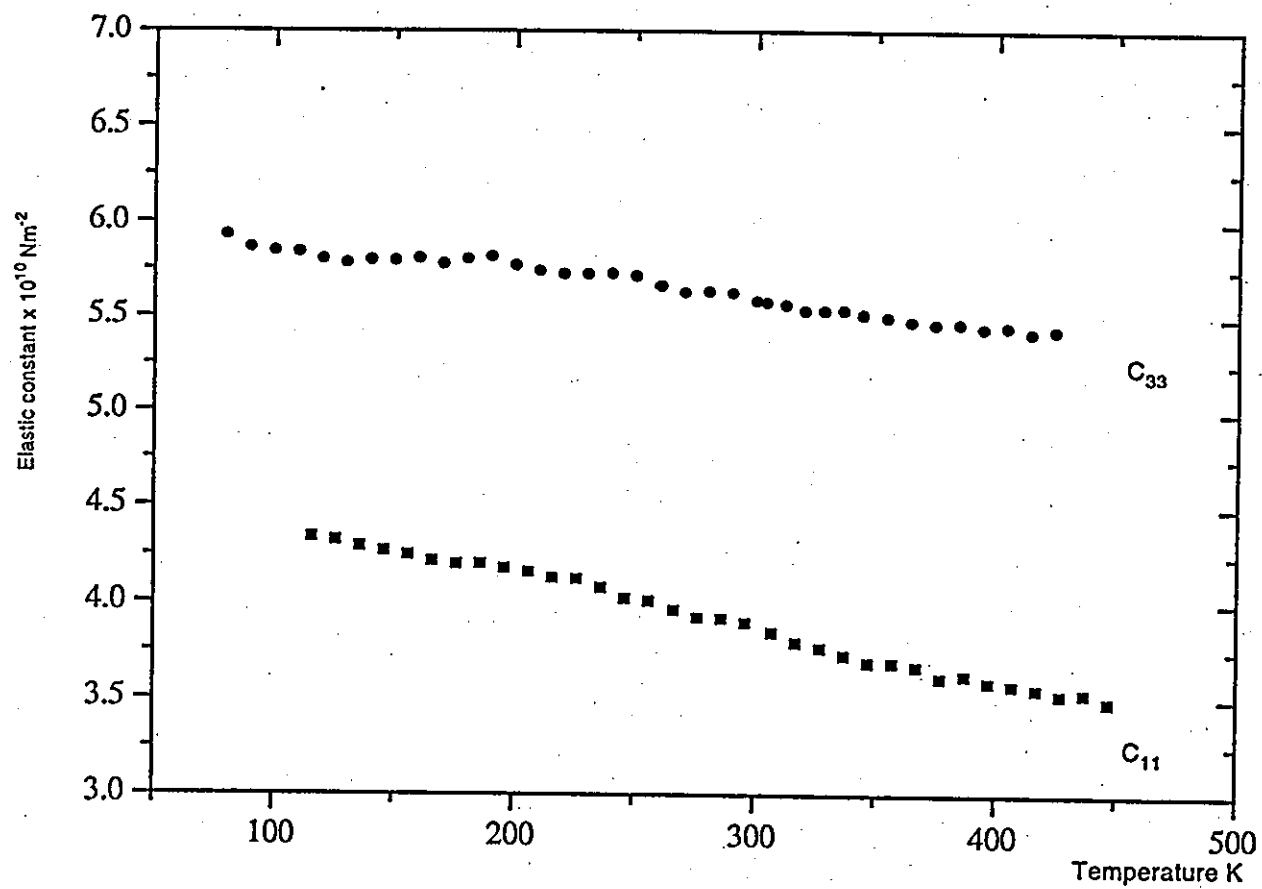


Fig. 3.28 Temperature dependence of elastic constant C_{11} and C_{33} for RbNiCl_3

Chapter 4

DSC

4.0 The Differential Scanning Calorimetry:

4.1 Introduction:

The specific heat of TMMC(H) in the range of 1.5-300K has been measured by Dunn [1983] who find a sharp anomaly at the phase transition. A preliminary DSC study on TMMC and TMMB showed there is a large change in the specific heat of both compounds at the phase transition [Visser 1985].

When a phase transition occurs, the change in heat content and in the thermal properties of the sample is indicated by a peak in its differential thermal analysis output. If the reaction proceeds at a rate varying with temperature, i.e., possesses an activation energy - the position of the peak varies with heating rate if other experimental conditions are maintained fixed [Kissinger 1957]. This provides a straightforward method to investigate the activation energies involved in the phase transitions.

In this work, investigations into the structural phase transitions of TMMC, TMMC:Cu, TMMB and deuterated TMMB (d_{12} -TMMB) are investigated using DSC and the activation energies at the phase transitions temperature are deduced. Experiments were carried out using a Mettler DSC 30 system over the temperature range 171K to 500K.

4.2 Measuring principle:

Figure. 4.1 shows a view of the measuring cell. The heat flow \dot{H} to the sample (\dot{H} in order to express that the heat flow is the change in sample enthalpy) is equal to the difference between the two heat flows \dot{Q}_s and \dot{Q}_r ,

$$\dot{H} = \dot{Q}_s - \dot{Q}_r \quad \dots\dots 4.1$$

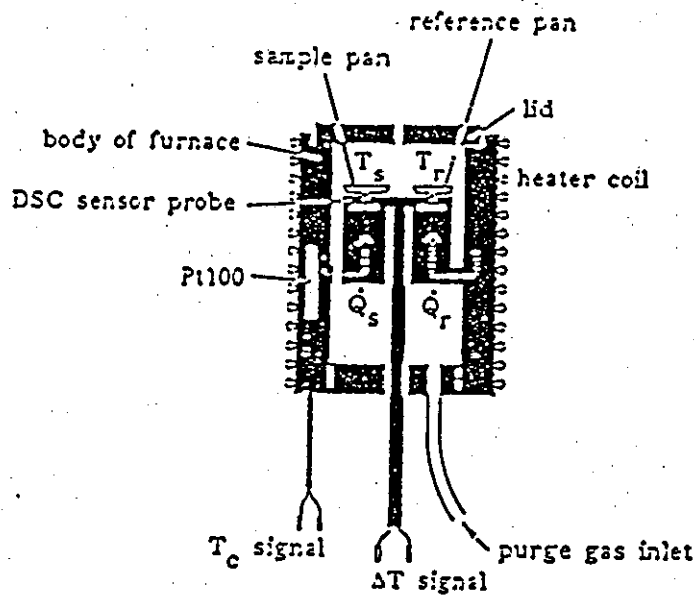


Fig. 4.1: Sectional view of the DSC measuring cell

From the thermal analogue of Ohm's law $\dot{Q} = \frac{T_2 - T_1}{R_{th}}$ i.e. the heat flow is proportional to the driving force (temperature difference $T_2 - T_1$) and inversely proportional to the thermal resistance R_{th} . When this is applied to the DSC cell it follows that

$$\dot{H} = \dot{Q}_s - \dot{Q}_r = \frac{T_c - T_s}{R_{th}} - \frac{T_c - T_r}{R_{th}} \quad \dots\dots 4.2$$

For reasons of symmetry, the two T_c and R_{th} values are identical. It follows that

$$\dot{H} = -\frac{T_s - T_r}{R_{th}} \quad \dots 4.3$$

In order to avoid problem with signs, an effect is defined as exothermic or endothermic and the sign is omitted. As the temperature difference, $\Delta T = T_s - T_r$ is measured by the sensor thermocouple, it follows from the thermocouple equation, $\Delta U = \Delta T \cdot S$

$$\dot{H} = \frac{\Delta U}{R_{th} \cdot S} \quad \dots 4.4$$

The two terms $R_{th} \cdot S$ are functions of the actual temperature, they can be combined as the calorimetric sensitivity $E = R_{th} \cdot S$ which can be divided into a temperature dependent (relative) term E_{rel} and a temperature independent term E_{in} , specific to the measuring cell being used. $E = E_{rel} \cdot E_{in}$. Thus it follows that the heat flow to the sample is

$$\dot{H} = \frac{\Delta U}{E_{in} \cdot E_{rel}} \quad \dots 4.5$$

The temperature dependence of E_{rel} is contained in the TA Processor as a hard programme polynomial $E = A + BT + CT^2$. The specific sensor parameters A, B and C are fixed with the coding plug in the measuring cell.

E_{in} was determined by calibrating the DSC using the known heat of fusion of indium with the DSC measuring cell set to 'medium' sensitivity using the standard sensor. An aluminium DSC pan with about 6 mg Indium, 4.5 mg lead and 3 mg zinc were heated in the DSC cell using the standard procedure for complete calibration (see Mettler handbook). An empty pan was used as a reference sample. Three endothermal melting peaks were displayed and A, B, C and E_{in} calculated and automatically transferred to the TC10A TA Processor. Temperatures subsequently did not require further correction although occasional checks were carried out.

The primary signal is converted once per second with equation 4.5 to the DSC signal H for the on-line plot on the printer plotter and for the analogue output.

No account is taken in the derivation of equation 4.5 for the fact that heat capacities as well as resistance are associated on the path of the heat flow. The original heat flow is calculated in all off-line evaluations, plotted on the printer/plotter and used for partial and total integrals. The sample temperature is also plotted after corrections.

4.3 Theory:

Based on the work of Willhelmy in 1850, the ratio of chemical reaction $\frac{d\alpha}{dt}$ can be expressed as a function of the degree of conversion α , using the kinetic equation

$$\frac{d\alpha}{dt} = k(1 - \alpha)^n \quad \text{..... 4.6}$$

where $\frac{d\alpha}{dt}$ = ratio of reaction s^{-1}

α = degree of conversion (which grows from 0 to 1 during the reaction)

n = order of reaction

k = rate coefficients

In calorimetric measurements, α is the ratio of enthalpies up to a given degree of conversion (ΔH) and total enthalpy of reaction (ΔH_T) i.e.

$$\alpha = \frac{\Delta H}{\Delta H_T} \quad \text{.....4.7}$$

which is equivalent to the ratio of areas under the dsc curve corresponding

to a given conversion.

In equation 4.6 the effect of temperature is introduced through the use of the Arrhenius equation derived in 1889.

$$k = Ae^{\frac{-E}{RT}} \quad \text{.....4.8}$$

where A = reaction rate constant at infinite temperature (pre-exponential factor s^{-1})

E = activation energy in Jmol^{-1}

R = gas constant = 8.31 J/mol K

T = temperature K

Taking logarithm $\ln k = \ln A - (E/R) \cdot 1/T$

This is a linear function of $\ln k$ versus $1/T$, the so called 'Arrhenius plot'.
See Figure 4.2.

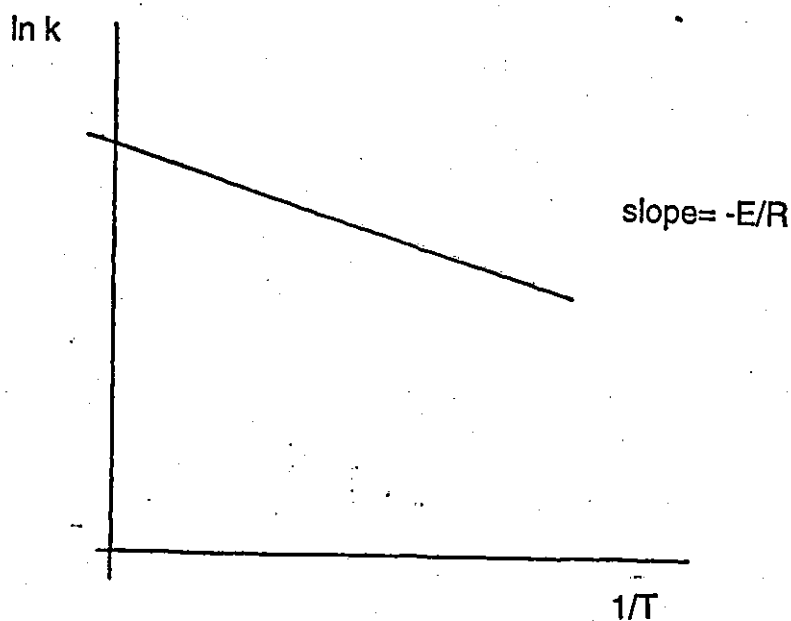


Fig. 4.2: The Arrhenius plot

Combining equation 4.6 and 4.8 the following expression is obtained

$$\frac{d\alpha}{dt} = Ae^{\frac{-E}{RT}}(1-\alpha)^n \quad \text{.....4.9}$$

At constant heating rate $\phi = dT/dt$, equation 4.9 can be written as

$$\frac{d\alpha}{dT} = \frac{A(1-\alpha)^n e^{\frac{-E}{RT}}}{\phi} \quad \text{.....4.10}$$

Determination of parameters A, E and n are based on the solution of equation 4.9 and 4.10.

Several approaches involved use the second derivative of equation 4.10 with respect to temperature [Sestak et. al. 1973] which gives

$$\frac{d^2\alpha}{dT^2} = \frac{d\alpha}{dT} \left[\frac{E}{RT^2} - \left(\frac{d\alpha}{dT} \right) \cdot \frac{n}{(1-\alpha)} \right] \quad \text{.....4.11}$$

and since this derivative must be zero and the inflection point of the maximum of a dsc peak

$$\frac{E}{RT_{\max}^2} = \left(\frac{d\alpha}{dT_{\max}} \right) \left(\frac{n}{1-\alpha_{\max}} \right) \quad \text{.....4.12}$$

where E can be calculated if n is known and T_{\max} , $\frac{d\alpha}{dT_{\max}}$ and α_{\max} are measured.

Combining equation 4.10 and 4.12 gives

$$\left(\frac{A}{\phi}\right) e^{\frac{-E}{RT_{\max}}} n(1-\alpha_{\max})^{n-1} = \frac{E}{RT_{\max}^2} \quad \text{.....4.13}$$

and since $(1-\alpha_{\max})$ is a constant for a given value of n , a plot $\ln \left[\frac{\phi}{T_{\max}^2} \right]$ against $1/T_{\max}$ for a series of runs at different heating rate ϕ gives E . The slope of such a plot is $-E/R$. This is the Kissinger method [Kissinger 1956].

Augis and Bennet [1978] modified the Kissinger treatment for use with the Avrami-Erofe'ev model that applies to many solid state reactions. They plot $\ln \left[\frac{\phi}{T_{\max} - T_o} \right]$ against $1/T_{\max}$ where T_o is the initial temperature at the start of the heating programme instead of $\ln \left[\frac{\phi}{T_{\max}^2} \right]$ against $1/T_{\max}$. Both the Kissinger and Augis & Bennet approaches were used to analyse the results obtained in this investigation.

4.4 DSC measurements:

The Mettler TA 300 system shown in Figure 4.3 was used to study the phase transition temperature of TMMC, TMMC:Cu, TMMB and d_{12} -TMMB crystals. The systems shown consist of a DSC 30 cell (cryofurnace covering temperature range -175C to 600 C), a liquid nitrogen reservoir, a microprocessor to control the furnace being used and performs the calculations as well as a printer for the output of results. Inert gas (argon) is used to purge gas and vapour products formed during analysis from the cell and the DSC cell is thus protected from corrosive gases. The purge gas also removes atmospheric oxygen in order to avoid unwanted oxidation of the sample.

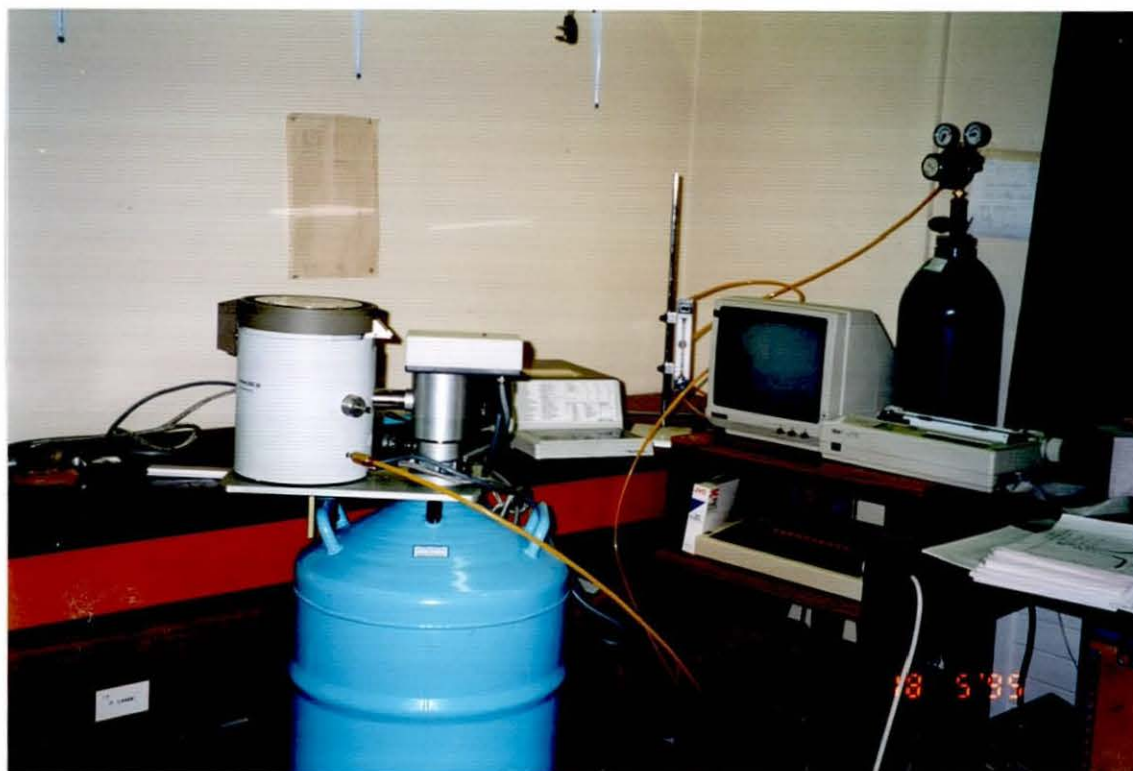


Fig. 4.3: The Mettler TA 300

Thermal events in the sample appear as deviations from the DSC baseline in either an endothermic or exothermic direction depending upon whether more or less energy has to be applied to the sample relative to the reference material. In DSC, endothermic responses are usually represented as being positive, i.e. above the baseline, corresponding to an increased transfer of heat to the sample compared to the reference.

Powdered samples of TMMC, TMMC:Cu, TMMB and d_{12} -TMMB were used for the DSC measurements. Aluminium pans were used for both the sample and the reference. The sample mass was about 12 mg, heating rates from 4 to 13 K/min with a temperature range of 171 K to 500K.

4.5 Results:

As shown in Figure 4.4, the scan reveals two distinct transitions for all four compounds. The low temperature transitions are of first order and another transition starts at about 373 K but being less well-defined presumably due to a second order transition.

The phase transition of these compounds with their enthalpy change ΔH are shown in Table 4.1. The enthalpy of the higher temperature transitions is too small for accurate peak transition determination due to the nature of its transition. Figure 4.5-4.8 shows the transitions with their thermal hysteresis upon cooling and heating the samples with their thermal hysteresis as indicated. The reproducibilities in the DSC curve, peak temperature and peak areas were good ($\pm 10\%$) in several thermal cycles.

Table 4.1 Transition temperature at heating rate 5K/min

Compound	T_{c1} K	Enthalpy (ΔH) Jg^{-1}	T_{c2} K
TMMC	127.2	4.6251	390.5
TMMC:Cu	129.3	1.1844	388.0
TMMB	144.9	4.5363	383.0
d_{12} -TMMB	143.6	4.8870	383.0

As observed, the enthalpy of TMMC:Cu is lower than the other three compounds. This effect might be due to the presence of Cu ions replacing the Mn ions. Interesting results have also been found due to doping in TMMC. An appreciable broadening of the ESR line and a shift in the transition temperature was observed [Richards 1974, Clements et. al. 1982, Levola & Laiho 1986, Braud et. al. 1990].

Heating these compounds at larger heating rates leads to an increase in the endothermal peak height and shifts the peak to higher temperatures as shown in Figure 4.9-4.10. The degree of conversion α at the transition peak was checked by integrating the data to the peak and was found to be the same for different heating rates. The fitting of the curve was done with

the Origin software package. The use of the Kissinger and Augis & Bennet methods requires α to be the same at each heating rate. This check shows that the method should be valid for these results.

Table 4.2-4.5 shows the peak temperature of the endotherm T_{\max} in degrees Kelvin with corresponding heating rate ϕ for TMMC, TMMC:Cu, TMMB and d_{12} -TMMB. All three methods (Avrami, Kissinger and Augis & Bennet) were employed to calculate the activation energy of the phase transition. $\ln \phi$ Vs $1/T_{\max}$, $\ln\left(\frac{\phi}{T_{\max}^2}\right)$ Vs $1/T_{\max}$ and $\ln\left(\frac{\phi}{T_o - T_{\max}}\right)$ Vs $1/T_{\max}$ have been calculated and shown in Table 4.2-4.5. Figure 4.11-4.14 show that the points obtained lie on reasonable straight line when these parameters were plotted. The plots were fitted using the Origin software package. This software fits the best straight line to the points and prints out the equation for this line, enabling activation energy E to be calculated.

Since the activation energy deduced from all three methods are very similar, clearly the results are not sensitive to the exact analysis method and the average values from all three methods are taken as the true values. The calculated values for activation energy E are given in Table 4.6.

Table 4.6 Activation energy to TMMC, TMMC:Cu, TMMB and d_{12} -TMMB

Compound	ACTIVATION ENERGY kJ/mol			
	Avrami	Kissinger	Augis & Bennet	Average
TMMC	73.068	70.940	67.828	70.612
TMMC:Cu	51.600	49.430	46.641	49.224
TMMB	53.896	51.465	49.881	51.747
d_{12} -TMMB	72.069	69.665	67.992	69.909

So far, there is no reported value of activation energy for TMMC, TMMC:Cu, TMMB and d_{12} -TMMB. Laiho et. al. [1973] reported the activation energy of CsCuCl_3 as 1 eV below the transition point and 0.78 eV above the transition point. The activation energy of TMMC:Cu shows

a marked difference compared to TMMC and this is again due to the presence of Cu. As for d₁₂-TMMB and TMMB, there is a very marked difference in the enthalpy and the activation energy obtained. The origin is believed to lie in two different effects which will be discussed in the final chapter.

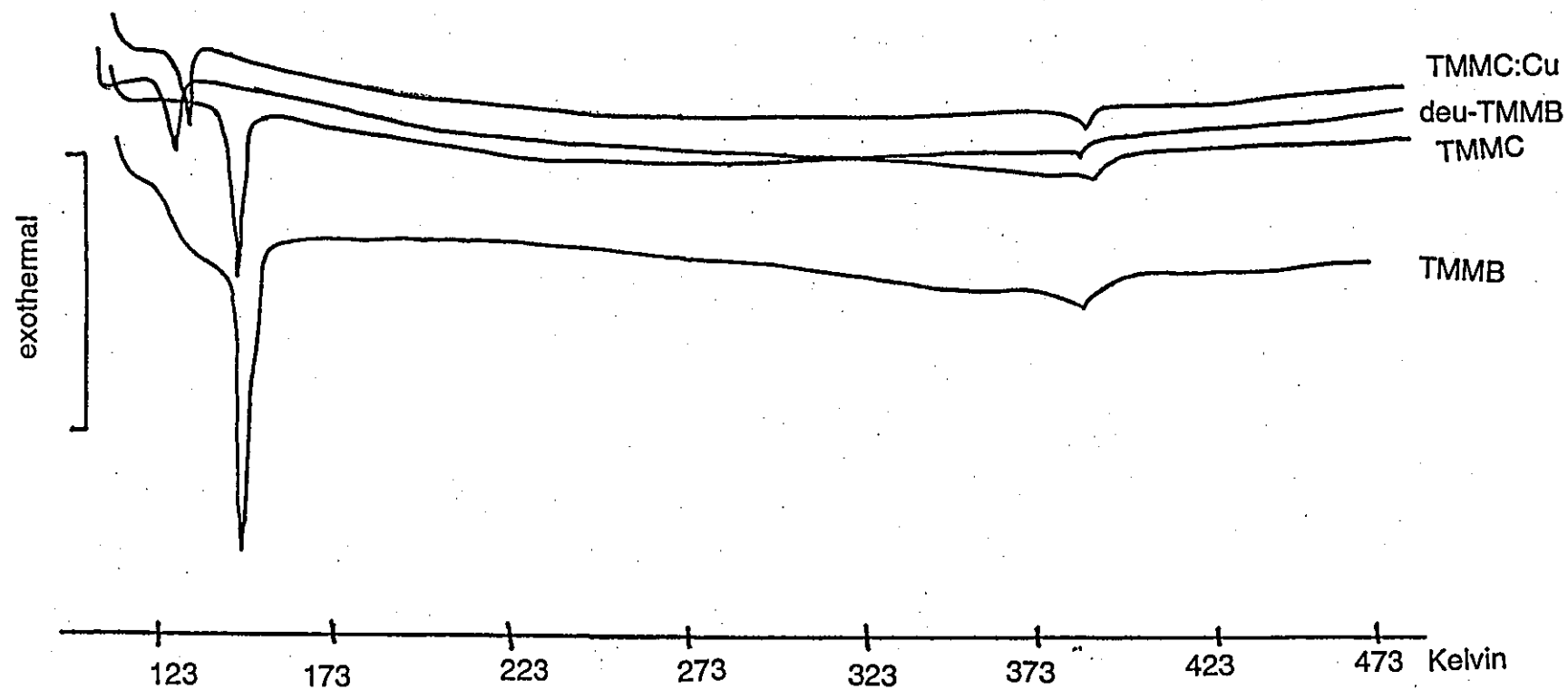


Fig. 4.4: DSC 30 data tracings for TMMC, TMMC:Cu, TMMB and deuterated TMMB.

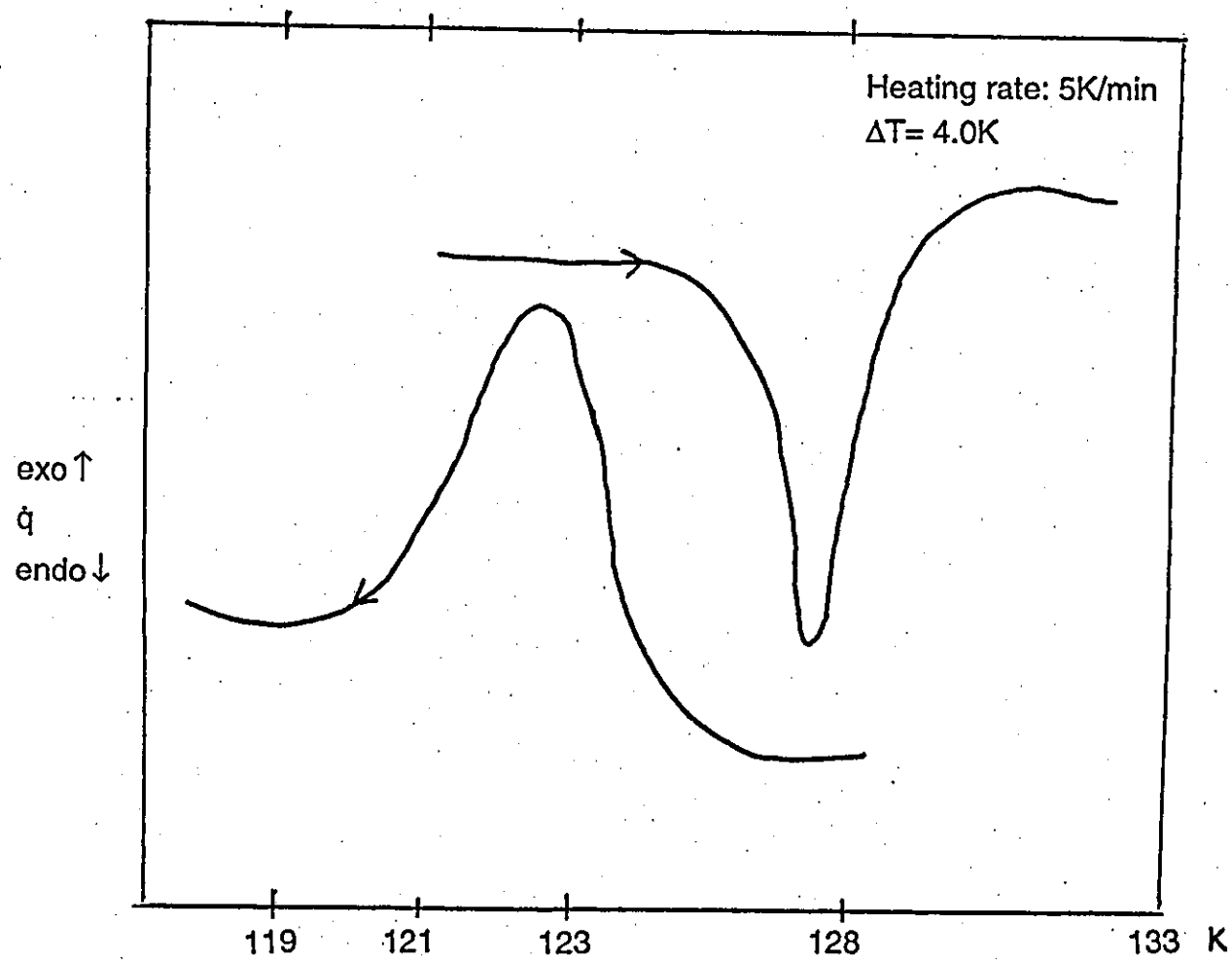


Fig. 4.5 DSC curve of TMMC. Heating and cooling curves are shown

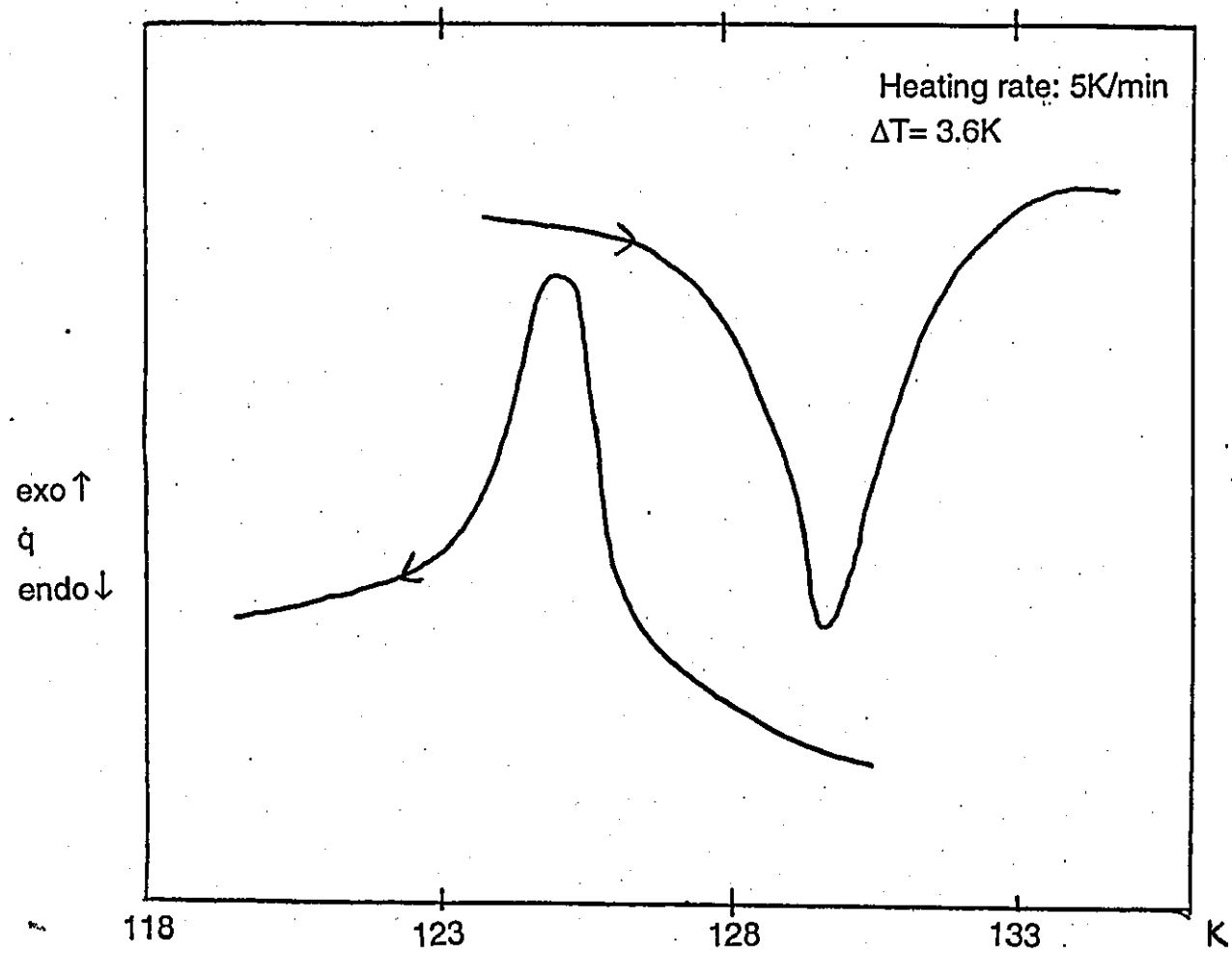


Fig. 4.6 DSC curve of TMMC:Cu. Heating and cooling curves are shown

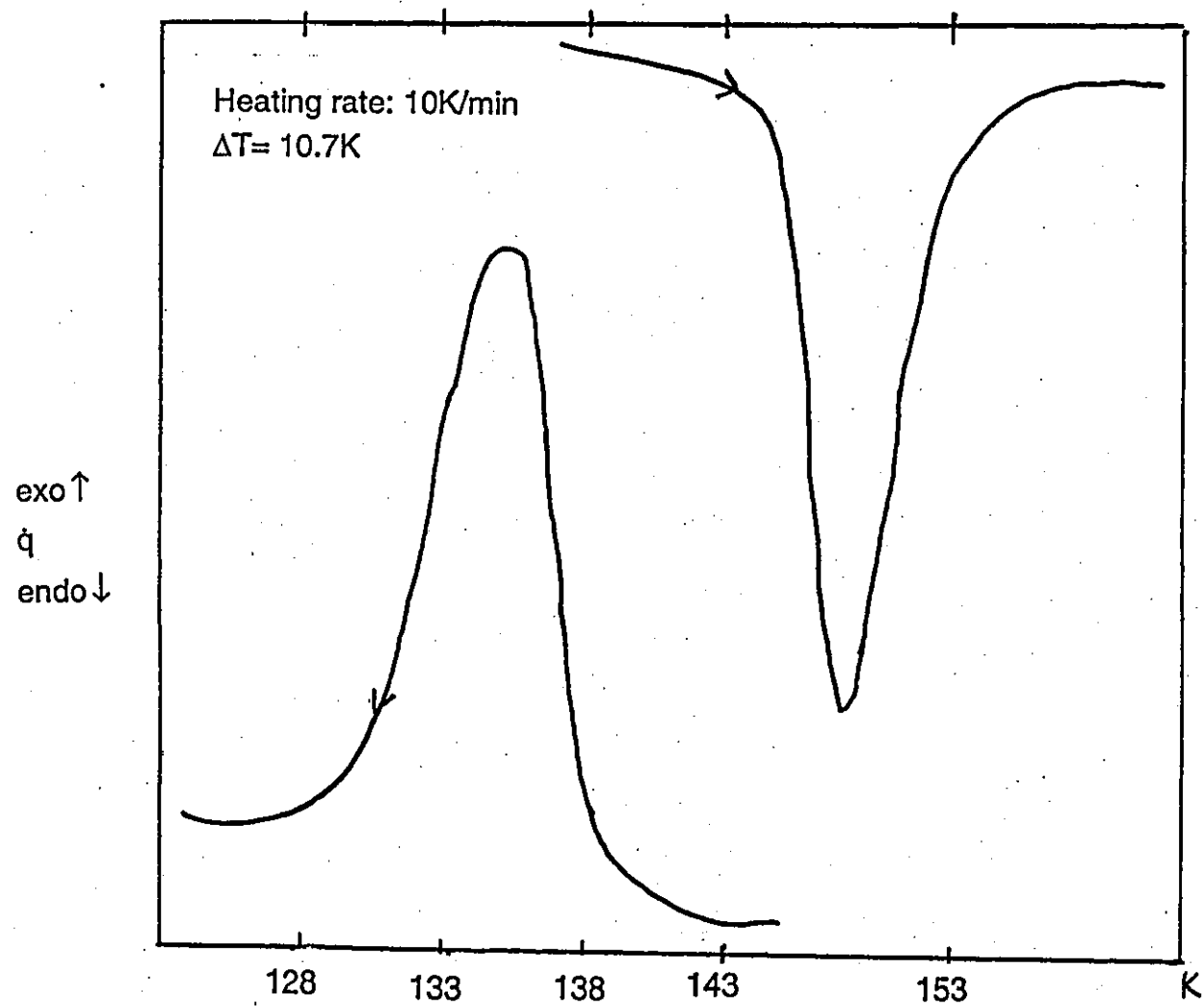


Fig. 4.7 DSC curve of TMMB. Heating and cooling curves are shown

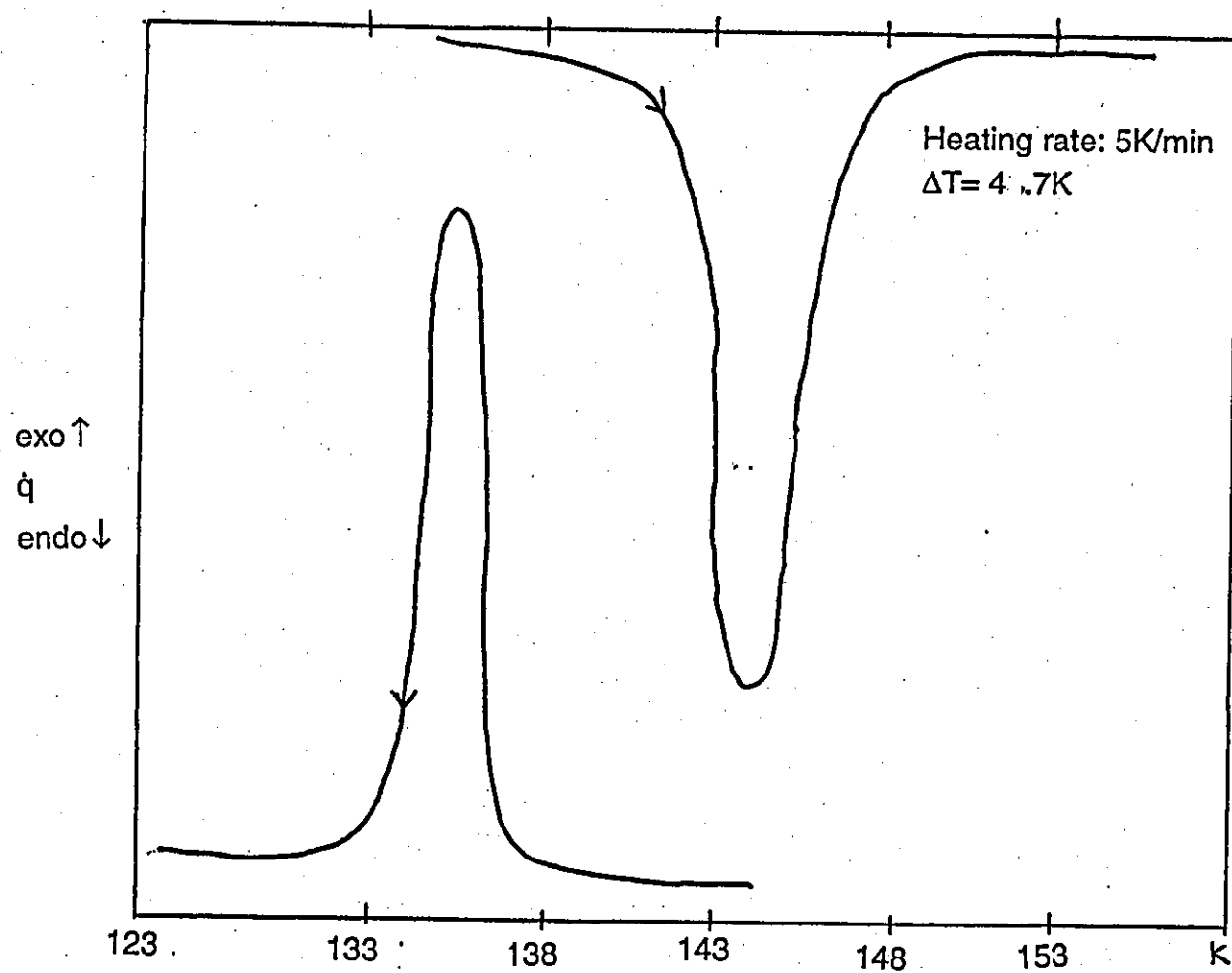


Fig. 4.8: DSC curve of d_{12} -TMMB. Heating and cooling curves are shown

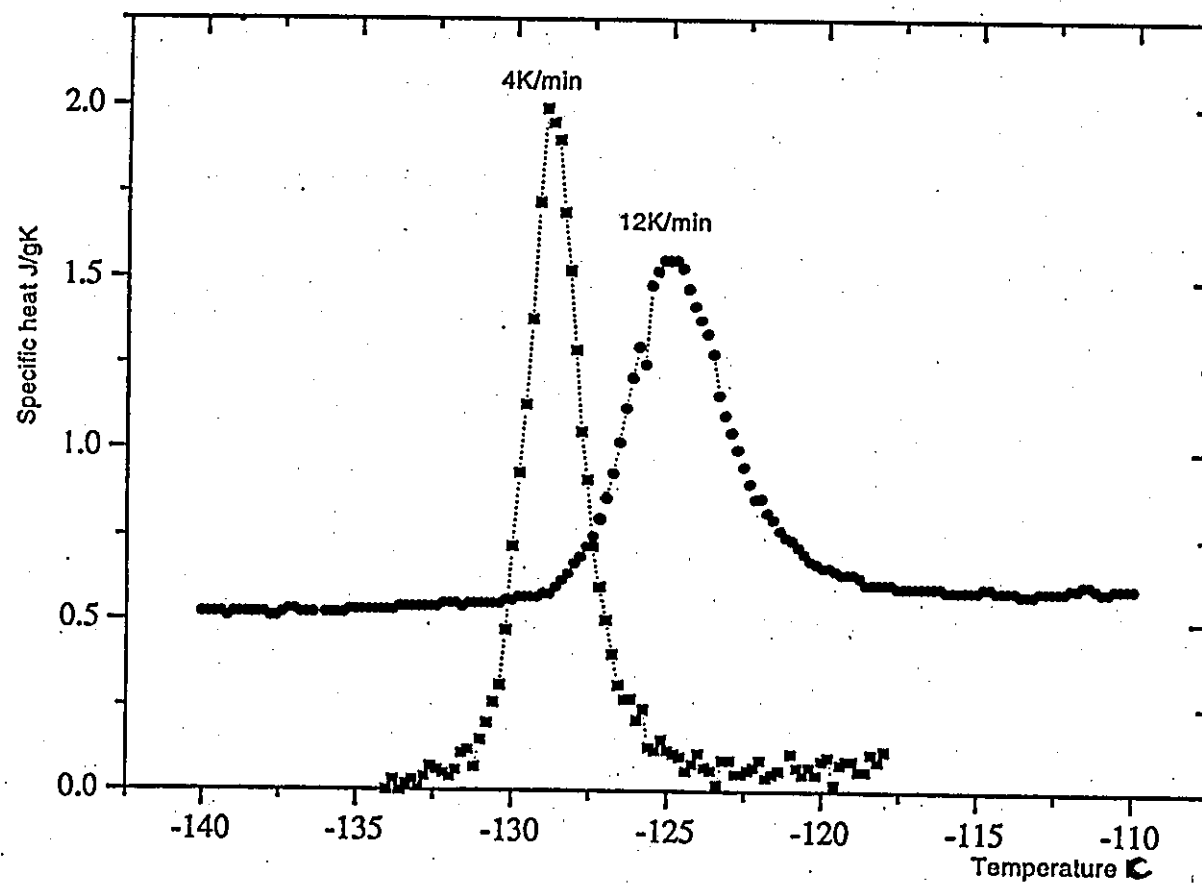


Fig. 4.9: DSC measurement curves of TMMB samples heated with different heating rates (as indicated)

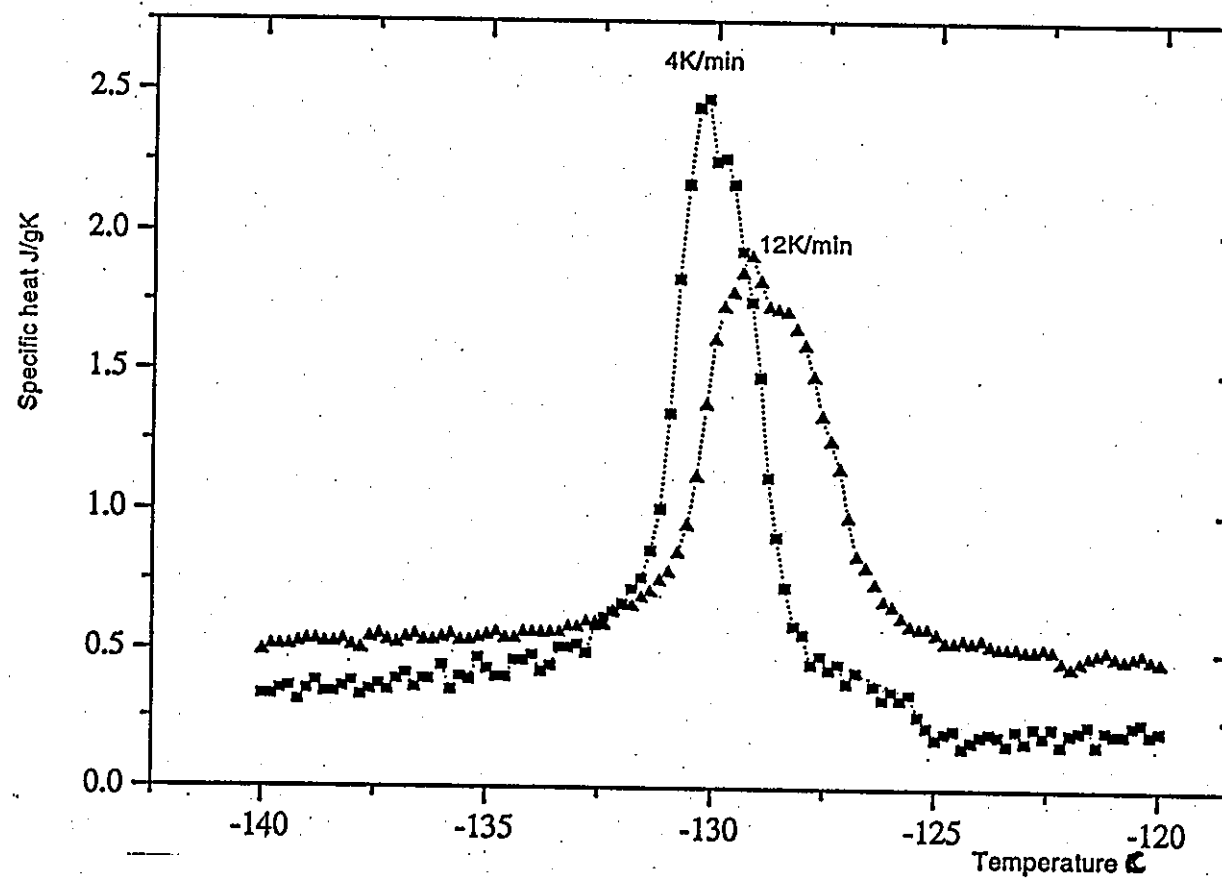


Fig. 4.10: DSC measurement curves of deuterated-TMMB samples heated with different heating rates (as indicated)

Table 4.2 Data and results obtained from DSC measurements for TMMC

Rate ϕ K/min	$\ln \phi$	T_{c1} K	ΔH J/g	$1/T_{c1} \times 10^{-3}$	$\ln \frac{\phi}{T_{c1}^2}$	$\ln \frac{\phi}{T_{c1} - T_o}$	T_{c2} K
13	2.565	129.0	5.4665	7.75	-7.155	-0.731	386.8
12	2.485	128.8	5.3833	7.76	-7.232	-0.804	385.0
11	2.398	128.6	5.5228	7.78	-7.316	-0.883	383.4
10	2.303	128.3	4.3306	7.79	-7.406	-0.967	379.0
9	2.197	128.1	4.6595	7.81	-7.508	-1.065	384.0
8	2.079	127.8	4.9757	7.82	-7.621	-1.171	384.0
7	1.946	127.5	5.4949	7.84	-7.750	-1.293	384.0
6	1.792	127.3	5.0858	7.86	-7.901	-1.439	384.0
5	1.609	127.2	4.6251	7.86	-8.082	-1.617	379.0
4	1.386	127.0	4.4677	7.87	-8.302	-1.833	383.0

Table 4.3 Data and results obtained from DSC measurements for TMMC:Cu

Rate ϕ K/min	$\ln \phi$	T_{c1} K	ΔH J/g	$1/T_{c1} \times 10^{-3}$	$\ln \frac{\phi}{T_{c1}^2}$	$\ln \frac{\phi}{T_{c1} - T_o}$	T_{c2} K
13	2.565	132.3	1.7182	7.56	-7.205	-0.846	386.8
12	2.485	131.4	2.1835	7.61	-7.272	-0.896	385.0
11	2.398	130.8	2.0578	7.65	-7.349	-0.962	383.4
10	2.303	130.6	1.6327	7.66	-7.442	-1.051	379.0
9	2.197	130.4	1.4435	7.67	-7.544	-1.149	384.0
8	2.079	130.3	1.3704	7.67	-7.660	-1.263	384.0
7	1.946	129.8	1.6641	7.70	-7.786	-1.379	384.0
6	1.792	129.4	1.5679	7.73	-7.934	-1.519	383.0
5	1.609	129.3	1.1844	7.73	-8.115	-1.697	383.0
4	1.386	129.1	1.7662	7.75	-8.335	-1.913	383.0

Table 4.4 Data and results obtained from DSC measurements for TMMB

Rate ϕ K/min	$\ln \phi$	T_{c1} K	ΔH J/g	$1/T_{c1} \times 10^{-3}$	$\ln \frac{\phi}{T_{c1}^2}$	$\ln \frac{\phi}{T_{c1} - T_o}$	T_{c2} K
13	2.565	148.2	4.3065	6.75	-7.432	-1.268	386.8
12	2.485	147.7	4.2265	6.77	-7.505	-1.337	386.8
11	2.398	147.1	4.5236	6.80	-7.584	-1.411	386.8
10	2.303	147.0	4.5206	6.80	-7.678	-1.504	386.8
9	2.197	146.4	4.5598	6.83	-7.775	-1.596	386.8
8	2.079	145.7	4.5455	6.86	-7.884	-1.698	386.8
7	1.946	145.7	4.9768	6.86	-8.017	-1.831	386.8
6	1.792	145.1	4.4911	6.89	-8.163	-1.972	385.5
5	1.609	144.9	4.5363	6.90	-8.343	-2.149	383.0
4	1.386	144.5	4.8844	6.92	-8.560	-2.363	384.3

Table 4.5 Data and results obtained from DSC measurements for d_{12} -TMMB

Rate ϕ K/min	$\ln \phi$	T_{c1} K	ΔH J/g	$1/T_{c1} \times 10^{-3}$	$\ln \frac{\phi}{T_{c1}^2}$	$\ln \frac{\phi}{T_{c1} - T_o}$	T_{c12} K
13	2.565	145.7	5.4655	6.86	-7.398	-1.212	386.8
12	2.485	146.0	5.3833	6.85	-7.482	-1.299	385.0
11	2.398	145.4	5.5228	6.88	-7.561	-1.373	383.4
10	2.303	145.3	4.3306	6.88	-7.655	-1.466	379.0
9	2.197	144.8	4.6595	6.91	-7.753	-1.559	384.0
8	2.079	144.5	4.9758	6.92	-7.867	-1.670	384.0
7	1.946	144.2	5.4949	6.93	-7.996	-1.797	384.0
6	1.792	143.9	5.0858	6.95	-8.146	-1.944	383.0
5	1.609	143.6	4.6251	6.96	-8.325	-2.119	383.0
4	1.386	143.3	5.9894	6.98	-8.544	-2.335	383.0

CHAPTER 5

Neutron scattering

5.1 Introduction:

With the advent of nuclear reactors, thermal neutrons have become a valuable tool for investigating many important features of matter, particularly condensed matter. The usefulness of neutron scattering as a technique to study dynamic properties of condensed matter stems from the fact that neutrons interact with both nuclei and magnetic, or unpaired electrons, and that slow neutrons have energies and wavelengths that match those of excitations and collective modes, e.g. rotational energy levels in molecules and acoustic and optic phonons.

Phonons play an important role in all phases of solid state physics. Phenomena such as resistivity, thermal conductivity, heat capacity and superconductivity for example are related directly to the phonon density of states. Other properties such as the dielectric function, ultrasonic, the inter atomic potentials (through the force constant) are more intimately related to the normal modes of vibrations (phonons) of crystals. These in turn are, of course ultimately related to the electronic structure of the crystal.

Neutron scattering allows one to perform a frequency analysis of atomic motions, and the determination of phonon dispersion relations has now become almost routine. CsFeBr₃ crystal of one of the ABX₃ compounds is to be studied with neutron scattering technique, which will enable us to get the phonon dispersion curve. From the initial slope of the dispersion curve we will be able to deduce the sound velocity in the crystals and hence calculate the elastic constant.

5.2 Neutron scattering theory:

The neutron is a fundamental particle of mass $m = 1.675 \times 10^{-27}$ kg, and this results in the de Broglie wavelength of thermal neutrons being of the order of inter atomic distances in solids and liquids. Thus, interference effects occur which yield information on the structure of the scattering system.

Since the neutron has zero electrical charge (uncharged), it means that not only can it penetrate deeply into the target, but also that it comes close to the nuclei - there is no Coulomb barrier to be overcome, so neutrons are thus scattered by nuclear forces, and for certain nuclides the scattering is large.

The energy of thermal neutrons is of the same order as that of many excitations in condensed matter. So, when the neutrons are inelastically scattered by the creation or annihilation of an excitation, the change in energy of the neutron is a large fraction of its initial energy. So measurements of the neutron energies thus provides accurate information on the energies of the excitations, and hence on the inter atomic forces.

The neutron has a magnetic moment (1.913 nuclear magnetons) and a spin 1/2, which means that neutrons interact with the unpaired electrons in magnetic atoms. Elastic scattering from this interaction gives information on the arrangement of electron spins and the density distribution of unpaired electrons. Inelastic magnetic scattering gives the energies of magnetic excitations and in general permits a study of time dependent spin correlations in the scattering system.

At present, the source of thermal neutrons in most scattering experiments is a nuclear reactor. In the thermal region, the velocity spectrum of the neutrons emerging from the reactor is close to a Maxwellian, with the temperature T being that of the moderator. The Maxwellian distribution for flux is:

$$\phi(v) \propto v^3 \exp\left[-\frac{mv^2}{2k_B T}\right] \quad \text{.....5.1}$$

where $\phi(v)dv$ is the number of neutrons passing through unit area per second with velocities between v and $v + dv$, m is the mass of the neutron, and k_B is the Boltzman constant. The maximum of the function occurs at

$$v = \left[\frac{3k_B T}{m} \right]^{1/2} \quad \text{.....5.2}$$

The peak in the Maxwellian spectrum can be shifted to higher energies by allowing the neutrons in the reactor to pass through a heated source e.g. a graphite block. Low energy neutrons are obtained by passing the neutrons through liquid deuterium. In this way a range of energies can be obtained, e.g. $E \sim 0.1 - 10$ meV (cold) and $E \sim 10 - 100$ meV (thermal). For energies greater than 500 meV, the neutrons are classified as epithermal.

In actual scattering experiments, the key variables are the change in the neutron energy and the associated change in the wave vector. If the direction of propagation of the incident neutron beam travelling with velocity v_0 is represented by the vector \vec{k}_0 and that of the scattered neutron beam with velocity v by \vec{k}' , where the scattered beam make an angle 2θ with the incident beam, then from Figure 5.1

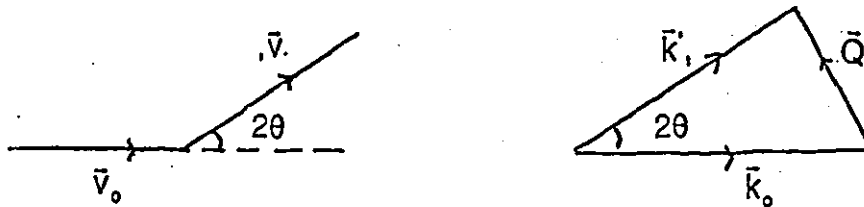


Fig. 5.1: Definition of the neutron scattering vector.

The magnitude of the scattering vector Q which has dimensions of reciprocal length is given by

$$Q^2 = k_o^2 + k'^2 - 2\bar{k}_o\bar{k}' \cos 2\theta \quad \text{.....5.3}$$

If we consider Q as a momentum transfer vector so that

$$\hbar Q = (m\bar{v} - m\bar{v}_o) \quad \text{.....5.4}$$

and the energy change on scattering

$$\hbar\omega = \left(\frac{m\bar{v} - m\bar{v}_o}{2} \right) \quad \text{....5.5}$$

where $\omega = 2\pi\nu$ is the angular frequency.

Alternatively, if E is the initial energy of the beam, and E' the final energy, then

$$\Delta E = E' - E = \frac{\hbar^2}{2m} [\bar{k}'^2 - \bar{k}_o^2] \quad \text{.....5.6}$$

In elastic scattering $\Delta E = 0$ and $|\bar{k}_o| = |\bar{k}'|$ since k' changes in direction but not in magnitude. The magnitude of Q then becomes

$$Q = |\bar{Q}| = 2k_o \sin\theta = \frac{4\pi}{\lambda} \sin\theta \quad \text{.....5.7}$$

In inelastic scattering, there is a finite energy change. The magnitude of wavelength and velocity are such that changes in energy and momentum resulting from interaction of the neutron with vibrational and rotational

modes of motion in atoms and molecules can be accurately measured. Hence by examining the energy distribution of the inelastically scattered neutrons, a great deal of information can be obtained about the motions of various kinds which occur in materials.

5.3 Neutron cross-section:

Consider a beam of thermal neutrons, all with the same energy E , incident on a target (Figure 5.2). The incident neutron has the state ψ_k and the scattered neutron the state $\psi_{k'}$. The direction of propagation of the latter with respect to the incident neutron is defined by the polar angle θ and the azimuthal angle ϕ .

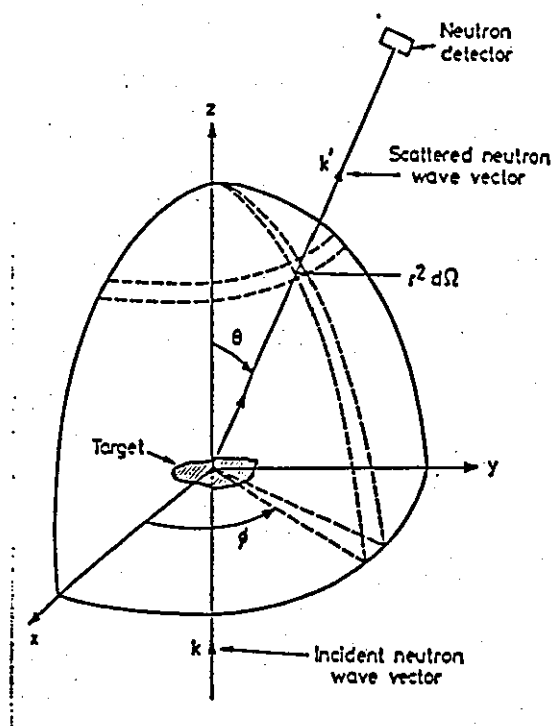


Fig. 5.2 Geometry of scattering experiments

The interaction of a monochromatic beam of neutrons (a neutron beam in which all the neutrons have the same wavelength or energy) incident upon a target (a collection of atoms) may be defined in terms of three cross-sections. These are:

First, the total scattering cross-section defined by:

$$\sigma = (\text{total number of neutrons scattered/unit time})/\Phi$$

where Φ is the flux of the incident neutrons (number of neutrons/cm²/sec).

Secondly, the differential cross-section

$$\frac{d\sigma}{d\Omega} = (\text{number of neutrons scattered/unit time/unit solid angle})/\Phi$$

For inelastic scattering, i.e. when the energy of the scattered neutron differs from that of the incident neutron, the state of the target must change. The initial and final states of the target is denoted as $|\lambda\rangle$ and $|\lambda'\rangle$ respectively, with corresponding energies E_λ and $E_{\lambda'}$. The cross section is then:

$$\left(\frac{d\sigma}{d\Omega}\right)_{k,\lambda \rightarrow k',\lambda'} = \frac{k'}{k} \left[\frac{m}{2\pi\hbar} \right]^2 |\langle \vec{k}', \lambda | \bar{V} | \vec{k}, \lambda \rangle|^2 \quad \text{.....5.9}$$

where V is the interaction potential that causes the transition and with the condition of conservation of energy

$$\frac{\hbar^2 k^2}{2m} + E_\lambda = \frac{\hbar^2 k'^2}{2m} + E_{\lambda'} \quad \text{.....5.10}$$

Finally, the partial differential cross-section:

$$\frac{d^2\sigma}{d\Omega d\omega} = (\text{number of neutrons scattered /unit time/unit solid angle with energies between } \omega \text{ and } \omega - d\omega) / \Phi d\omega$$

5.4 Scattering by phonons:

Neutron scattering affords a technique for the measurement of phonon dispersion curves in crystals. For crystals with simple, symmetric structure (one or two atoms per unit cell) it is often possible to measure polarisation vectors, and changes in the one-phonon line shape due to variations in temperature or pressure for example. Crystals with low symmetry and several atoms per unit cell are much more difficult to study thoroughly.

Structural phase transitions are usually heralded by an anomalous temperature dependence of certain phonon groups. Neutron scattering experiments have provided key information on the microscopic origin of various first order and continuous structural phase transitions.

For single phonon scattering, the scattering function $S(Q, \omega)$ with a scattering vector Q at frequency ω is given by

$$S(\vec{Q}, \omega) = \sum_v \frac{\hbar}{2\omega_v(\vec{k})} |F_v(\vec{Q})|^2 \left\{ [1 + n(\omega_v(\vec{k}))] \delta(\omega + \omega_v(\vec{k})) + n(\omega - \omega_v(\vec{k})) \right\}$$

....5.13

where $\omega_v(\vec{k})$ is the phonon frequency at wave vector \vec{k} , $n(\omega_v(\vec{k}))$ is the Bose-Einstein factor. $F_v(\vec{Q})$ is the structure factor for the v th normal mode,

$$F_v(\vec{Q}) = \sum_{\mu} \frac{b_{\mu}}{m_{\mu}} \exp(-W_{\mu}) \exp(i\vec{Q} \cdot \vec{R}_{\mu}) \vec{Q} \cdot \vec{e}(\mu, \vec{k}, v) \quad \text{..... 5.14}$$

where b_{μ} is the scattering length, m_{μ} is the mass, W_{μ} the Debye-Waller factor, and R_{μ} the position of the μ th nucleus, and \vec{e} is the mode eigenvector.

The delta functions in equation 5.13 are responsible for $S(Q, \omega)$ only having non-zero values at $\omega = \pm\omega(k)$. At low temperatures there are very few phonons with $\omega_v > 0$ and hence there is always a greater probability of

scattering for neutron energy loss ($\omega > 0$), corresponding to the creation of a phonon in the crystal rather than for energy gain where a phonon is absorbed. At high temperatures, the scattering factor tends to be the limiting value

$$S(\vec{Q}, \omega) \propto \frac{k_B T}{\omega_v^2(\vec{k})} \quad \text{.....5.15}$$

This is why high frequency modes tend to be difficult to observe with neutron scattering.

One other important point from Eq. 5.13 is that it contains the vector product $|\vec{Q} \cdot \vec{e}|^2$. The scattered intensity is strongest, therefore if \vec{Q} is parallel to \vec{e} , essentially the direction of atomic motion, and weakest if perpendicular. Using the $|\vec{Q} \cdot \vec{e}|^2$ factor it is possible to interpret the spectra and assign wave vectors and eigenvectors to the observed peaks. It is possible, therefore, with sufficient constant- \vec{Q} scans across the Brillouin zone, to build up a picture of the main dispersion relations of phonon branches in the crystal.

5.5 The triple axis spectrometer:

The availability of high flux reactors ($10^{14} - 10^{15} \text{ n/cm}^2$) has permitted neutron inelastic scattering studies of crystals of greater complexity and smaller size (the latter often a determining factor in adequately measuring the phonon and magnon spectra). In inelastic neutron spectroscopy, the energy E of the neutron before being scattered and E' after scattering have to be determined. There are essentially two methods:

- (i) the time of flight technique which determines the energy by determining the neutron velocity v
- (ii) the triple axis spectrometer (triple axis means one monochromator axis, one sample axis and one analyser axis, in contrast to two axis instruments where the analyser is missing). In this technique the

wavelength of the incident and scattered beams are determined using Bragg law.

For phonon studies experience has amply demonstrated the superiority of the triple axis spectrometer, which employs Bragg reflection, over time of flight instruments.

The advantage of a triple axis spectrometer over a two axis diffractometer is that in addition to measuring the neutron intensity as a function of momentum transfer Q , the use of the third axis enables the neutron intensity to be measured as a function of energy $\hbar\omega$ i.e. the inelasticity in the scattering.

The condition for conservation of crystal momentum and energy for the one-phonon coherent scattering process in single crystal requires that

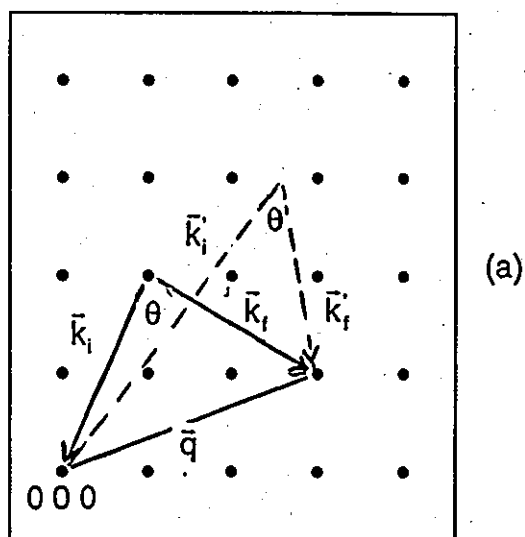
$$\vec{Q} = \vec{k} - \vec{k}' = \vec{\tau} - \vec{q} \quad \text{.....5.16}$$

and the momentum transfer is defined by:

$$\hbar\omega(\vec{q}) = \frac{\hbar^2(k^2 - k'^2)}{2m} \quad \text{.....5.17}$$

where k and k' are the incidents and final wave vectors and E and E' are the corresponding energies of the neutron. From equation 5.17 the Bragg condition is obtained when $|k| = |k'|$ and the scattering vector $Q = \vec{\tau}$, a reciprocal lattice vector. In conventional triple axis spectroscopy, two types of scan are used; the first is a constant q scan, in which the wave vector q is fixed and the energy transfer varied, and the second is a constant scan, in which the energy transfer and the direction of q is fixed but the magnitude of q is varied. These two scans are diagrammatically represented in Figure 5.3. The choice of scan depends on the resolution in energy and momentum of the spectrometer and the nature of the scattering surface studied.

Constant q scan



Constant ω scan

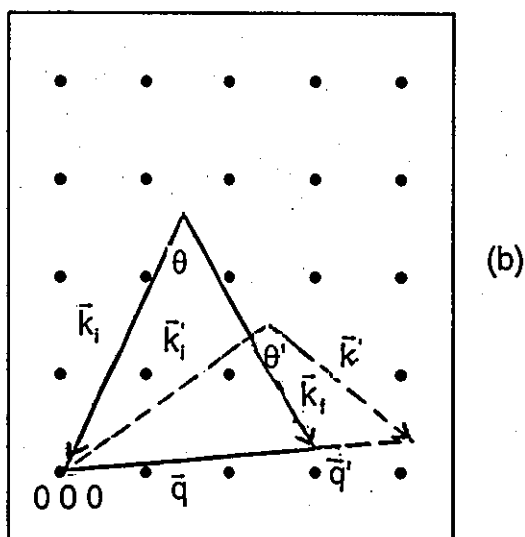


Fig. 3.5a: Schematic representation of a constant q scan in reciprocal space, in which the neutrons initial and final wavevectors change from k_i and k_f to k'_i and k'_f respectively

b: schematic representation of a constant energy scan in reciprocal space

In any measurement performed on a triple axis spectrometer, whether constant q or constant ω , the conservation rules (equation 5.16 and 5.17) must be satisfied simultaneously. The incident wavelengths are within the range 1.2 - 2.0 Å for thermal neutrons. The energy of these neutrons can be calculated using the de Broglie relation:

$$\lambda = \frac{2\pi}{k} = \frac{2\pi\hbar}{mv} \quad \text{.....5.18}$$

where v is the neutron velocity and M its mass. This then become:

$$\lambda = \frac{0.286}{E^{1/2}} \quad \text{....5.19}$$

where E is the neutron energy in eV and the wavelength is in Å.

5.6 The E7 Triple axis spectrometer at HMI-Berlin:

A triple axis E7 instrument in HMI-Berlin was used for the study of phonons in CsFeBr_3 . Figure 5.4 shows the schematic diagram of the instrument set-up. The massive ω -table of the diffractometer and its analyser-detector unit are mounted on a platform which rests on two concentric rails. By rotating the platform around the monochromator axis about $2\Delta\theta_m$ and the monochromator crystal about $\Delta\theta_m$, the wavelength of the neutron beam can be changed continuously. The vertically focusing monochromator crystal, PG(002) and Ge(311) can be exchanged remotely.

The detector arm or analyser detector support is driven by a friction wheel which moves on the platform. The detector is He-counter of cylindrical shape with an internal diameter of 48 mm and an active length of 100 mm. The He pressure is 3 bar. The efficiency of the detector is 90% for a neutron of wavelength 1Å and 99% for 2Å. Soller collimators can be mounted and easily changed between monochromator and sample (MS) between sample and analyser (SA) and between analyser and detector (AD). The in-pile collimation (RM) can be changed from open 40' and 20' by remote control. The instrument data are as follows:

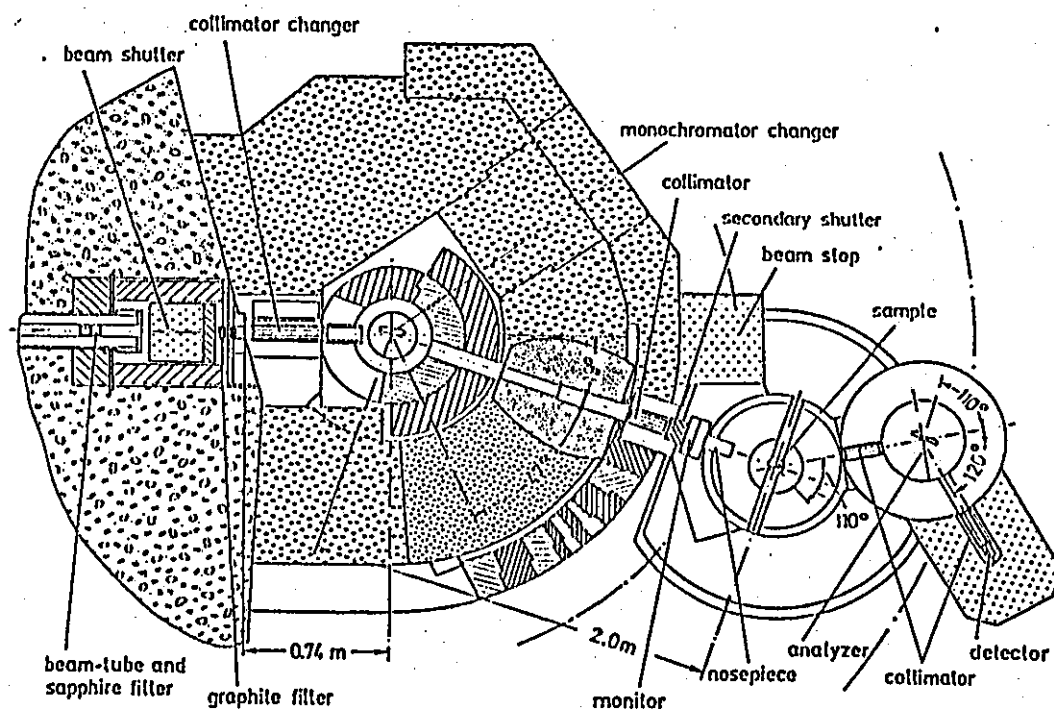


Fig. 5.4 The E7 3-axis spectrometer at HMI-Berlin

E7

INSTRUMENT DATA

Beam tube:	D1S
Monochromator crystals:	PG (002) (vert. focusing) Ge (311)
Expected flux at sample: (2.4Å, flat PG(002), open collimation)	1.5×10^6 neutrons/cm ² s
Analyser crystals:	PG(002) Ge (311)
Range of scattering angles:	Monochromator: $19^\circ < 2\theta_m < 66^\circ$ Sample: $-110^\circ < 2\theta_s < +110^\circ$ Analyser: $-110^\circ < 2\theta_A < 120^\circ$
Collimators available:	RM: 20', 40', open (=60') MS: 20', 40' SA: 20', 40' AD: 30', 60'
Energy resolution:	$\Delta E / E : 5-10\%$

5.7 Experimental method:

The triple axis spectrometer measurements were performed at the Hahn-Meitner Institute, Berlin, Germany on E7 spectrometer. The CsFeBr₃ crystal used was grown by the Bridgeman method. It was cylindrical in shape of about 3.5 cm³ and the lattice constants of CsFeBr₃ are $c = 6.322 \text{ \AA}$ and $a=b= 7.544 \text{ \AA}$. The crystal was mounted in a DISPLEX to avoid deterioration from the atmosphere. The crystal was oriented such that its (110) and (002) scattering plane was horizontal.

Neutron of wavelength 2.41 \AA was provided using the (002) reflection from pyrolytic graphite as a monochromator. The analyser was also PG 002 and the collimation was 60'-40'-40'-60'. The dispersion of phonon excitation

was then measured by the constant Q-method along $[0\ 0\ l]$ ($l = 3$ and -1) and along $[h\ k\ 0]$ ($h=k=2$) and $[h\ k\ 2]$ ($h=k=0$) at room temperature. The positions of the experimental measurements in reciprocal space are indicated as in Figure 5.5.

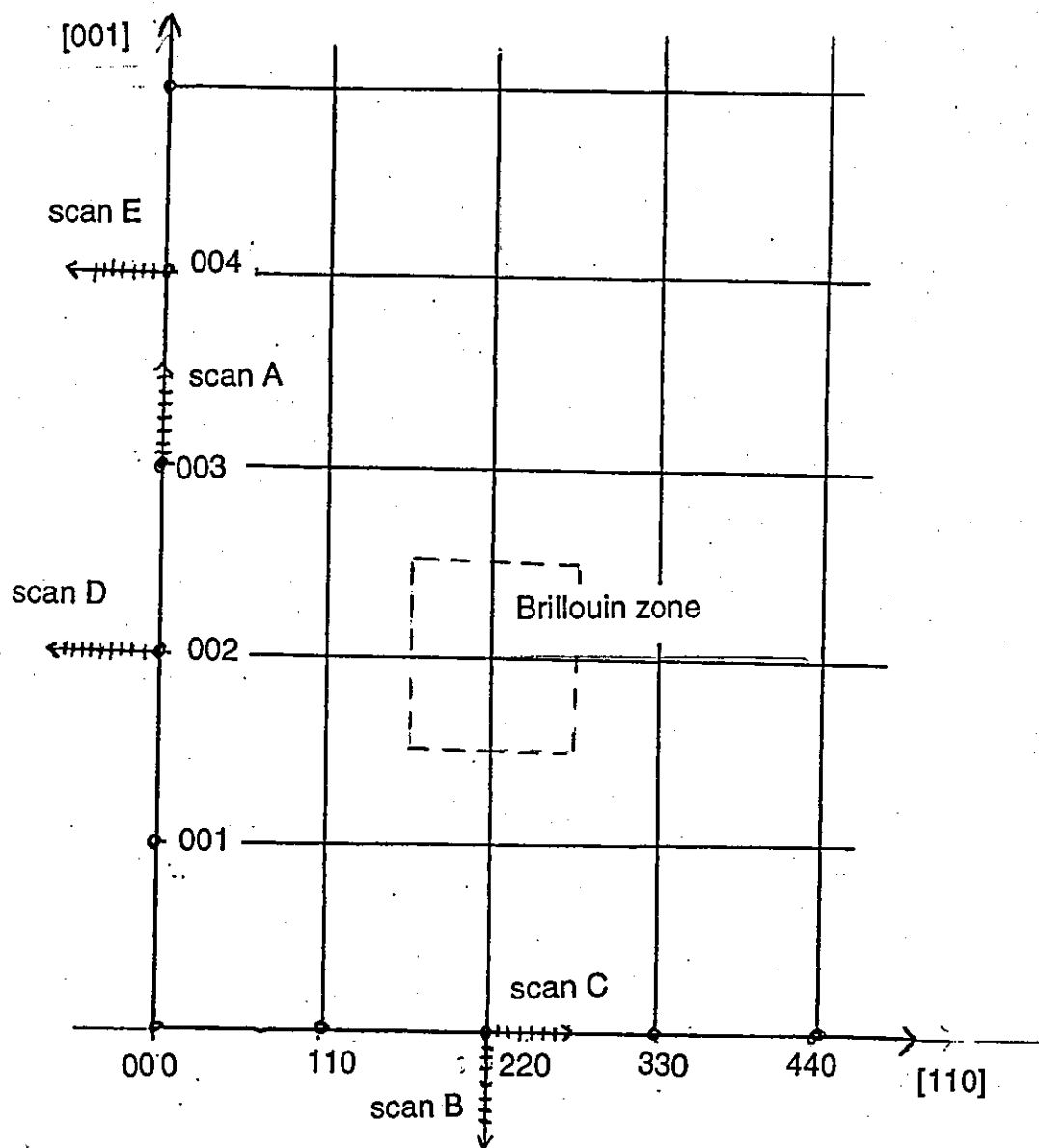


Figure 5.5: $(h\ k\ l)$ reciprocal lattice plane for the unit cell of CsFeBr_3 . The arrows indicate directions along which scan were made.

5.8 Results:

The dispersion relations of the longitudinal acoustic (LA) and transverse acoustic (TA) phonons for the [001] and [110] were measured at the following points in the Brillouin zone (see Figure 5.5)

- a. LA [001] along $Q(0\ 0\ 3+l)$ scan A
- b. TA [001] along $Q(2\ 2\ 0-l)$ scan B
- c. LA [110] along $Q(2+h\ 2+h\ 0)$ scan C
- d. TA [110] along $Q(0-h\ 0-h\ 2)$ and $Q(0-h\ 0-h\ 4)$ scan D and E

It was necessary for some parts of the phonon dispersion to measure at different positions in the Brillouin zone. Keeping in mind the physical limitation of the scattering angles involved for setting the spectrometer and the intensity of the elastic Bragg positions from where the dispersion curves are measured (the structure factor increases with increasing Q and strong intensities of the phonon excitations occur around strong Bragg position which are reflections).

The inelastic neutron scattering peaks were fitted assuming Gaussian profiles by means of the least square method taking product of height times width. The program used was an adapted version of Pk Fit (ILL-source) for data collected on the E7 spectrometer at HMI-Berlin. The data were taken using k_i as constant, therefore the data were also corrected for the analyser efficiency, $k_F^3 \coth \theta_A$, as well as for PG analyser reflectivity which can be observed in a change of the background scattering.

The scattering profiles (with fitted data) and derived dispersion curves are presented in the following tables and figures.

Mode	Table	Figure (scattering profile)	Figure (dispersion curve)
LA [001]	5.1	5.6	5.7
TA [001]	5.2	5.8	5.9
LA[110]	5.3	5.10	5.11
TA [110]	5.4	5.12	5.13

5.8.1 Longitudinal acoustic (LA) [001]:

Typical scattering profiles observed along the [001] are as shown in Figure 5.6. Along this direction (parallel to the chain axis), a longitudinal acoustic (LA) phonon which has a zone boundary energy of ~ 5.5 meV was observed. The change of the intensity of the phonon excitations along the [001] direction indicates the presence of an optical phonon as shown in Figure 5.7. Both excitations are clearly resolved above $Q(0\ 0\ 3.25-3.50)$. The scattering profiles indicate that the optical phonon has a very small gap at the zone boundary $\sim 1-2$ meV. The energy of this longitudinal optical (LO) phonon increases to ~ 9.0 meV at the zone boundary.

5.8.2 Transverse acoustic (TA) [001]:

The transverse acoustic (TA) phonon along $[0\ 0\ 1]$ direction was measured at $Q(2\ 2\ 0-l)$ and its scattering profiles are as shown in Figure 5.8. It was observed that the phonon does not have an energy maximum at the zone boundary as shown in Figure 5.9. The phonon energy seems to level off for values of $l=0.7-0.8$. It is not clear whether the phonon energy towards the second zone centre at $l = -1.0$ increases or decreases in energy.

5.8.3 Longitudinal acoustic (LA) [110]:

The dispersion perpendicular to the chain was studied at $Q(2+h\ 2+h\ 0)$ - scan C. The scattering profiles are as shown in Figure 5.10. From the dispersion curve, again in this direction we find a maximum half way the zone boundary at ~ 6 meV as shown in Figure 5.11. The phonon energy decreases towards ~ 3 meV at the zone boundary.

5.8.4 Transverse acoustic (TA) [110]:

The dispersion curve perpendicular to the c -direction (chain axis) was measured along the $Q(0-h\ 0-h\ 2)$ and $Q(0-h\ 0-h\ 4)$ direction. The scattering profiles are as shown in Figure 5.12 and the dispersion curve obtained is shown in Figure 5.13.

It is not clear from the data taken at Q(0-h 0-h 2) direction what was happening for wavevectors larger than 0.3, the scattered intensity was too low (see Figure 5.12). Therefore, we tried to measure these points at Q(0-h 0-h 4). The intensity gain by going to higher Q values allowed us to measure the wavevectors > 0.3 around this Q point and to finalised the dispersion curve. We observed a maximum of ~ 2 meV at Q(-.25 -.25 2,4). The excitations decrease towards the zone boundary to a value of ~ 1.5 meV.

From the initial slopes of the dispersion curves, the sound velocity can be deduced and with the calculated value of density $\rho = 4260 \text{ kgm}^{-3}$ for CsFeBr₃, the elastic constant C_{11} , C_{33} , C_{66} and C_{44} can be calculated as shown in Table 5.3.

Table 5.3 Values of elastic constant at room temperature of CsFeBr₃

Mode	$v \text{ ms}^{-1}$	$\rho v^2 \times 10^{10} \text{ Nm}^{-2}$
C_{11} (LA)	3983	7.33
C_{66} (TA)	1477	1.01
C_{33} (LA)	2371	2.58
C_{44} (TA)	1103	0.56

Table 5.1 Phonon excitation energy of CsFeBr₃ at room temperature (parallel to the chain axis) Q (0 0 3+l)

Q	Energy meV	Energy meV
0.0 0.0 3.90	1.16	1.75
3.85	2.10	3.85
3.80	3.03	
3.75	3.92	
3.70	4.60	6.66
3.65	4.95	7.07
3.60	4.99	7.97
3.5	5.02	9.15

Table 5.2: Phonon excitation energy of CsFeBr₃ at room temperature (parallel to the chain axis) Q (2 2 0-l)

Q	Energy meV
2.0 2.0 -0.15	0.7839
-0.20	1.0288
-0.30	2.0268
-0.40	2.7376
-0.50	3.4894
-0.60	4.2642
-0.70	5.0380
-0.80	5.2961

Table 5.3: Phonon excitation energy of CsFeBr₃ at room temperature (perpendicular to the chain axis) Q (2+h 2+h 0)

Q	Energy meV
2.05 2.05 0	1.53
2.08 2.08	1.94
2.10 2.10	2.54
2.15 2.15	3.93
2.20 2.20	5.03
2.22 2.22	5.54
2.26 2.26	5.67
2.28 2.28	5.15
2.35 2.35	3.89
2.40 2.40	3.58
2.45 2.45	3.04
2.50 2.50	3.07

Table 5.4: Phonon excitation energy of CsFeBr₃ at room temperature (perpendicular to chain axis) Q (0-h 0-h 2,4)

Q	Energy meV
-0.10 -0.10 2.0	1.21
-0.20 -0.20	1.82
-0.22 -0.22	2.12
-0.25 -0.25	2.34
-0.28 -0.28	2.37
-0.30 -0.30	2.51
-0.35 -0.35	2.46
-0.40 -0.40	2.29
-0.50 -0.50	2.00

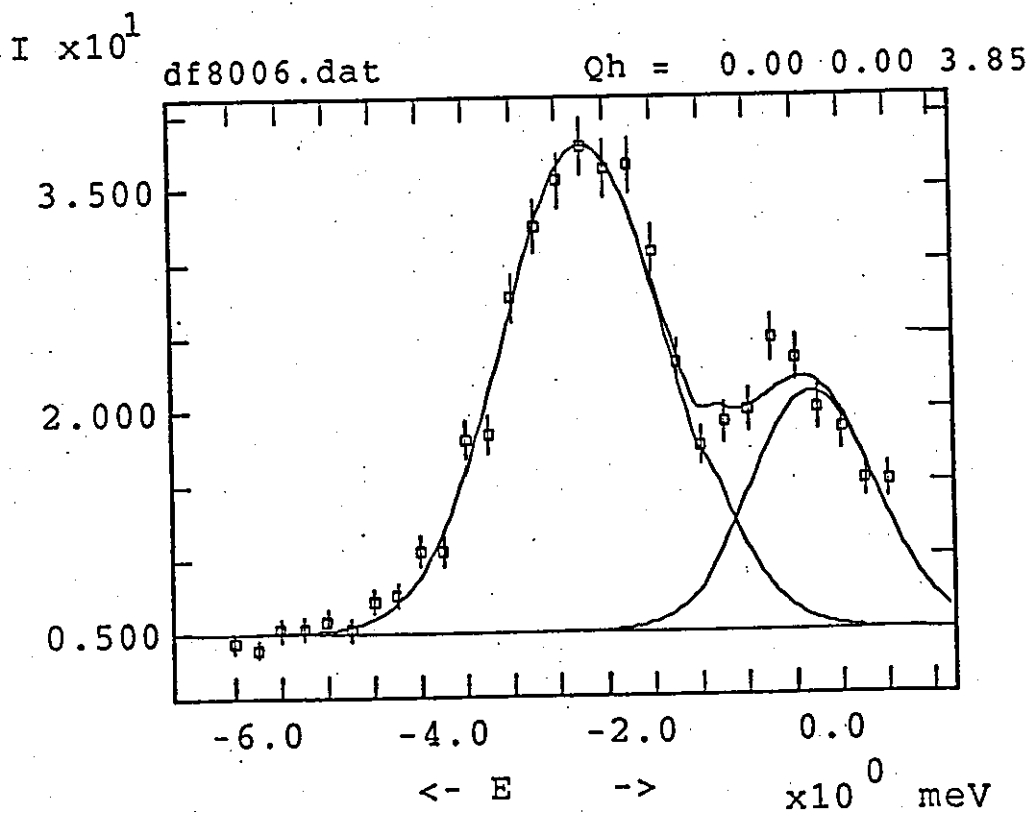
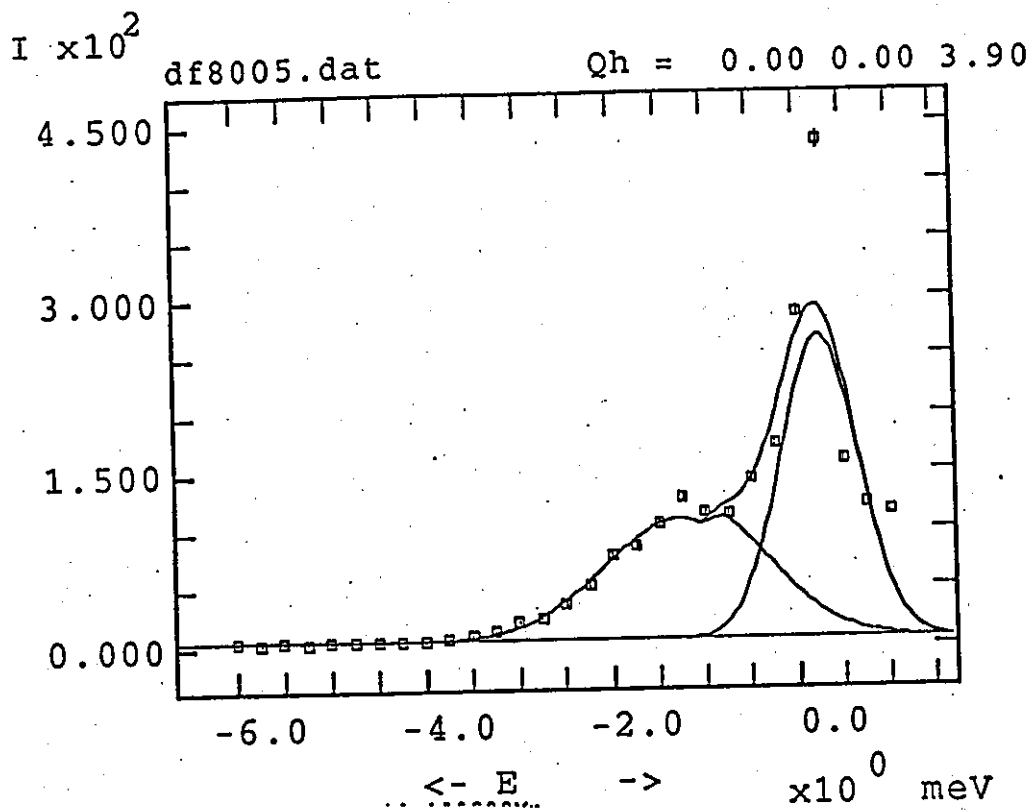


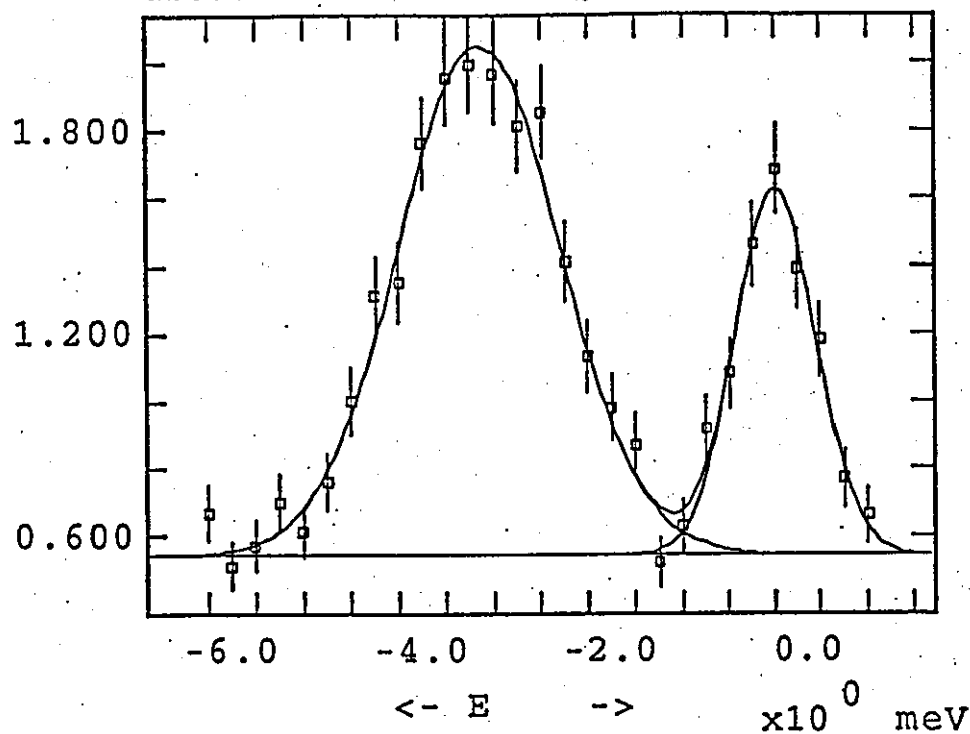
Fig. 5.6: Profiles of scattering $Q(0\ 0\ 3+l)$

continued

$I \times 10^1$

df8007.dat

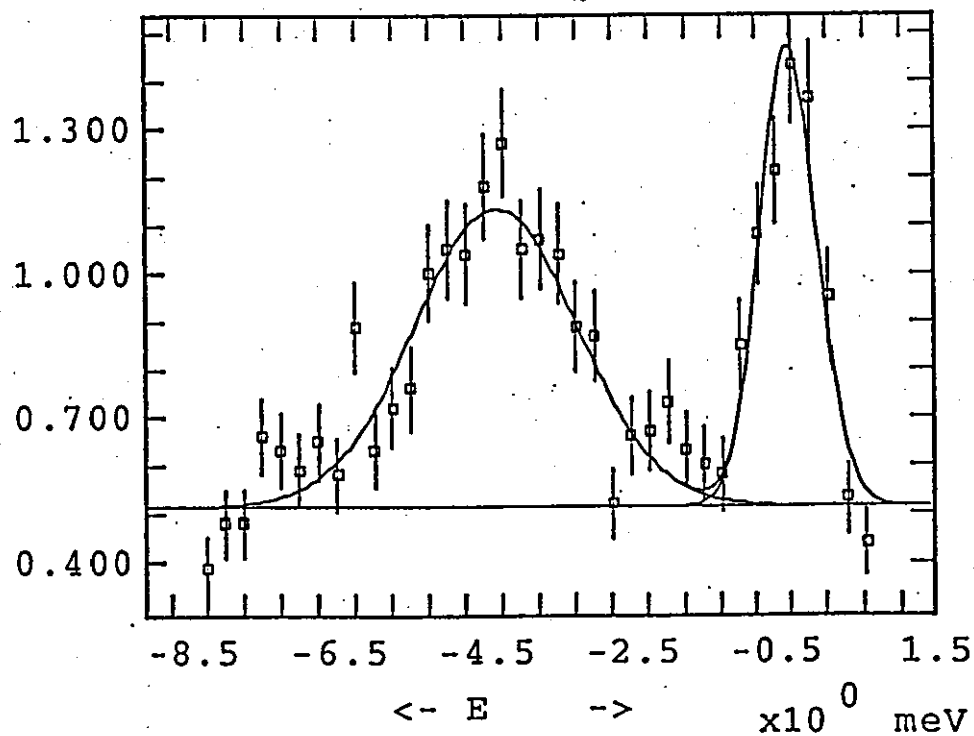
Qh = 0.00 0.00 3.80



$I \times 10^1$

df8011.dat

Qh = 0.00 0.00 3.75

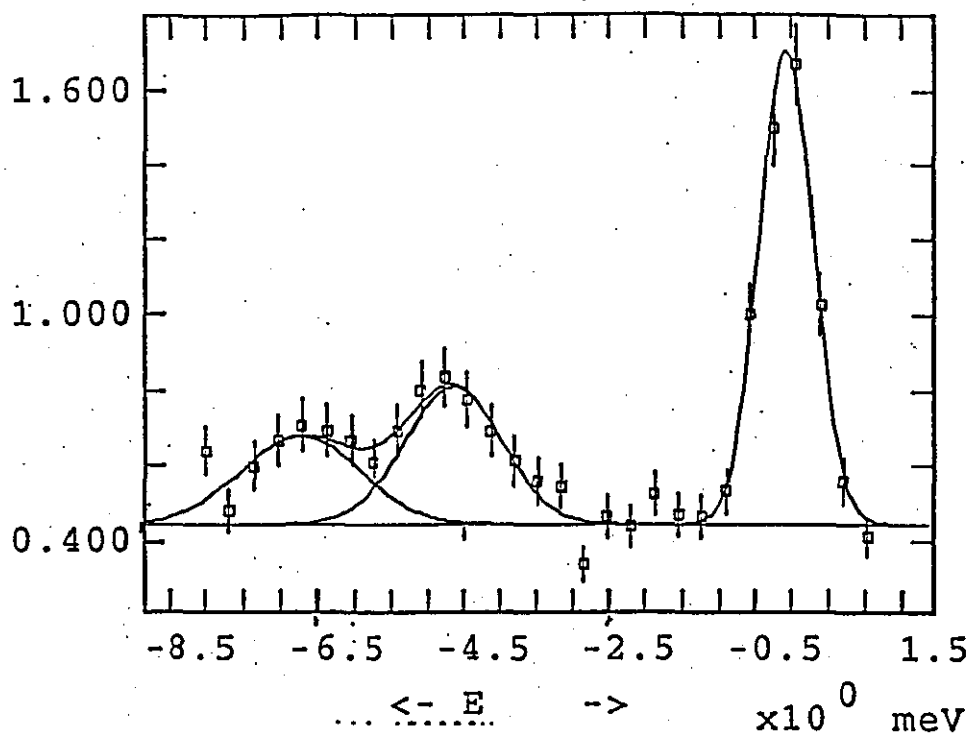


continued

$I \times 10^1$

df8008.dat

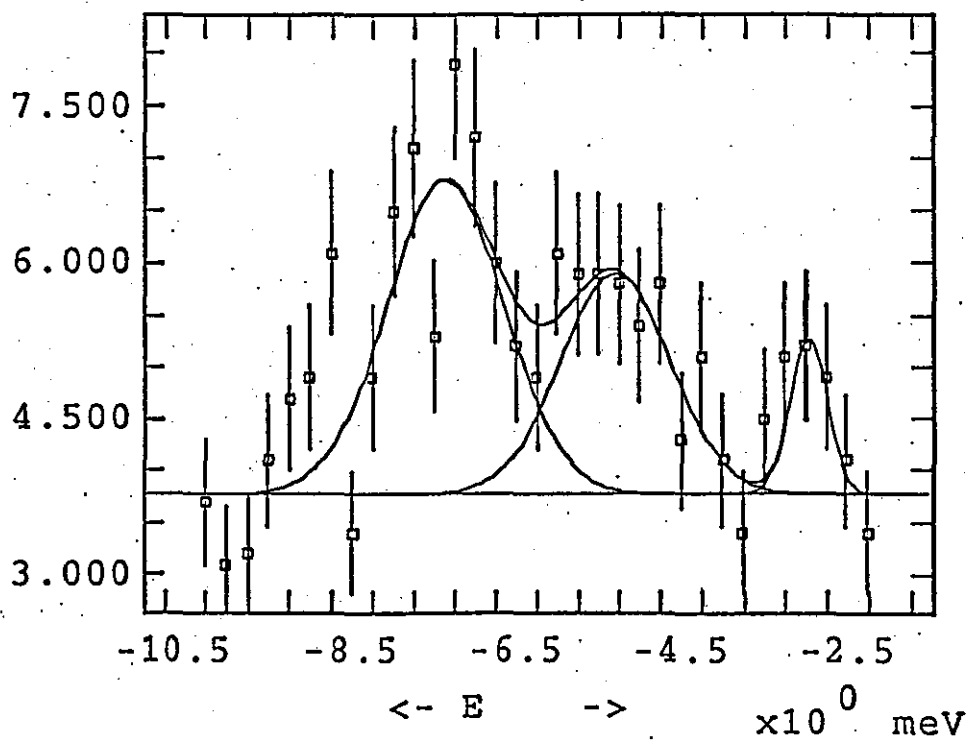
Qh = 0.00 0.00 3.70

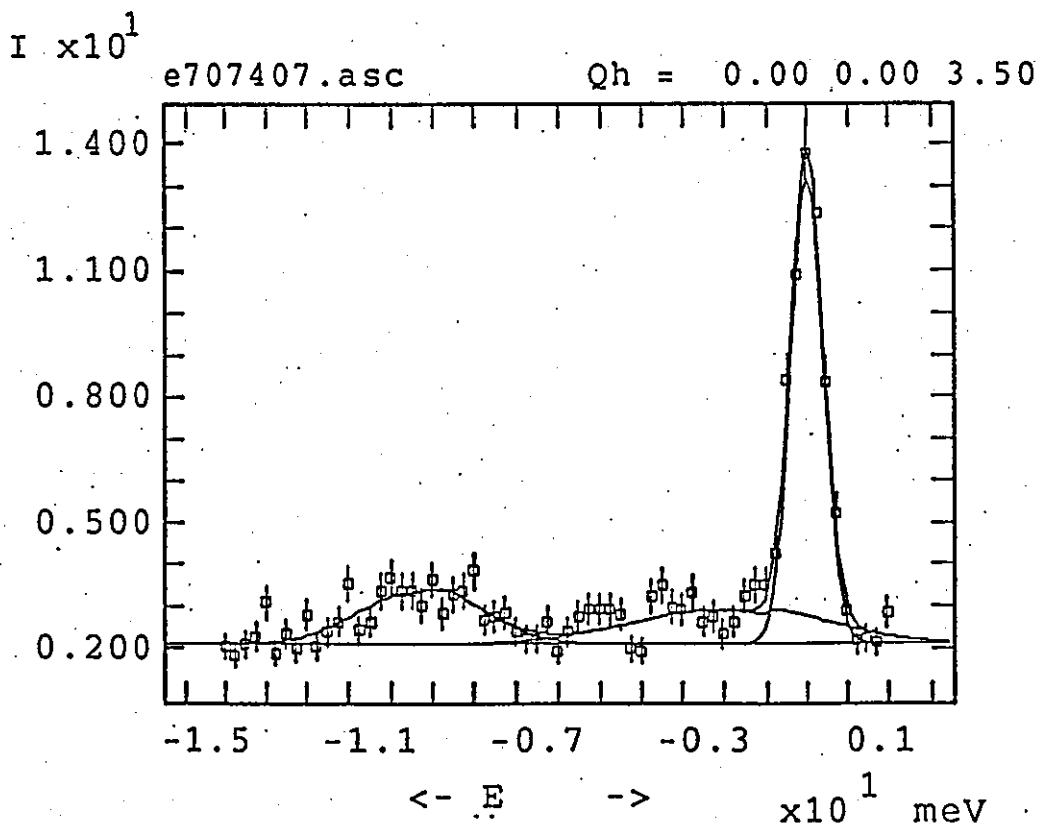
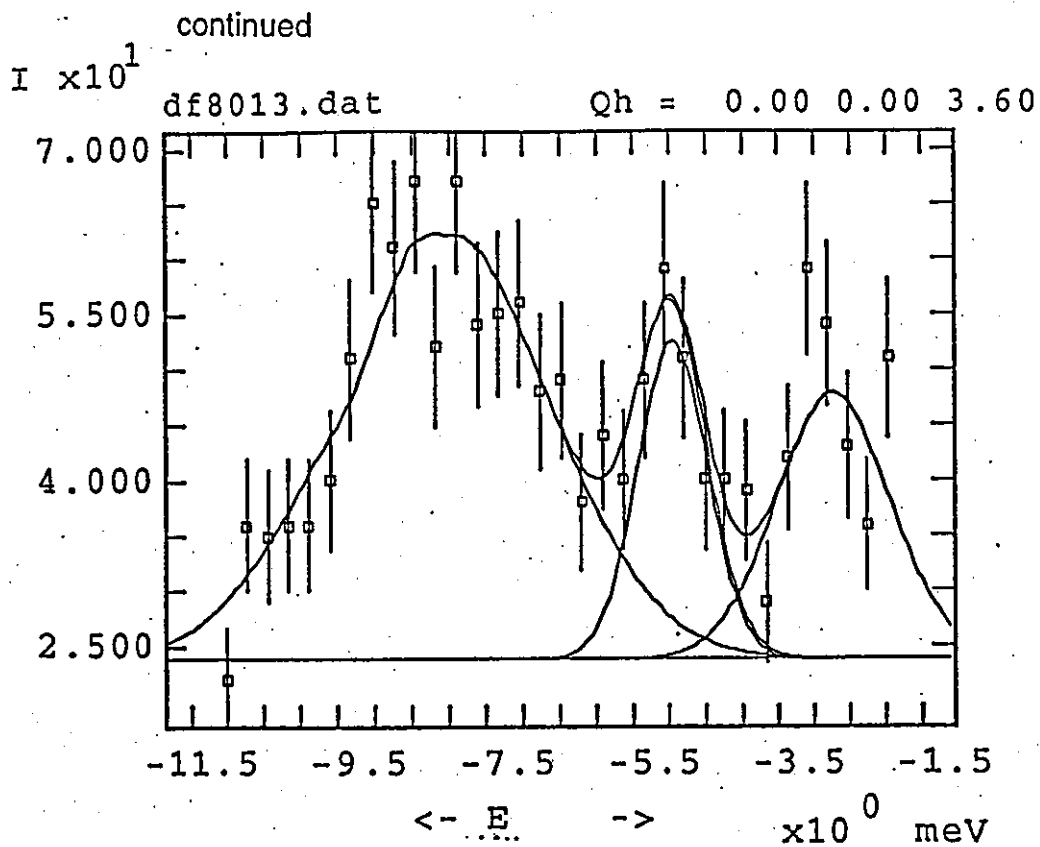


$I \times 10^1$

df8012.dat

Qh = 0.00 0.00 3.65





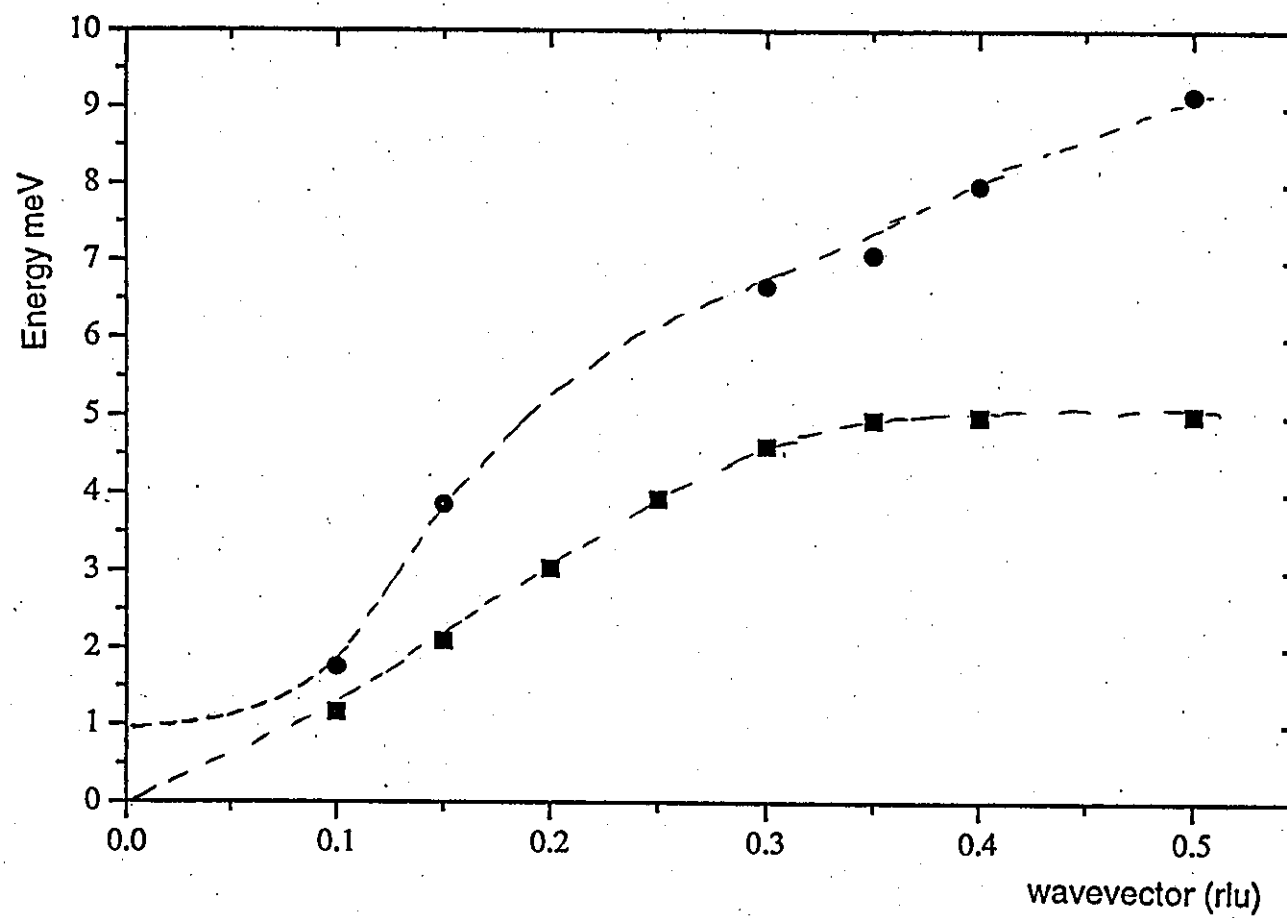


Fig. 5.7: Dispersion curve of LA [001] phonon (line as guide to the eye)

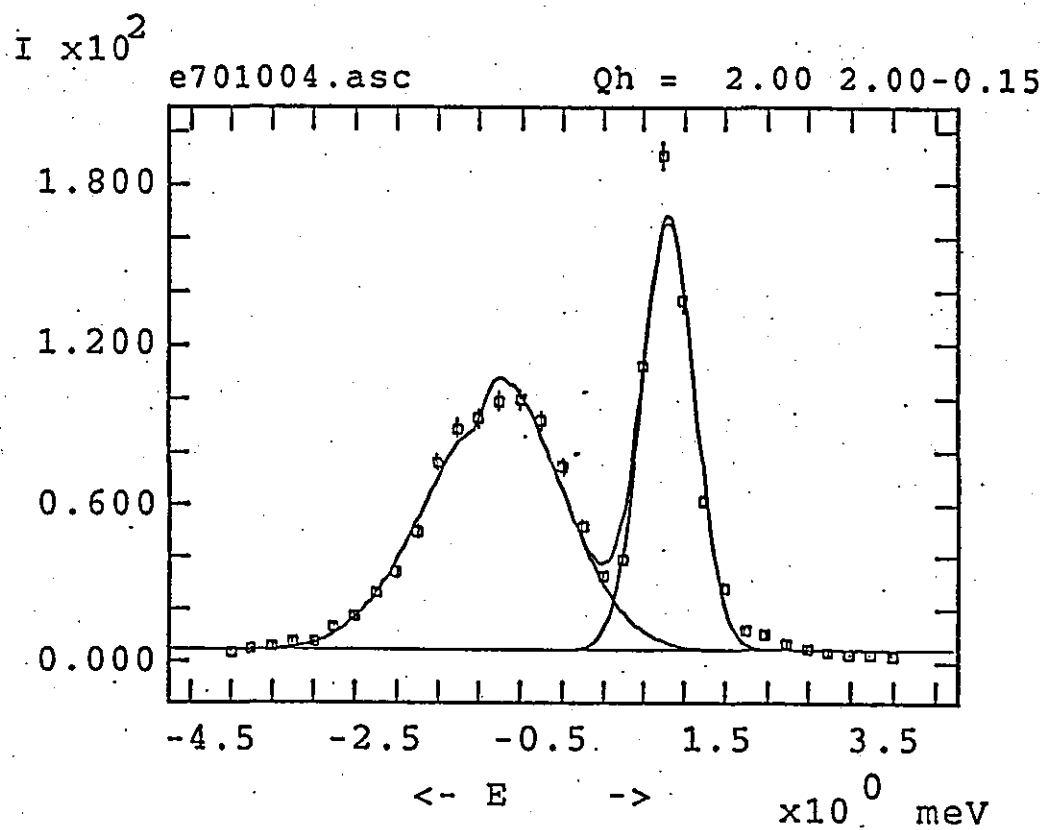
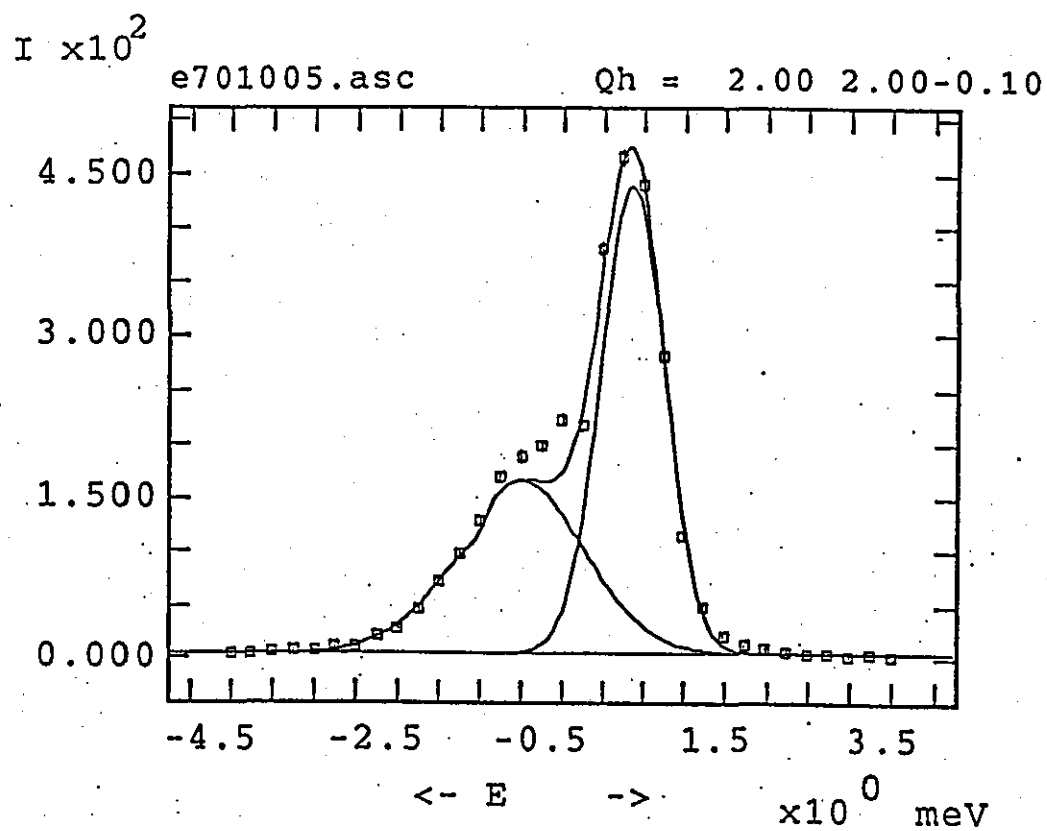
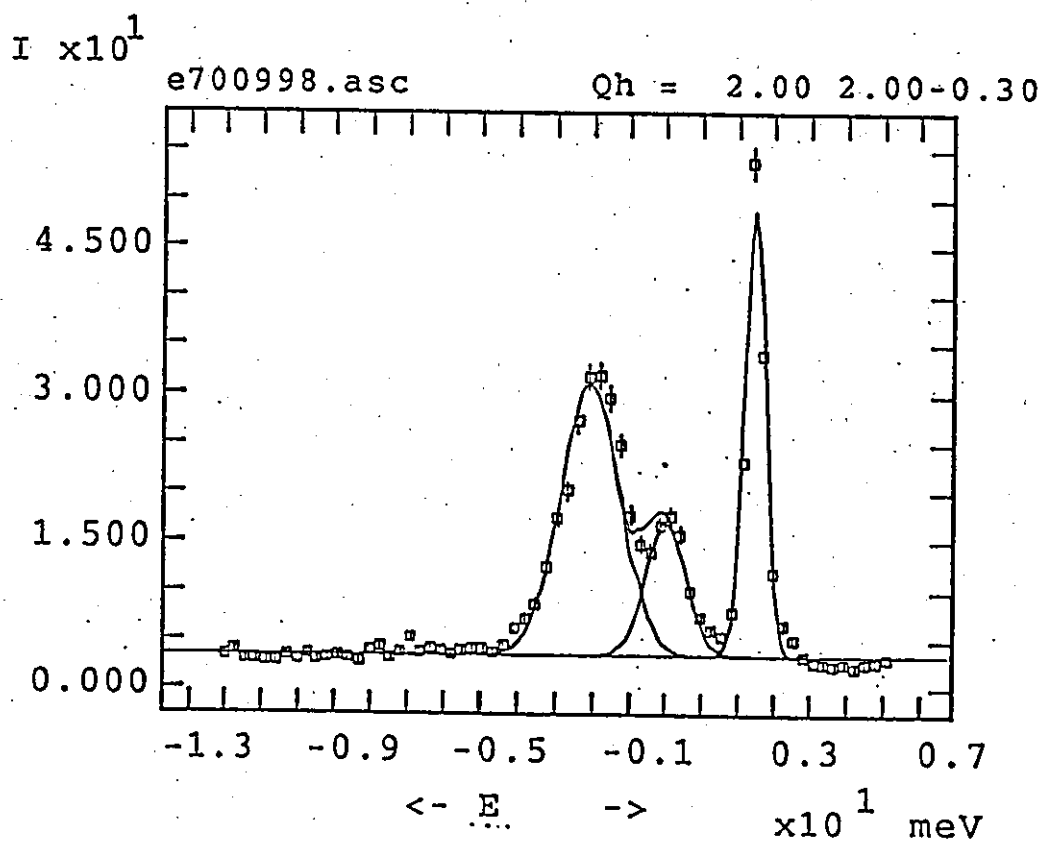
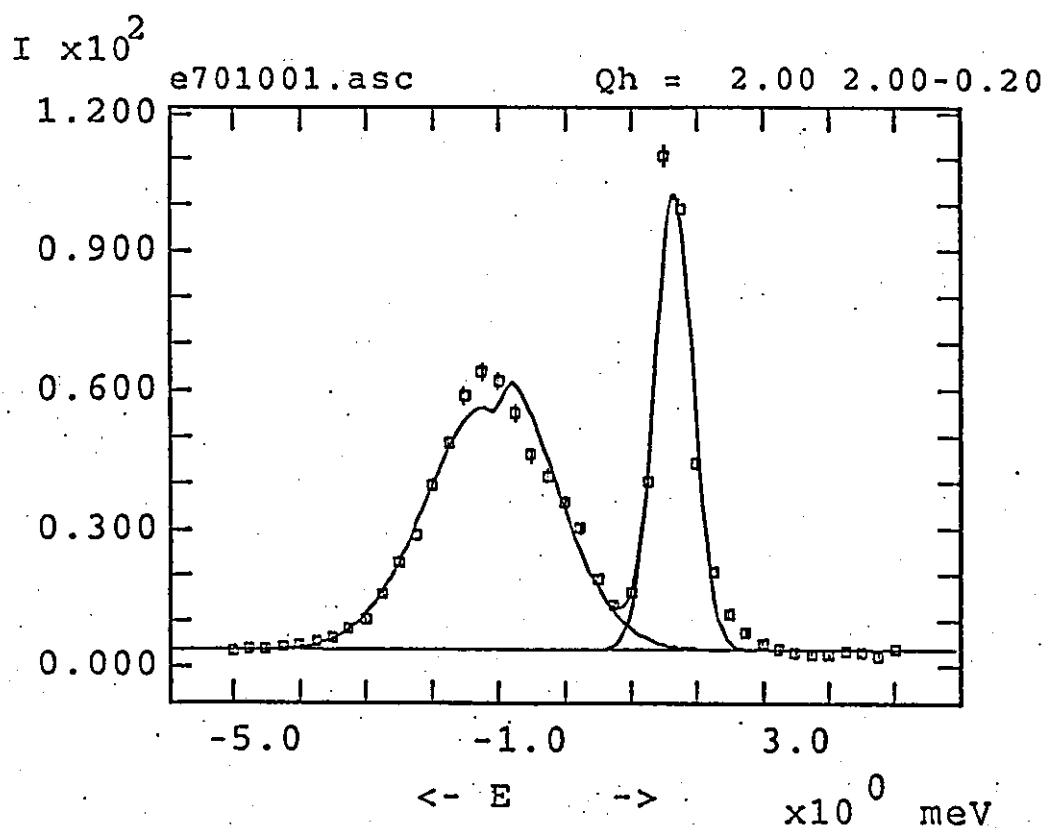


Fig. 5.8: Profiles of scattering Q(2 2 0-l)

continued

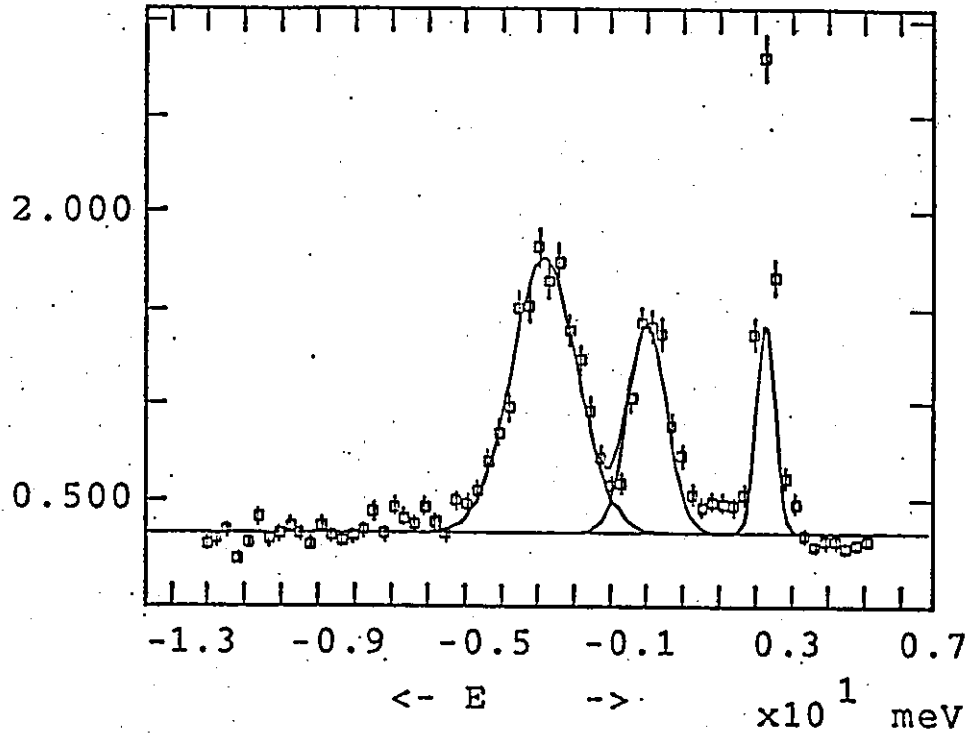


continued

$I \times 10^1$

e700996.asc

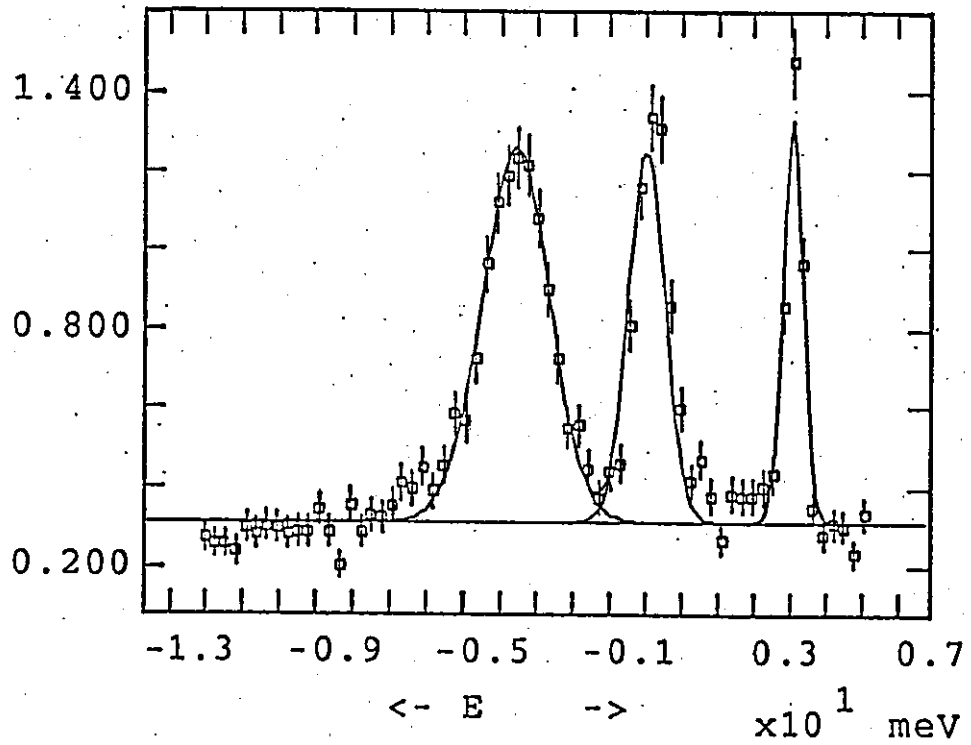
Qh = 2.00 2.00-0.40



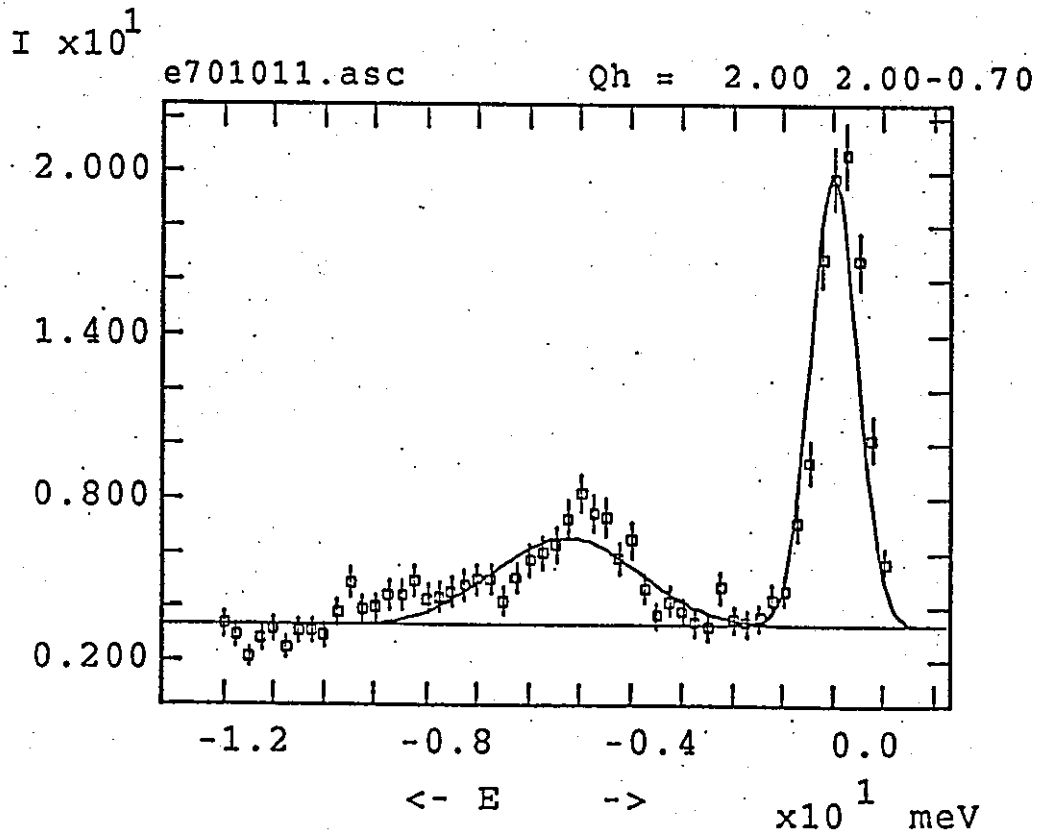
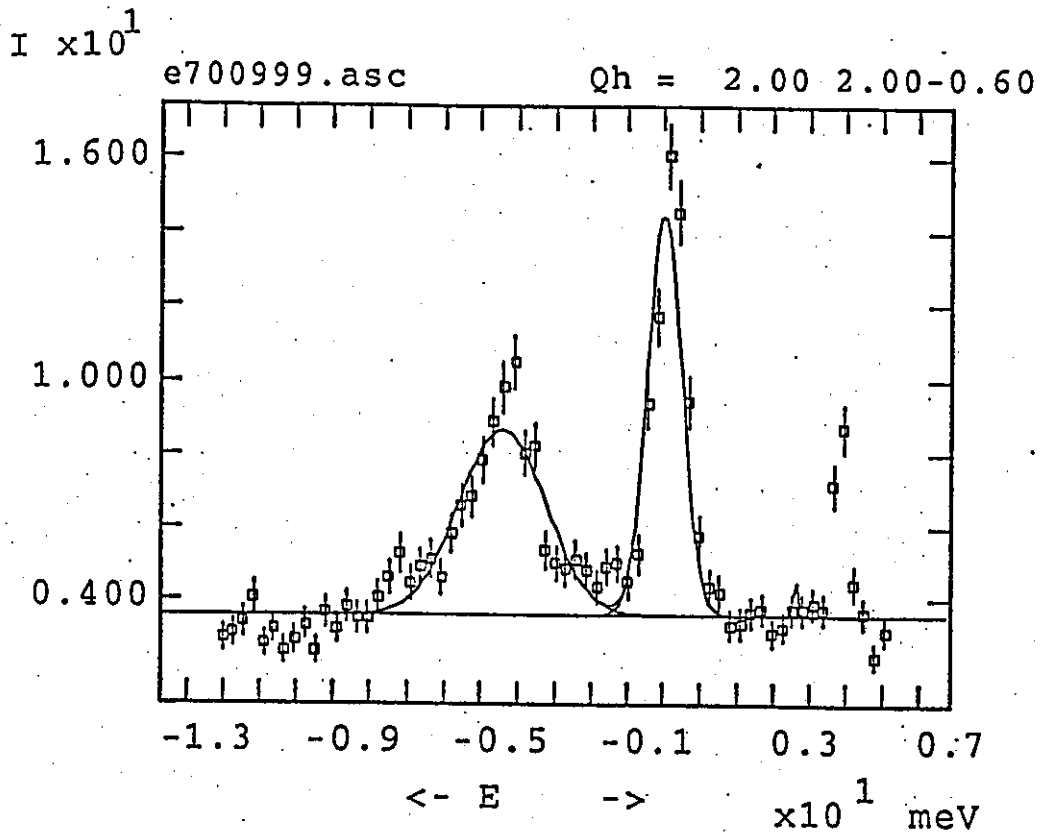
$I \times 10^1$

e700995.asc

Qh = 2.00 2.00-0.50



continued

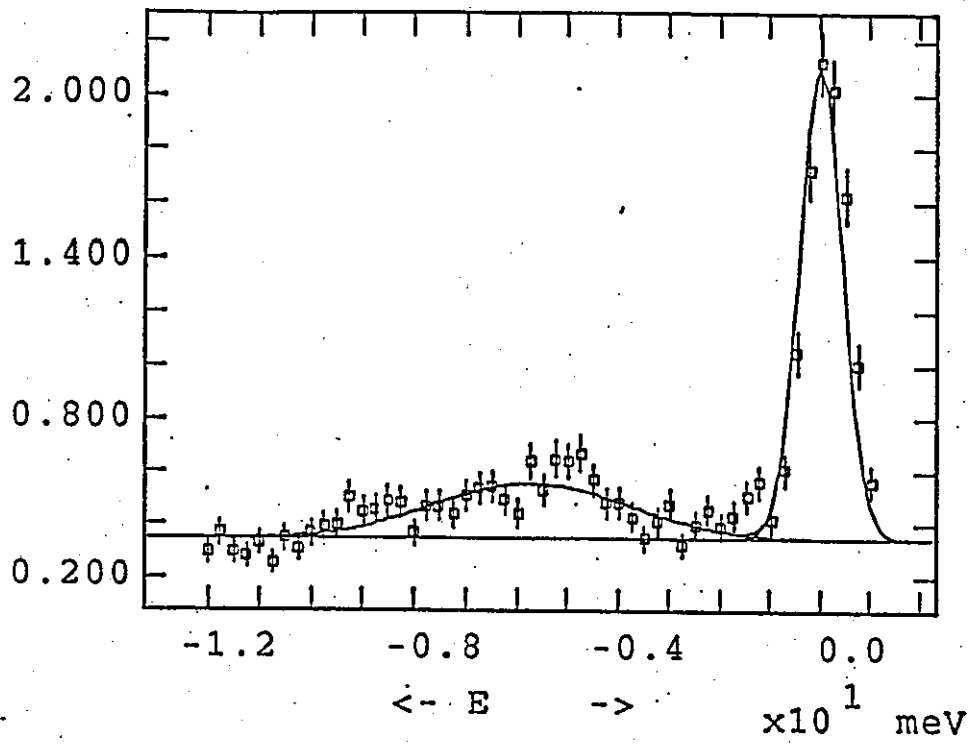


continued

$I \times 10^1$

e701010.asc

Qh = 2.00 2.00-0.80



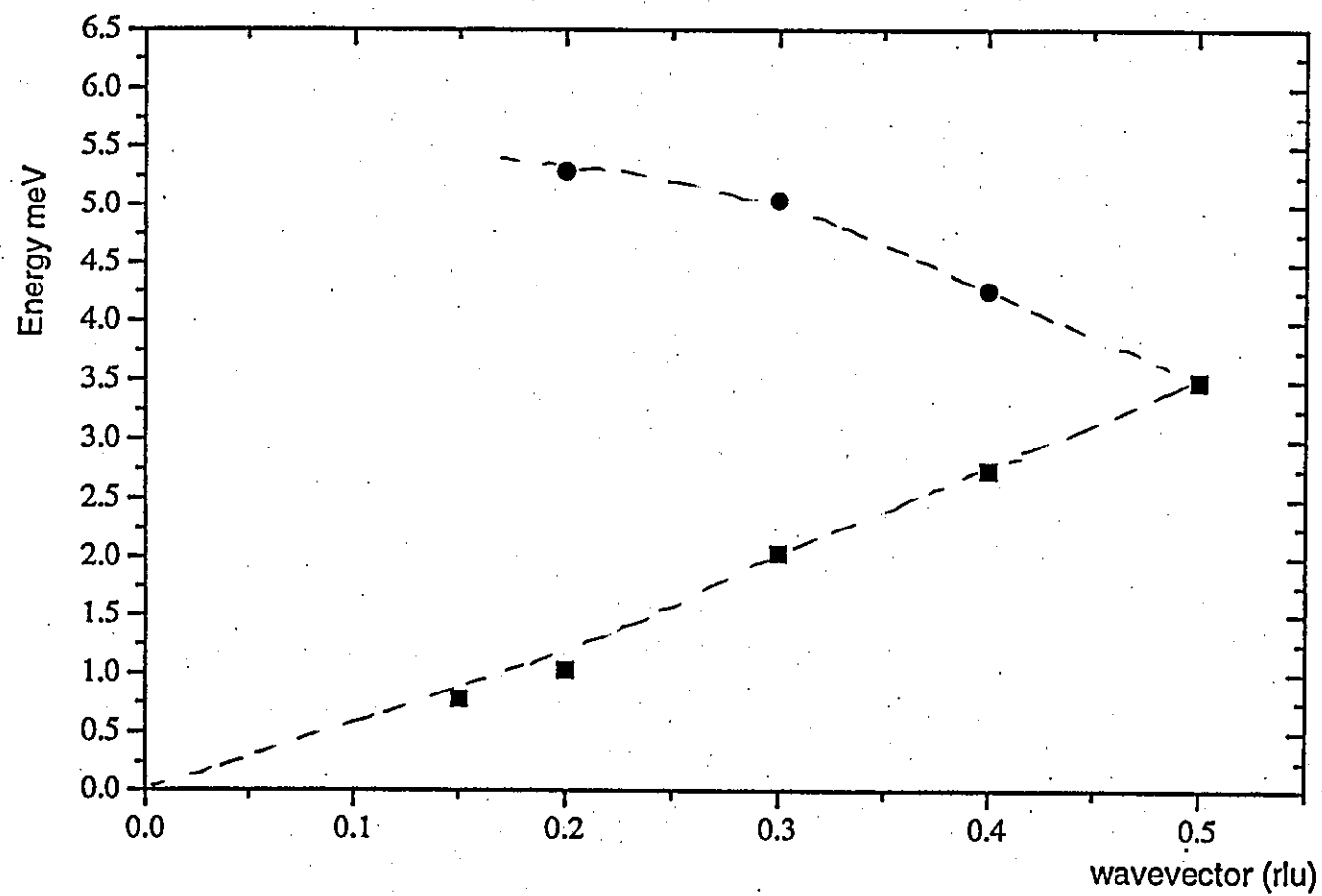


Fig. 5.9: Dispersion curve of TA [001] phonon (line as guide to the eye)

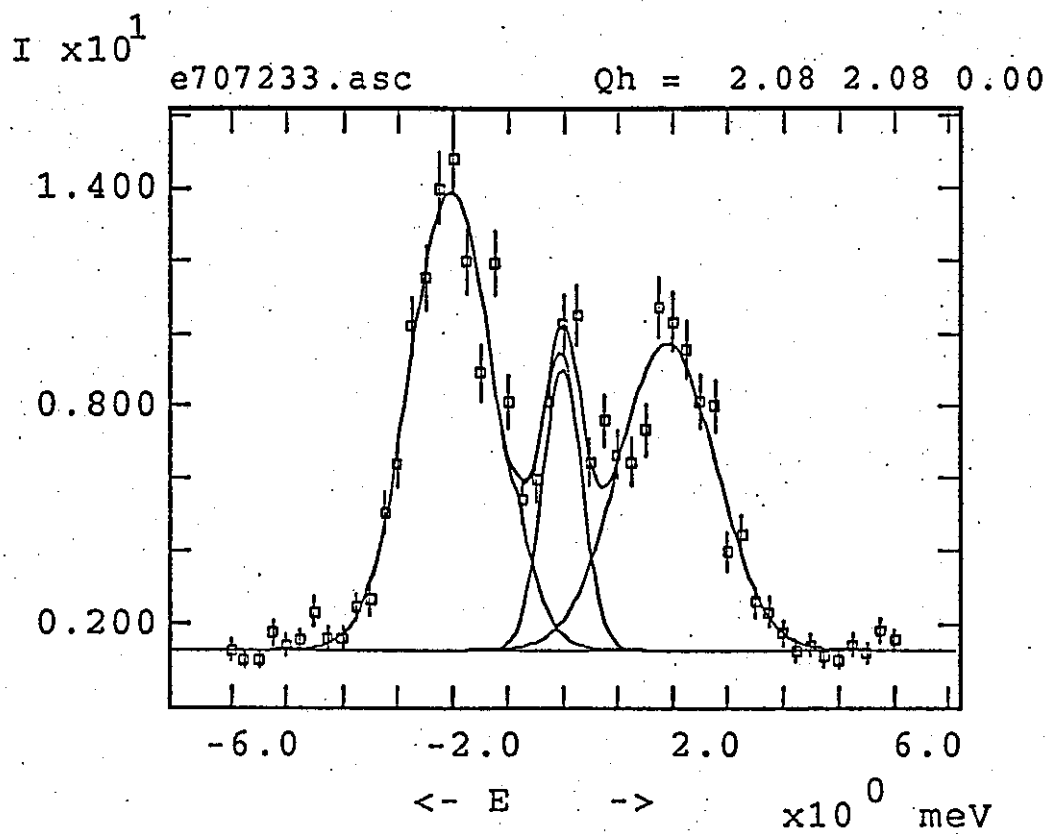
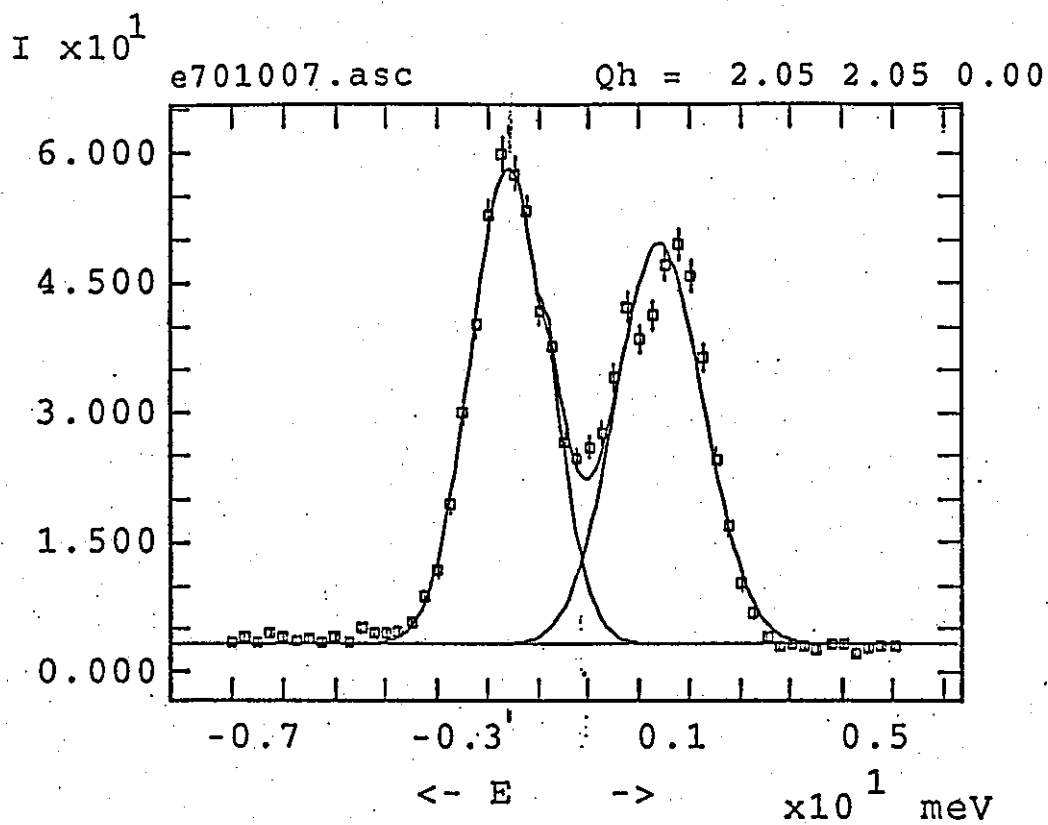


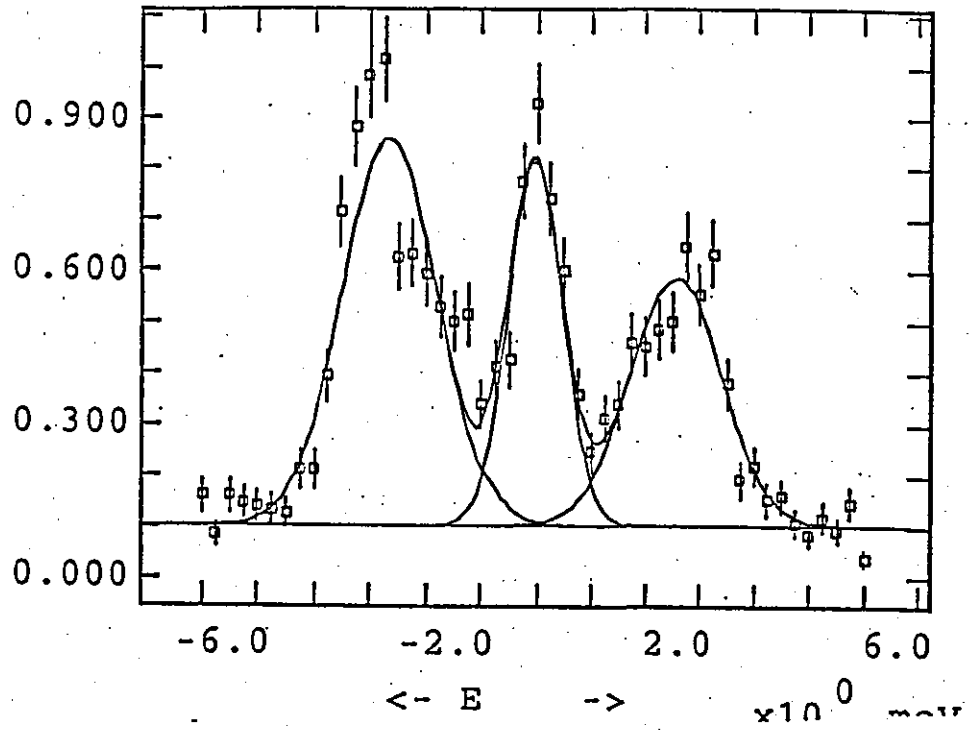
Fig. 5.10: Profiles of scattering $Q(2+h \ 2+h \ 0)$

continued

$I \times 10^1$

e707232.asc

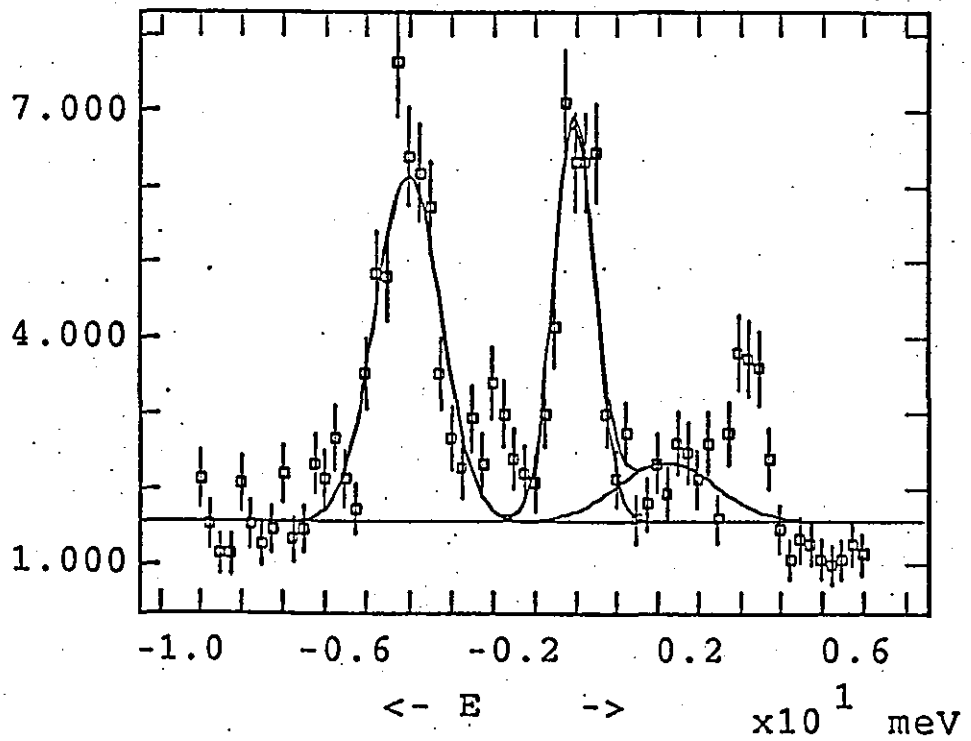
Qh = 2.10 2.10 0.00



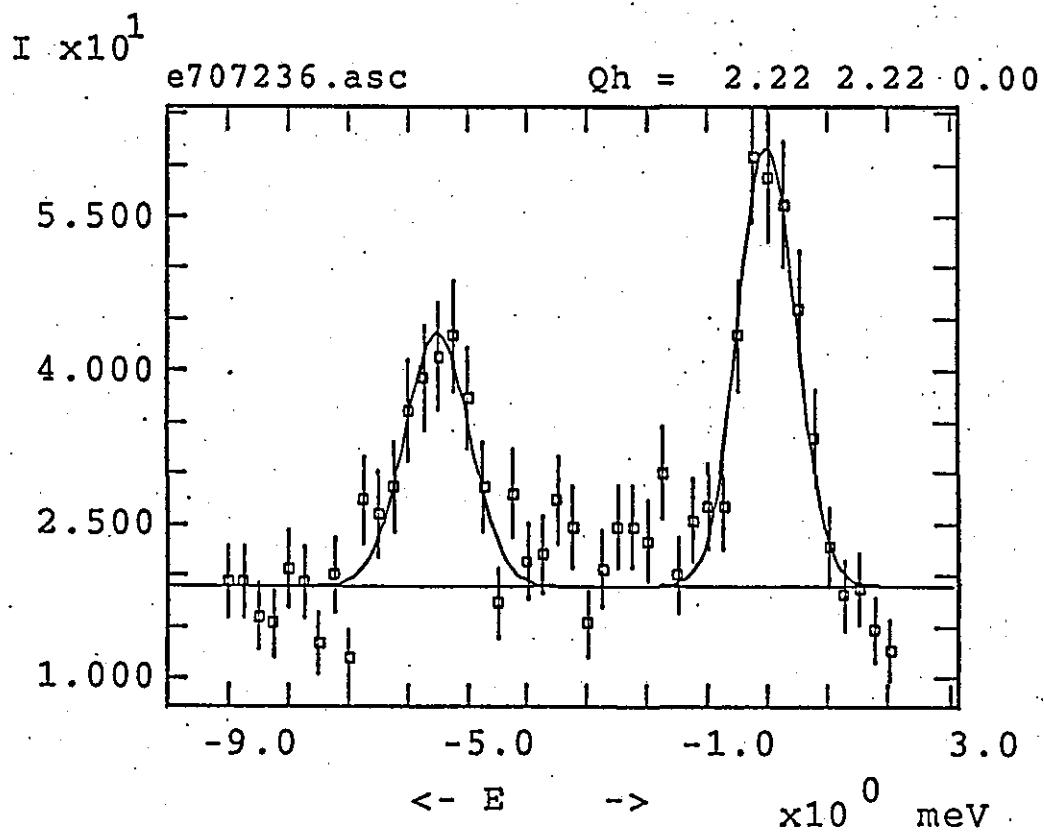
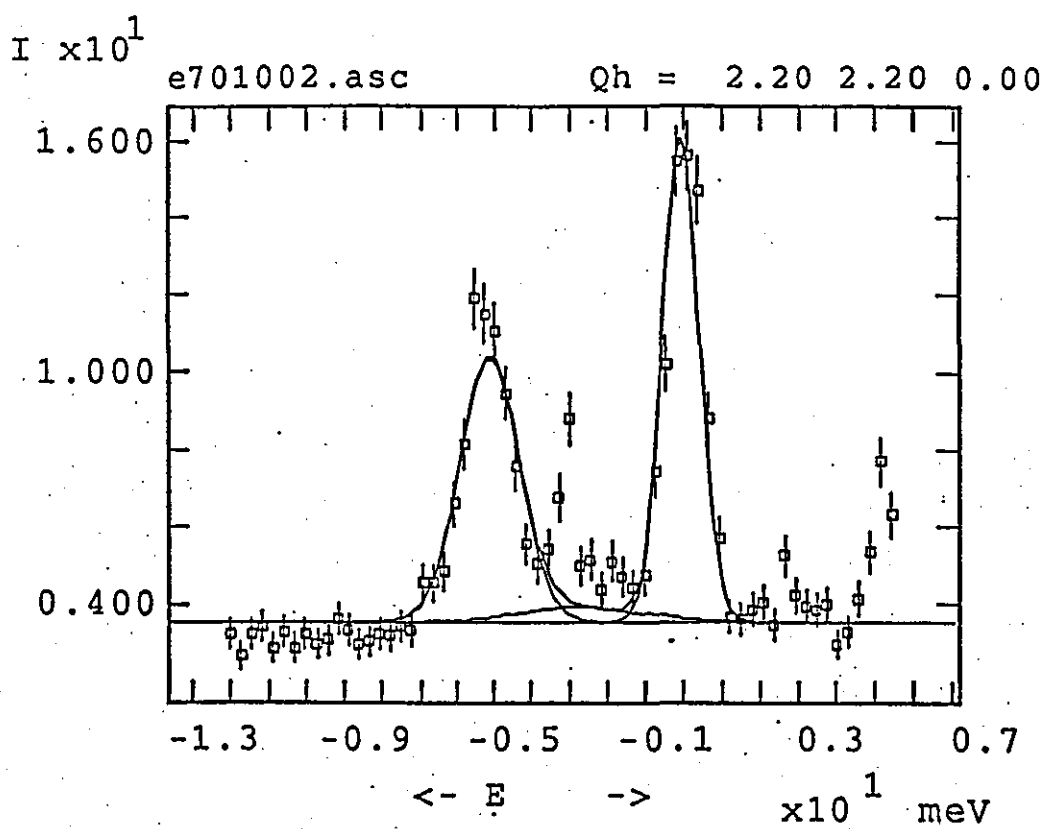
$I \times 10^1$

e707235.asc

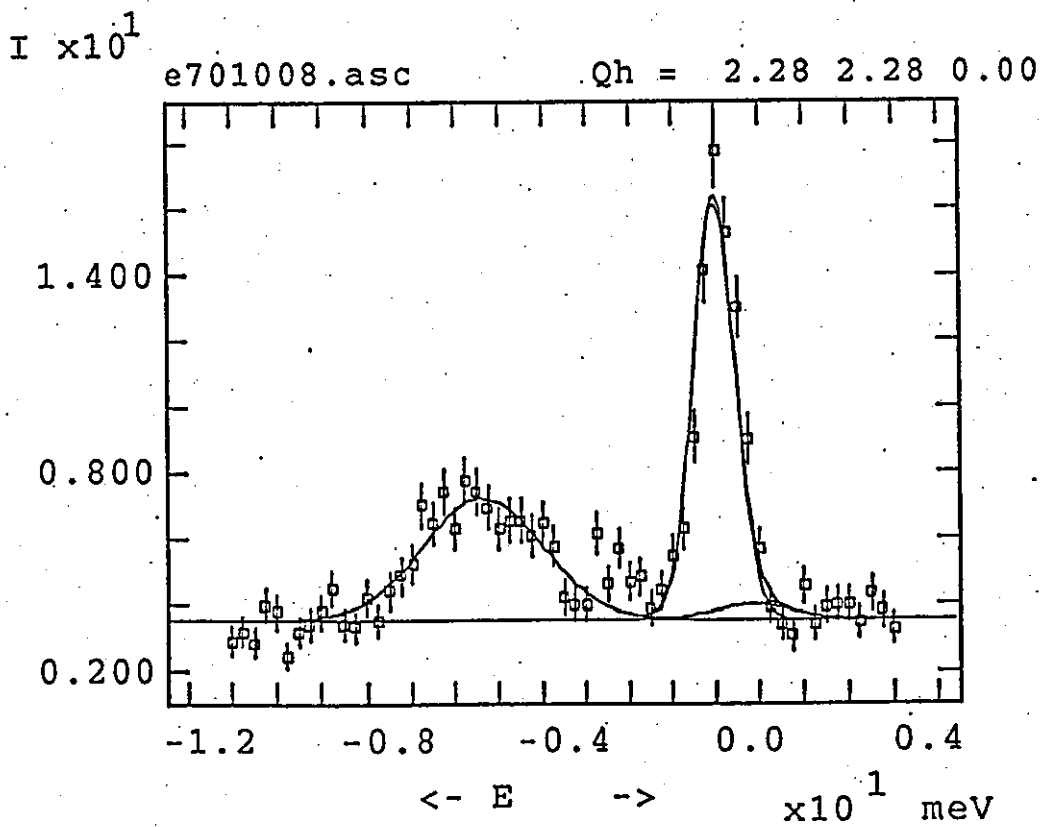
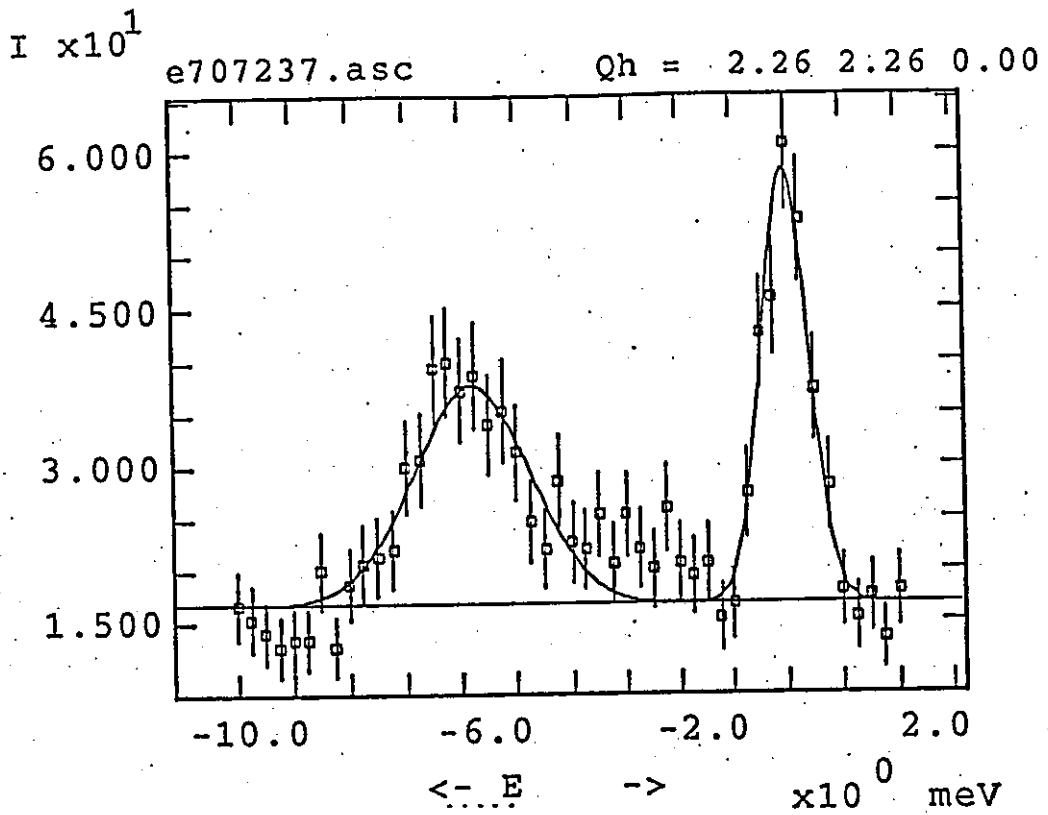
Qh = 2.15 2.15 0.00

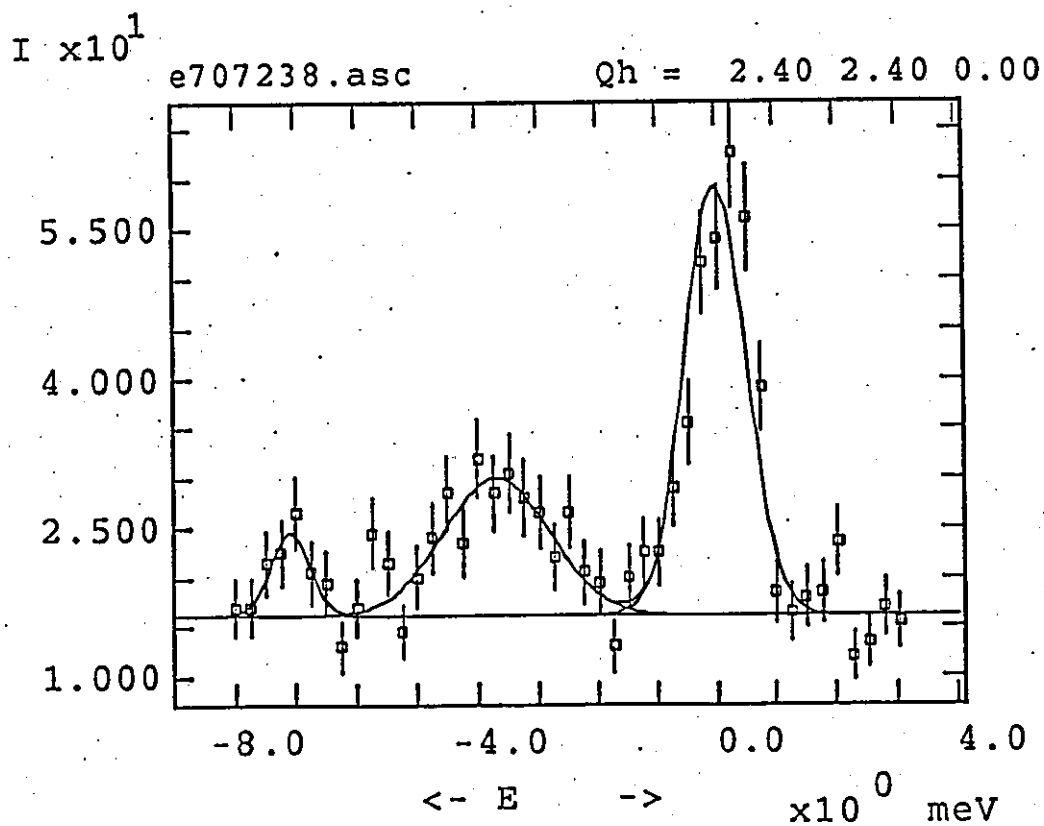
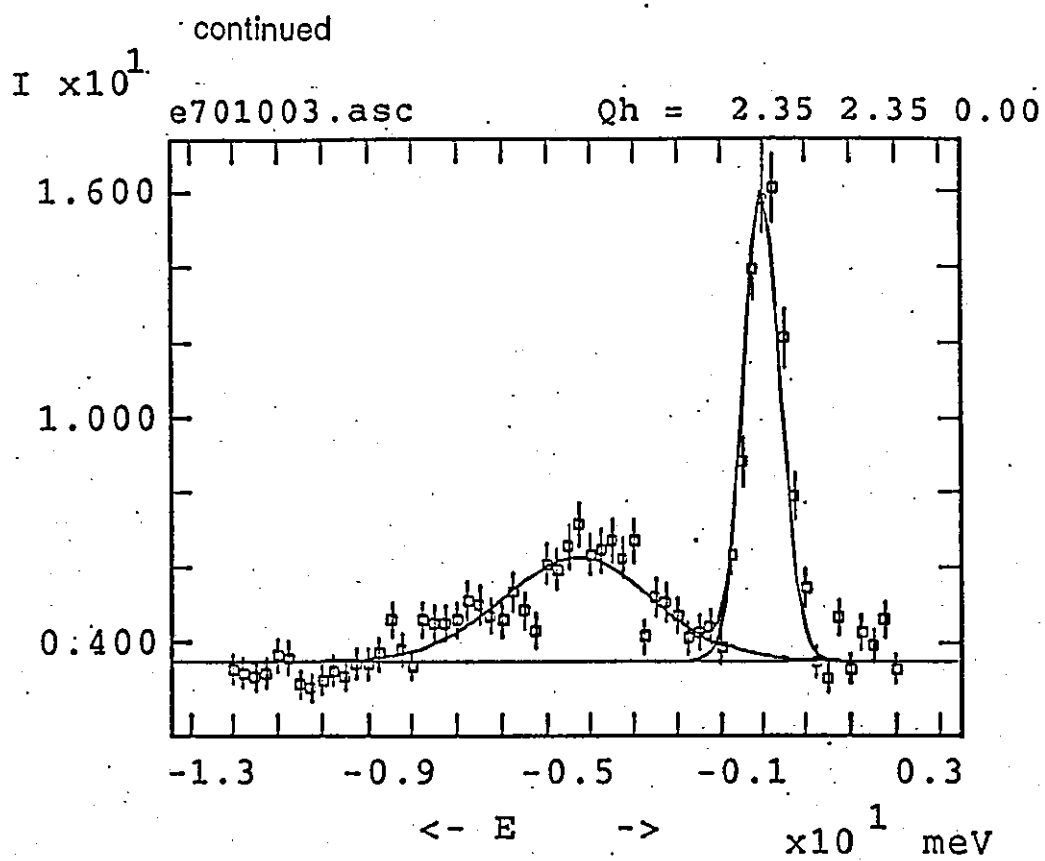


continued

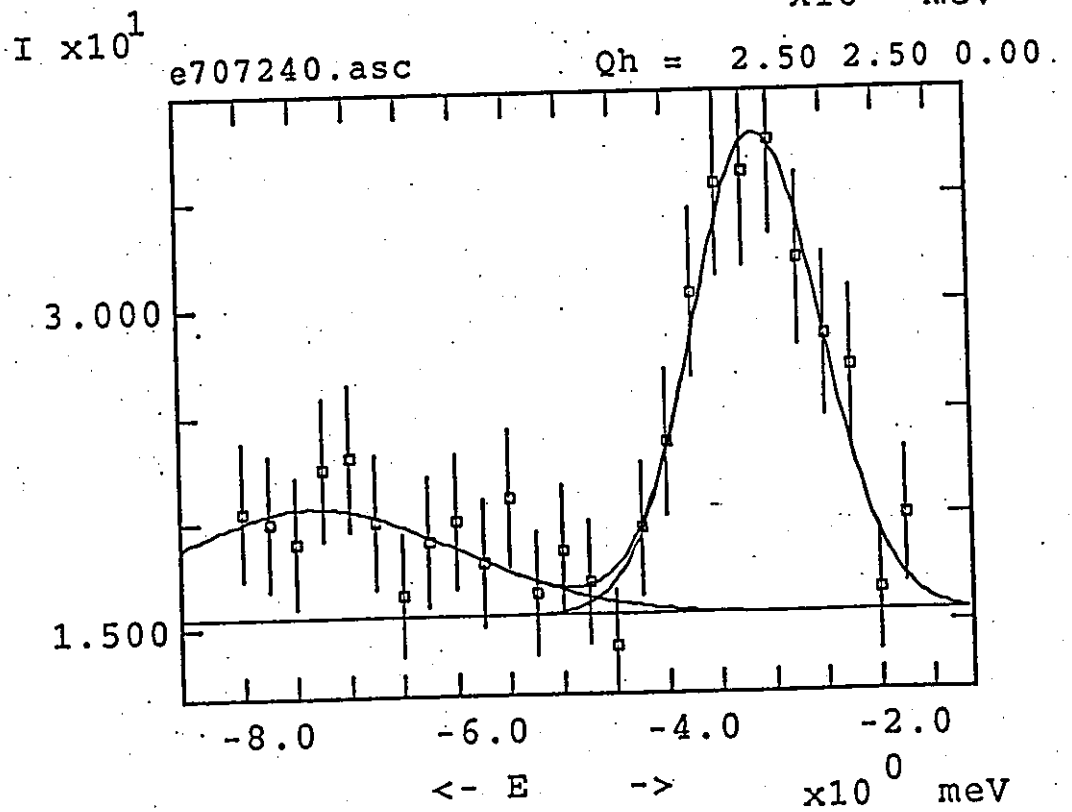
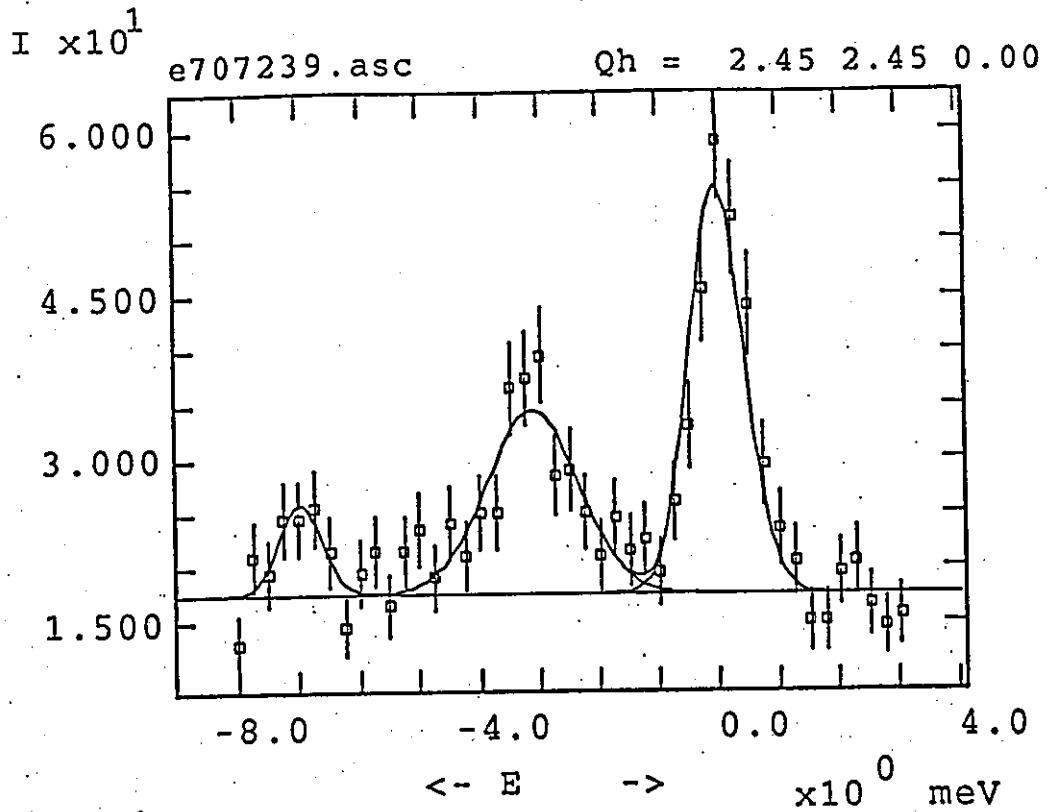


continued





continued



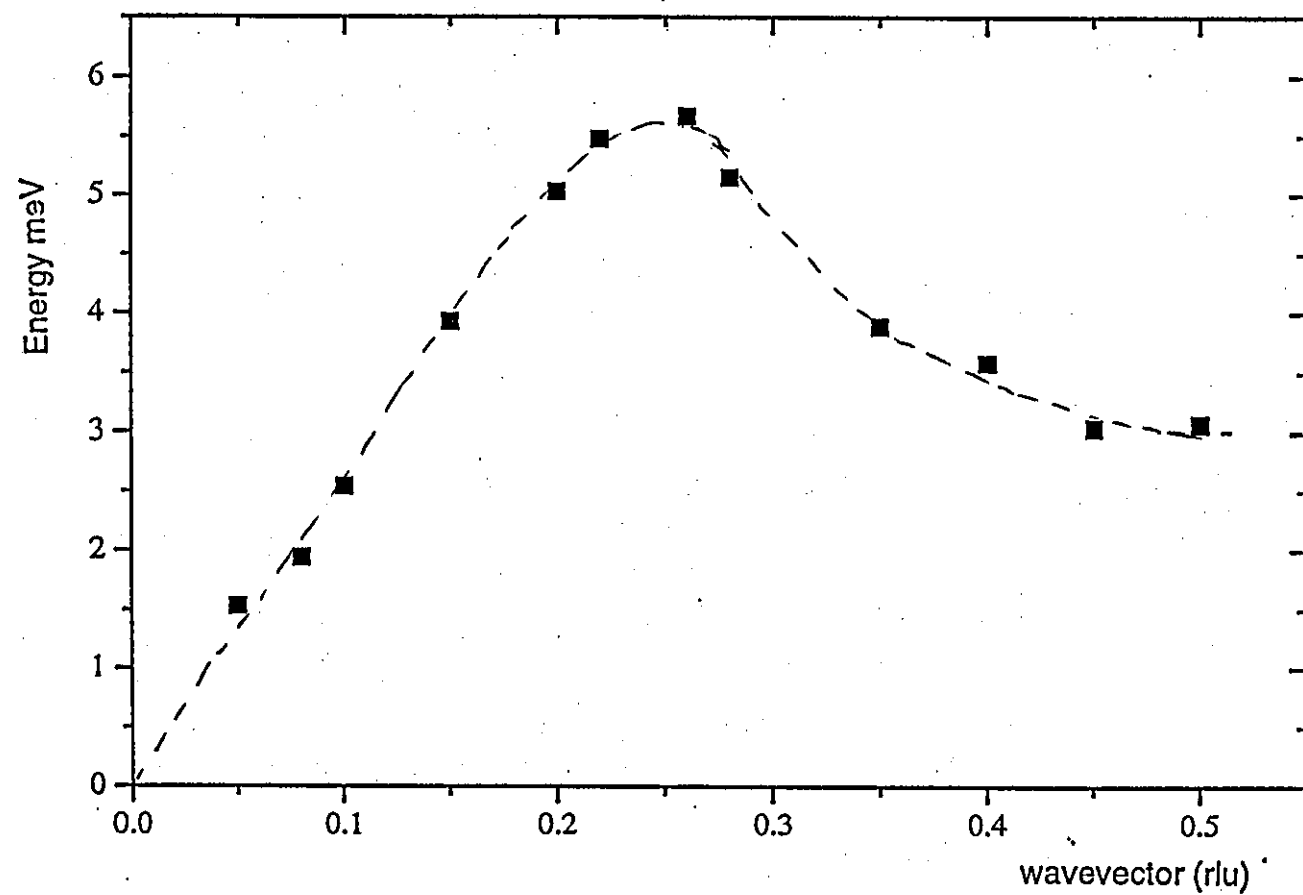


Fig. 5.11: Dispersion curve of LA [110] phonon (line as guide to the eye)

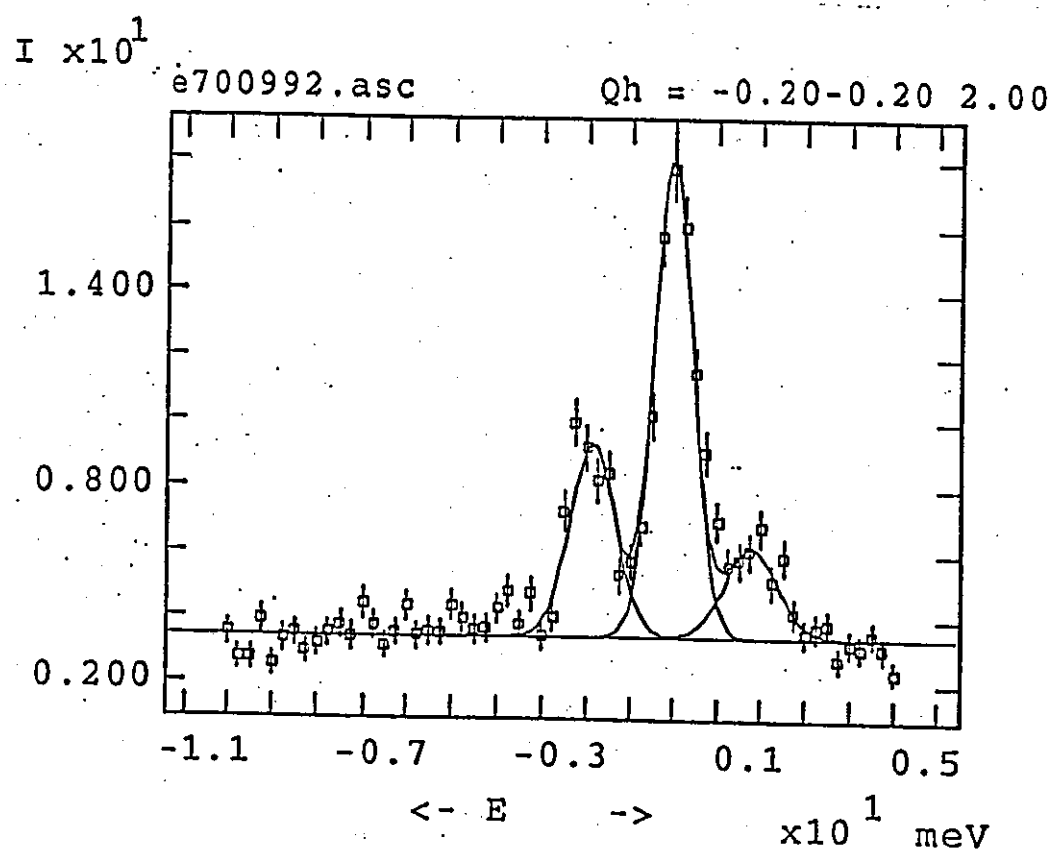
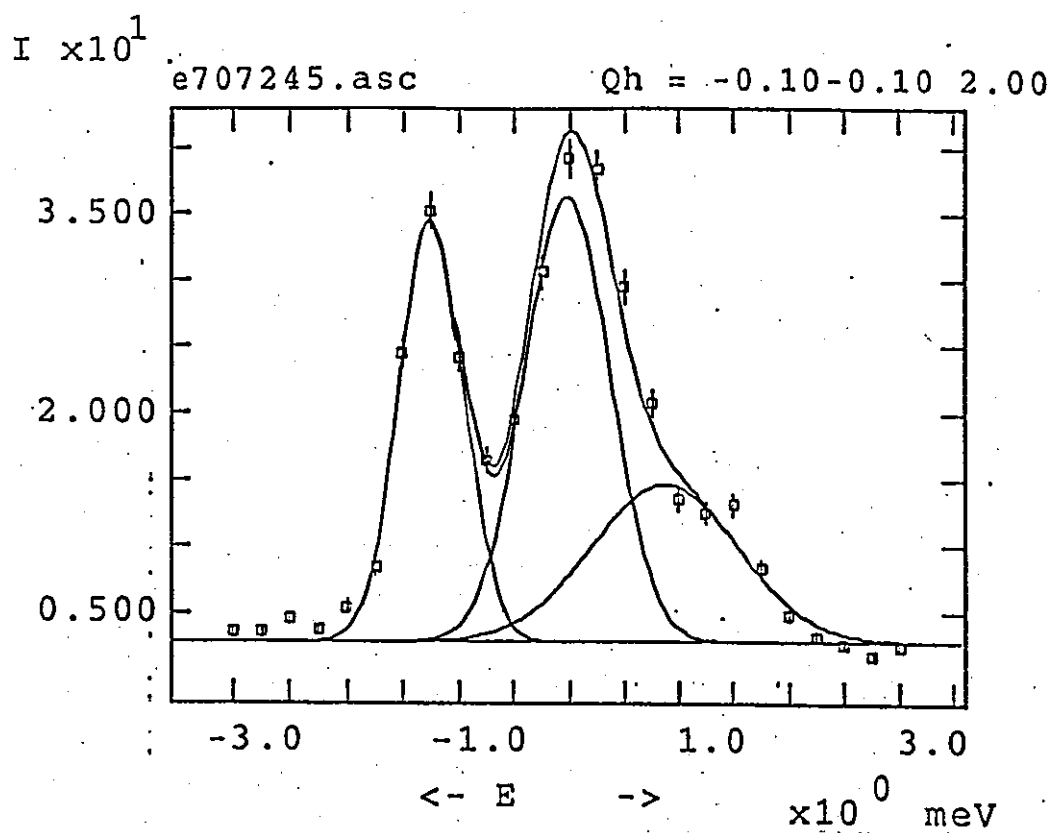


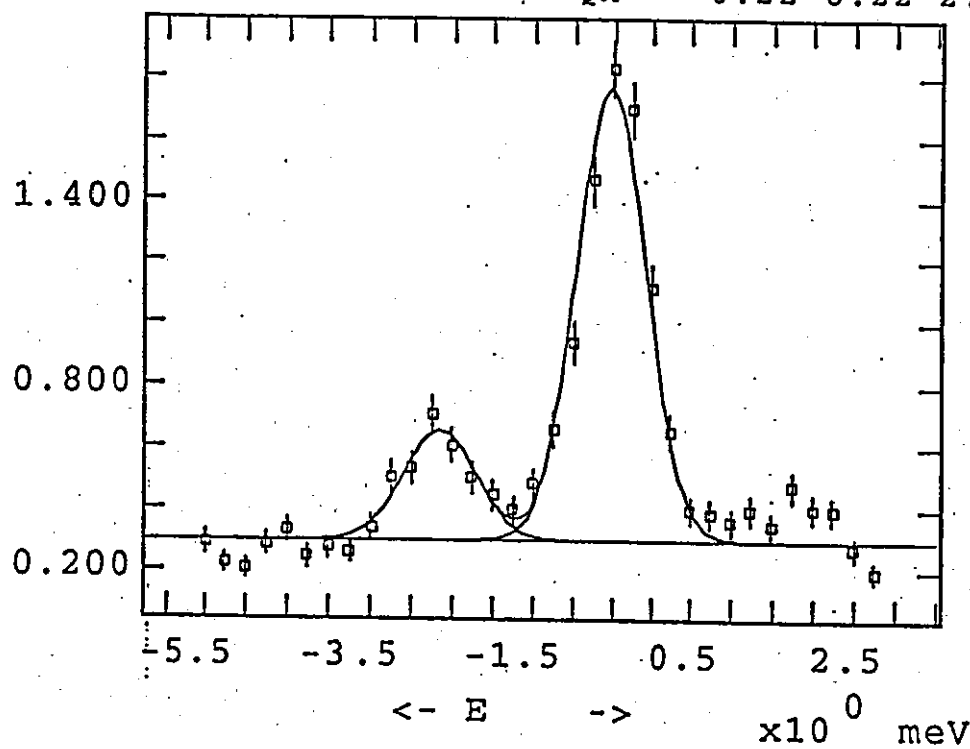
Fig. 5.12: Profiles of scattering Q (0-h 0-h 2,4)

continued

$I \times 10^1$

e707253.asc

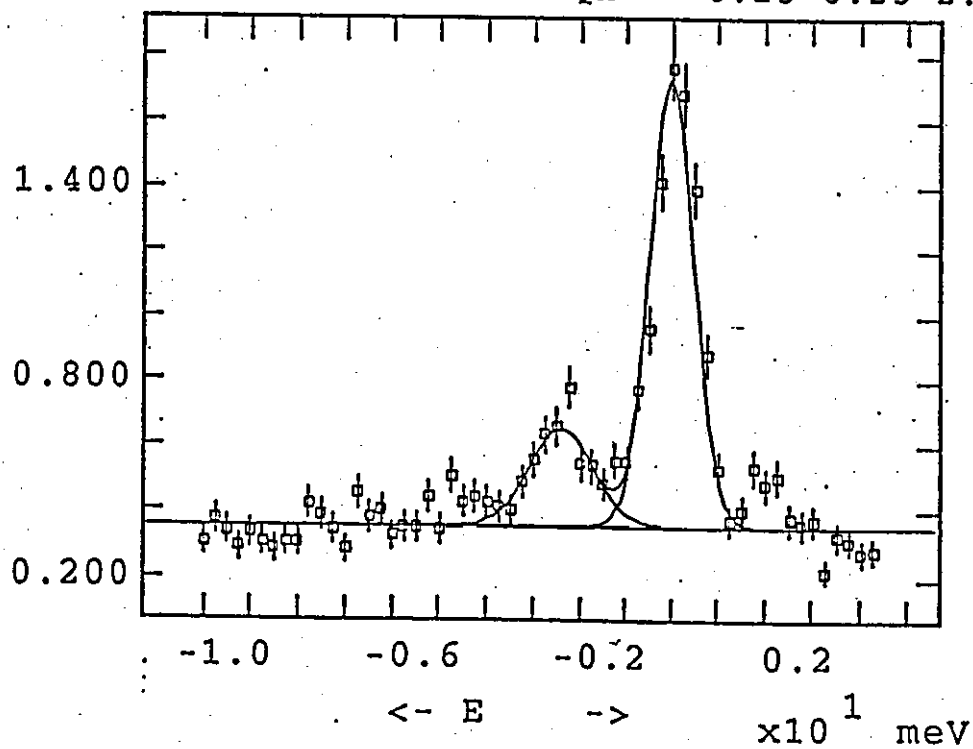
Qh = -0.22-0.22 2.00



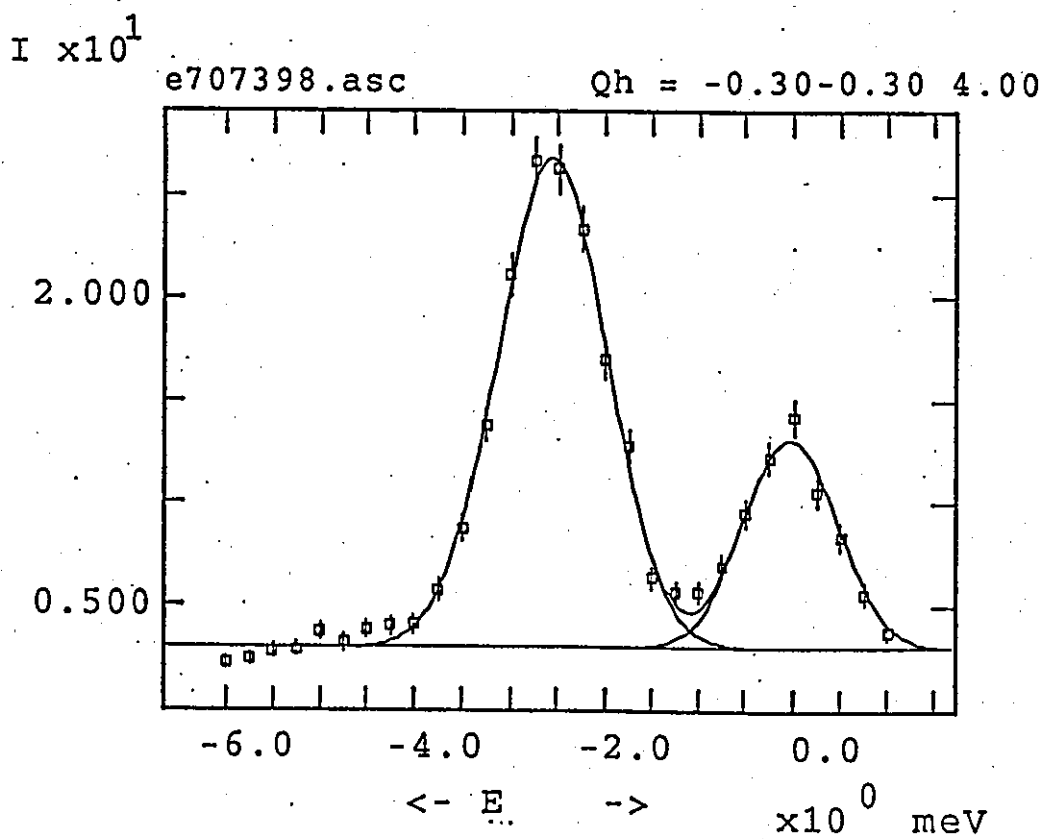
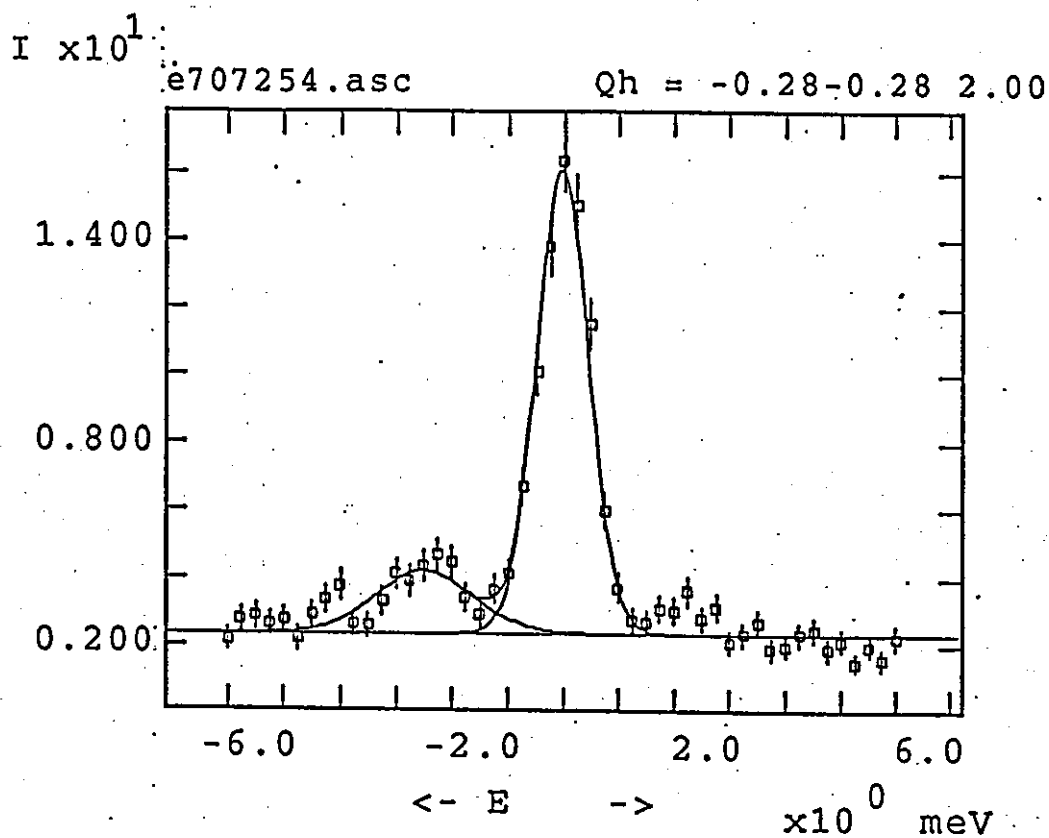
$I \times 10^1$

e700993.asc

Qh = -0.25-0.25 2.00



continued

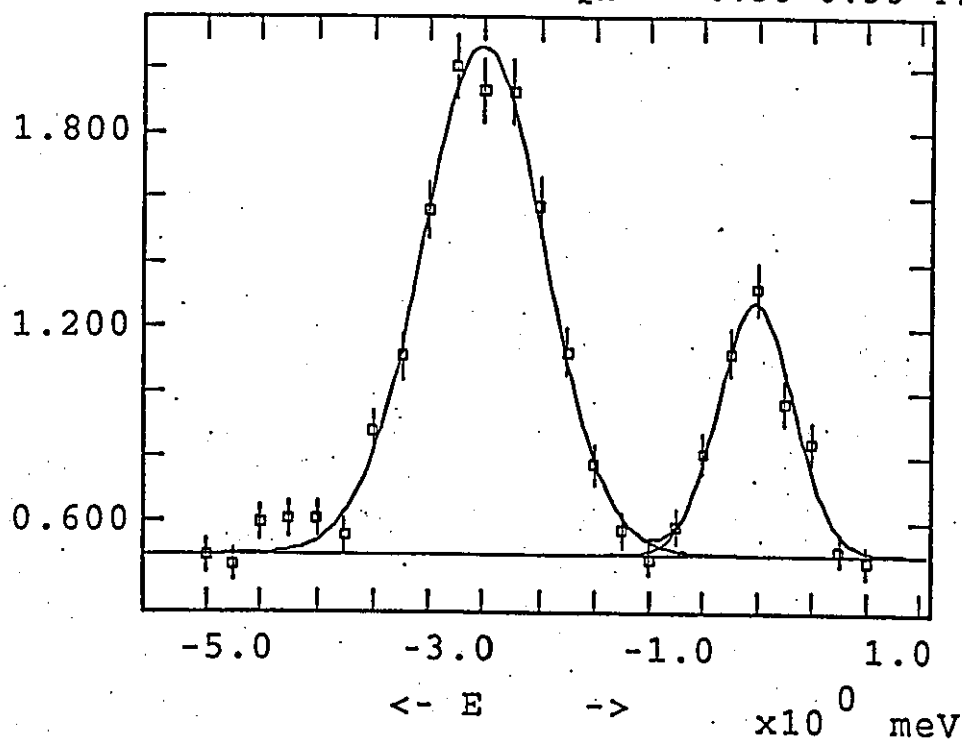


continued

$I \times 10^1$

E707402.ASC

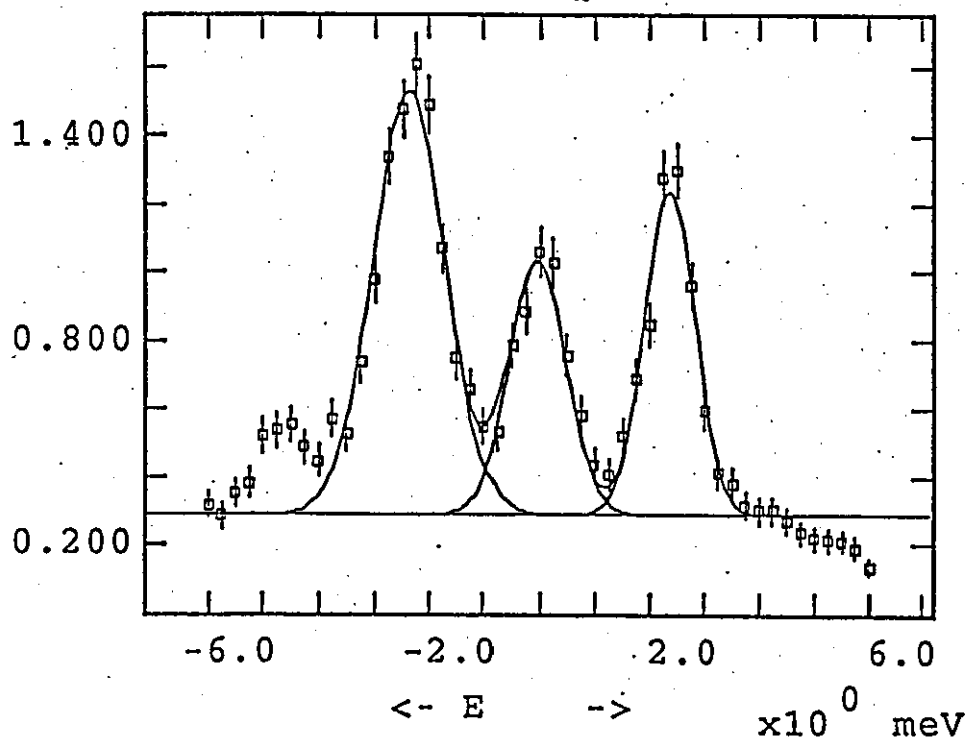
Qh = -0.35-0.35 4.00



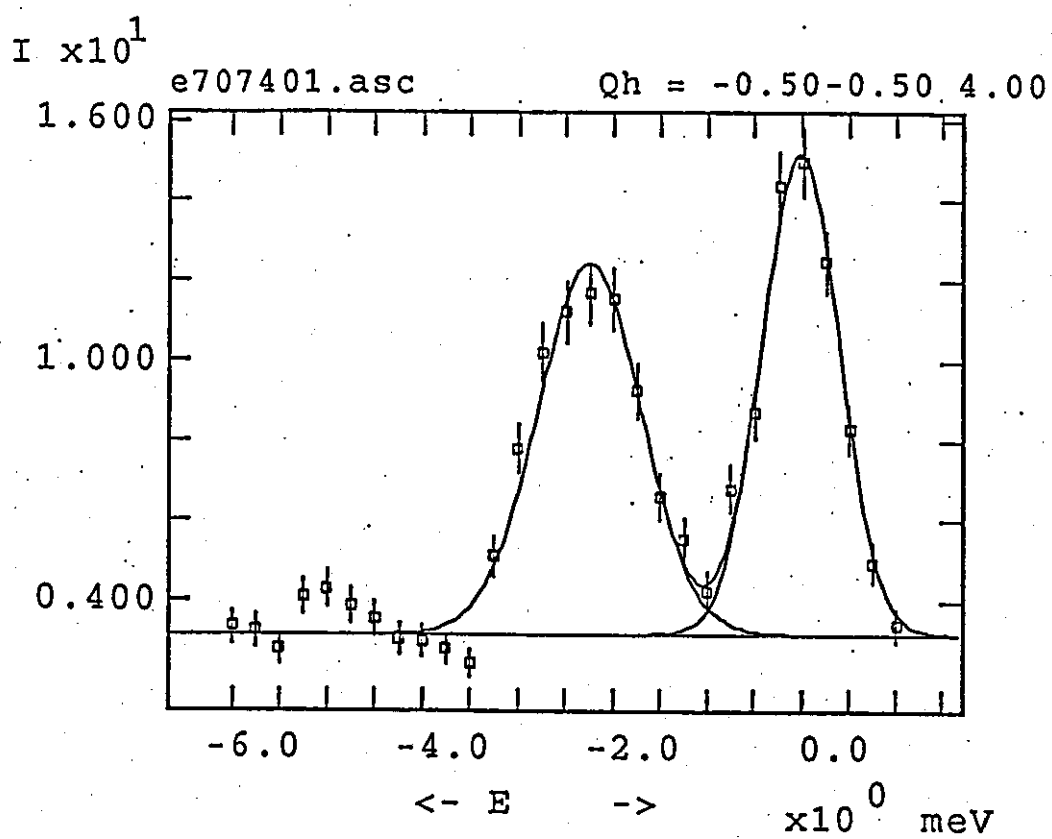
$I \times 10^1$

e707259.asc

Qh = -0.40-0.40 4.00



continued



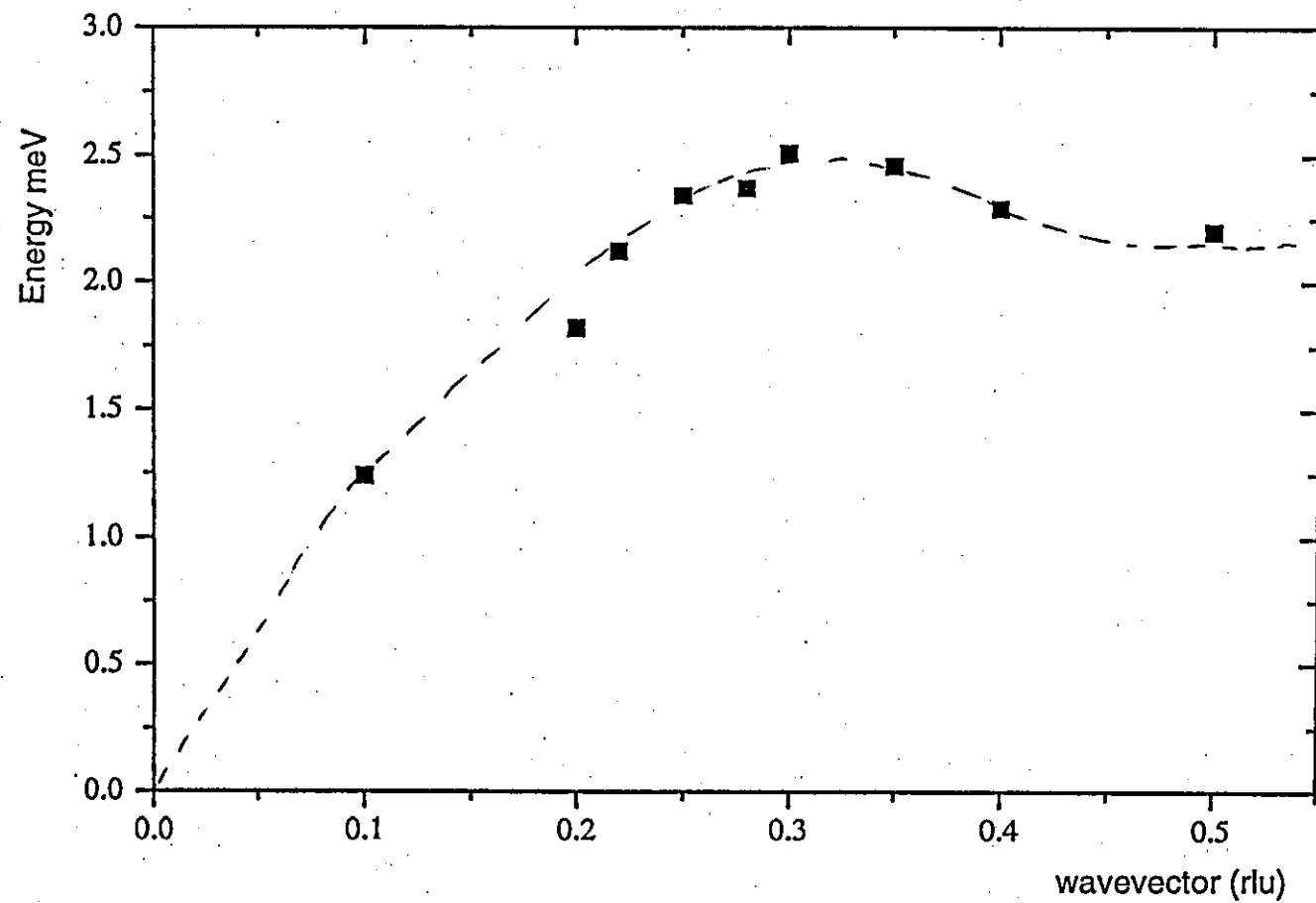


Fig. 5.13: Dispersion curve of TA [110] phonon (line as guide to the eye)

CHAPTER 6

Discussion

The structural phase transitions of TMMC, TMMB and TMMC:Cu have been detected by various techniques such as magnetic susceptibility [Visser 1986], Raman scattering [Mlik & Couzi 1982], ultrasonic measurement [Braud et al 1990] and neutron scattering [Hutchings et. al. 1983] to name a few. In these compounds, the ordering of the TMA molecules takes place at the phase transition (phase I). Many problems are still unresolved; so that a model description of the transition mechanism has not been possible [Couzi & Mlik 1986].

Information (microscopic) from sound wave measurements provide detailed information of the temperature behaviour of the principal elastic constants C_{11} , C_{33} etc. of the lattice. However, the complex continuous change of the parameter in the TMMeX_3 compounds is caused by the complex nature of the TMMeX_3 crystal structure. Therefore, we have carried out Brillouin scattering experiments on ABX_3 hexagonal perovskites, CsNiCl_3 and RbNiCl_3 in order to obtain the temperature dependence of the C_{11} and C_{33} elastic constant of a non distorted ABX_3 system while the full dispersion of the phonons in the hexagonal ABX_3 system CsFeBr_3 was studied by means of inelastic neutron scattering.

Structural phase transitions in TMMC, TMMB and TMMC (8% Cu) were initially investigated by using differential scanning calorimetry (DSC). From our investigations it was confirmed that these compounds undergo structural phase transitions of the first order type at low temperature (phase II) and a second order type at high temperature (phase I').

Numerous cycles of heating and cooling between 171-500K always show distinct anomalies in the DSC curve which is related to the first order transition $\text{I} \leftrightarrow \text{II}$ transitions of TMMC, TMMB, TMMC:Cu and d_{12} -TMMB. In addition to that, we found also another thermal anomaly at I' phase and no hysteresis can be detected and the DSC signal exhibits the characteristics of a second order (or nearly second order) transformation. This phase transition ($\text{I} \leftrightarrow \text{I}'$) stretches itself out over a very large temperature range ($\Delta T \sim 173\text{-}373\text{K}$).

The presence of these phase transitions was further investigated using Brillouin scattering technique. TMMC is the best example of a truly one-dimensional linear chain antiferromagnet in the ABX_3 series. As a result, it has been one of the most extensively studied compounds of the series. All structural modifications of TMMC derive from the parent phase (I') stable at high temperature, with space group $P6_3/mmc$ and $Z=2$ formula units in the primitive unit cell [Braud et. al. 1990]. Another hexagonal phase (I) stable at room temperature, with space group $P6_3/m$ ($Z=2$). Both phases I' and I exhibit orientational disorder of the TMA, of complex nature, coupled to translational disorder of the $MnCl_6$ octahedra chains. These phenomena has been studied in detail in phase I by Braud et. al. [1990].

At low temperatures, ordering processes takes place [Mangum & Utton 1972, Braud et. al. 1990] inducing different ordered phases. In the case of TMMC at zero pressure, a phase transition connects phase I to an ordered phase II with monoclinic symmetry (space group $P2_1/b$ with $Z=4$); phase II is related to phase I by a doubling of the lattice period along the b-axis, perpendicular to the six fold axis [Braud et. al. 1990, Couzi & Mlik 1986].

It has been emphasised by Braud that hexagonal-monoclinic phase transition as observed in TMMC is ferroelastic since they involve a change of the crystalline system; as a result, the monoclinic phase exhibits domain structures as evidenced on the Weissenberg photograph. Thus it is important in such cases to study the behaviour of the elastic constants associated with the strain tensor components that can couple with order parameter of the transition.

This is shown with Brillouin scattering experiments with TMMC, TMMB and TMMC:Cu, showing anomalies in the temperature dependence of C_{11} at the transition temperature. The temperature dependence of C_{11} in the high temperature range is dominated by anharmonic effects due to the thermal expansion of the crystal as have been shown by Braud et. al. [1990], which produces a monotonic (quasi-linear) increase of C_{11} with decreasing temperature.

However, one notices a well defined step-like anomaly of C_{11} at the I'-I transition temperature (see Figures 3.18, 3.20 and 3.21). In phase I, there is a

balance between the thermal expansion effects mentioned by Braud and a softening of C_{11} when the $I \leftrightarrow II$ transition temperature is approached from above, resulting in a maximum value of C_{11} around 200-250K in all three compounds studied.

The temperature dependence of C_{11} has been analysed in detail according to a thermodynamic potential developed in the framework of Landau theory [Braud et. al. 1990]. However, it is possible to explain these data on qualitative grounds - the step like variation of C_{11} at the $I \leftrightarrow II$ transition temperature is characteristic of linear quadratic coupling existing between the strain components and the order parameter [Rehwald 1973].

The phase transition temperatures obtained from our measurement is shown in Table 6.1. Also the reported values of other measurements in the literature are given

Table 6.1 Values of transition temperatures obtain from Brillouin Scattering and DSC

Compound	T_{c1} K			T_{c2} K		
	Brillouin	DSC	Others	Brillouin	DSC	Others
TMMC	129.6	129.2	129.0	388.6	379.0	390.0
TMMB	142.6	144.9	144.0	377.6	383	-
TMMC:Cu	108.6	129.3	92, 124, 130	359.6	383	-
d_{12} -TMMB	-	143.6	-	-	383.0	-

The values of the transitions temperatures obtained from our measurement agrees well with the reported values, except for TMMC:Cu. This might be due to the different percentage of Cu doped or due to the non homogenous doping. The phase transition in TMMB was first reported here using the Brillouin scattering technique as was the higher temperature (phase I') of TMMB and TMMC:Cu.

The activation energies of these compounds at the phase transition ($I \leftrightarrow II$) (Table 4.6) were obtained by three different methods (see Chapter 4) which gave all approximately the same values. When we compare the activation

energies for the same phase transitions at low temperature ($I \leftrightarrow II$) we observed large differences between each individual compound. The difference between the activation energy of TMMC (40.6 kJ/mol), TMMB (51.7 kJ/mol) can be explained by looking at the direct chemical surrounding of the TMA group. The hexagonal packing results in a twinned cuboctahedron (12 co-ordination of Cl, Br ions) in which the TMA group rotates. By comparing the twinned cuboctahedron Cl⁻ or Br⁻ ion, it is obvious that the space provided by the Br ion is much larger, therefore the activation energy which is required to set the TMA group spinning is lower. The potential barrier which has to be overcome in order to set the TMA group spinning in TMMC is larger than in TMMB.

One notices also a substantial difference for the activation energy between the TMMB (hydrogenated) and d_{12} -TMMB (deuterated). This fact may be explained by the fact that the bonding between the TMA group and the Cl layer takes place via the C-H-Cl hydrogen bonding. The main difference in the C-D-Cl bond increases the bond strength and consequently more energy is required.

The Cu doped (TMMC:Cu 8%) has relatively low activation energy and seems on first sight to be anomalous in comparison with the other $TMMeX_3$ compounds. The transition temperature (from Brillouin scattering) of both phases II and I' is very much lower than the pure TMMC. For an explanation one has to look to the chemical nature of the Cu²⁺ ion. Substitution of Cu²⁺ in TMMC, where Cu²⁺ is known to be Jahn Teller active, therefore it has the tendency to distort the surrounding Cl₆ octahedron along one of its three axes. Different amount of doping will produce increased strain fields in the crystals and work finally in a co-operative way to distort the lattice e.g. CsCuCl₃ and TMCuCl [Haije & Maaskant 1988, Willet et. al 1985]. By assuming that there is a coupling between the motions of the TMA molecules and the MnCl₃ chain, Mlik & Couzi [1982] indicates that a commensurate-incommensurate phase transition should occur in TMMC but the balance between competing forces is such that the incommensurate phases become infinitely narrow.

From Brillouin scattering experiments, we were able to calculate the elastic constant of these compounds at room temperature. The elastic constant of CsFeBr₃ was obtained by neutron scattering experiments. The values of the

elastic constant are listed in Table 6.2 with comparison to other reported values.

Table 6.2 Elastic constant of some of the ABX_3 at room temperature

Compound	Mode	$\rho v^2 \times 10^{10} \text{Nm}^{-2}$ (Brillouin)	$\rho v^2 \times 10^{10} \text{Nm}^{-2}$ (reported)	$\rho \text{ kgm}^{-3}$
TMMC	C_{11}	2.1	2.2 [Hutchings et. al. 1983] 2.0 [Levola & Laiho1986]	1661
TMMB	C_{11}	1.59	-	2355
RbNiCl ₃	C_{11}	3.71	-	3371
	C_{33}	5.42	-	
CsNiCl ₃	C_{11}	3.77	3.58 [Mountfield 1981]	3738
	C_{33}	5.62	6.25 [Mountfield 1981]	
CsFeBr ₃	C_{11}	7.33	-	4620
	C_{66}	1.01	-	
	C_{33}	2.58	-	
	C_{44}	0.56	-	

The values obtained agree with the reported values. The elastic constant of RbNiCl₃, CsFeBr₃ and TMMB was first reported here.

The phonon excitations in pseudo one-dimensional antiferromagnets CsFeBr₃ were observed using inelastic neutron scattering techniques. Along the [001] (parallel to the chain axis), a longitudinal acoustic(LA), longitudinal optic (LO) and transverse acoustic (TA) phonons were observed. The LA phonon has a zone boundary energy of ~ 5.5 meV and the LO phonon increases to ~ 9.0 meV at the zone boundary. The TA phonon does not have an energy maximum at the zone boundary. The dispersion curves parallel to the chain axis are as shown in Figure 6.1.

The dispersion curves perpendicular to the chain axis are as shown in Figure 6.2. From the dispersion curve, the LA phonon reach a maximum half way the zone boundary at ~ 6.0 meV which then starts to decrease towards the zone boundary. A TA phonon was also observed with lower energy compared to the LA phonon. The TA phonon has a maximum energy at ~ 2.4 meV which

again starts to decrease towards the zone boundary. From the initial slopes of the dispersion curves, the sound velocity can be deduced which enable us to calculate the elastic constant as shown in Table 6.2.

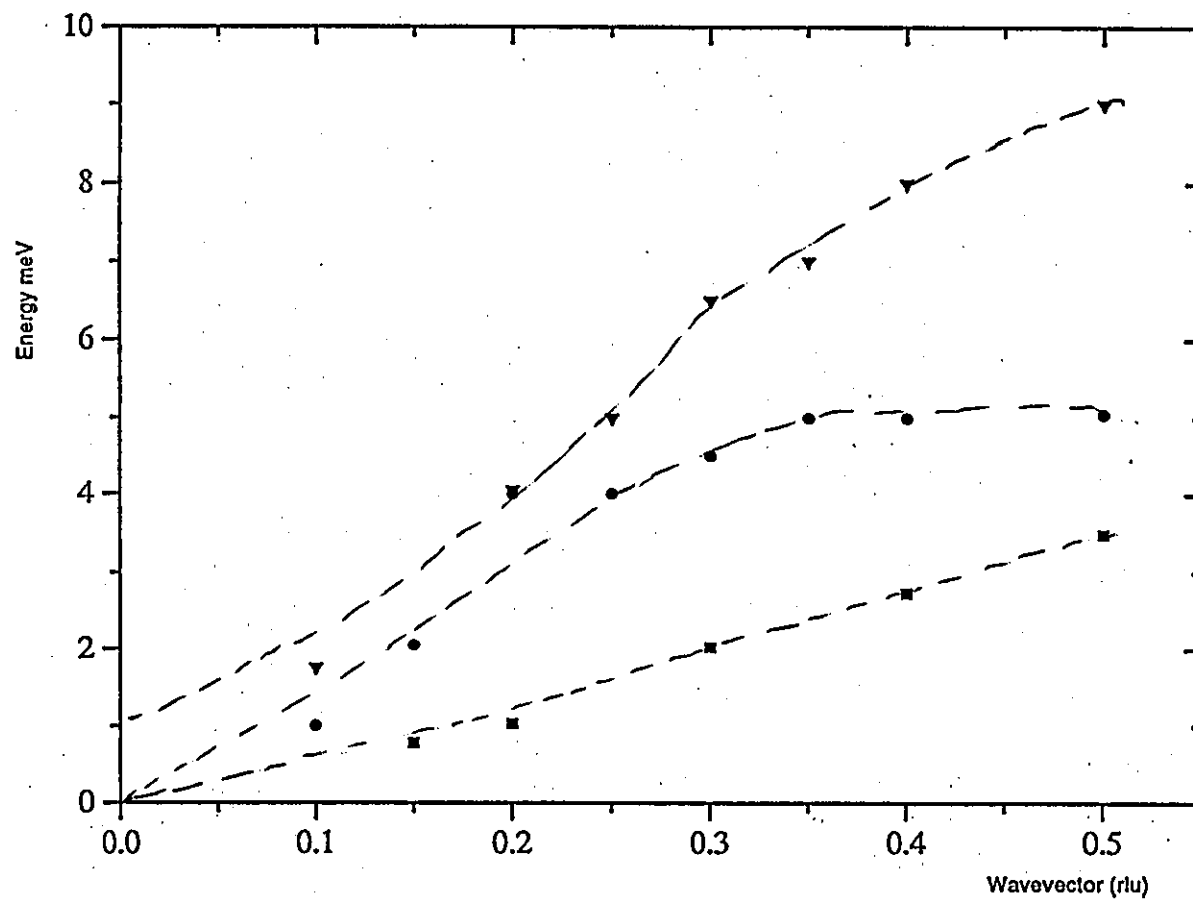


Fig. 6.1 Dispersion curves of phonon excitation parallel to chain direction
(line as guide to the eye)

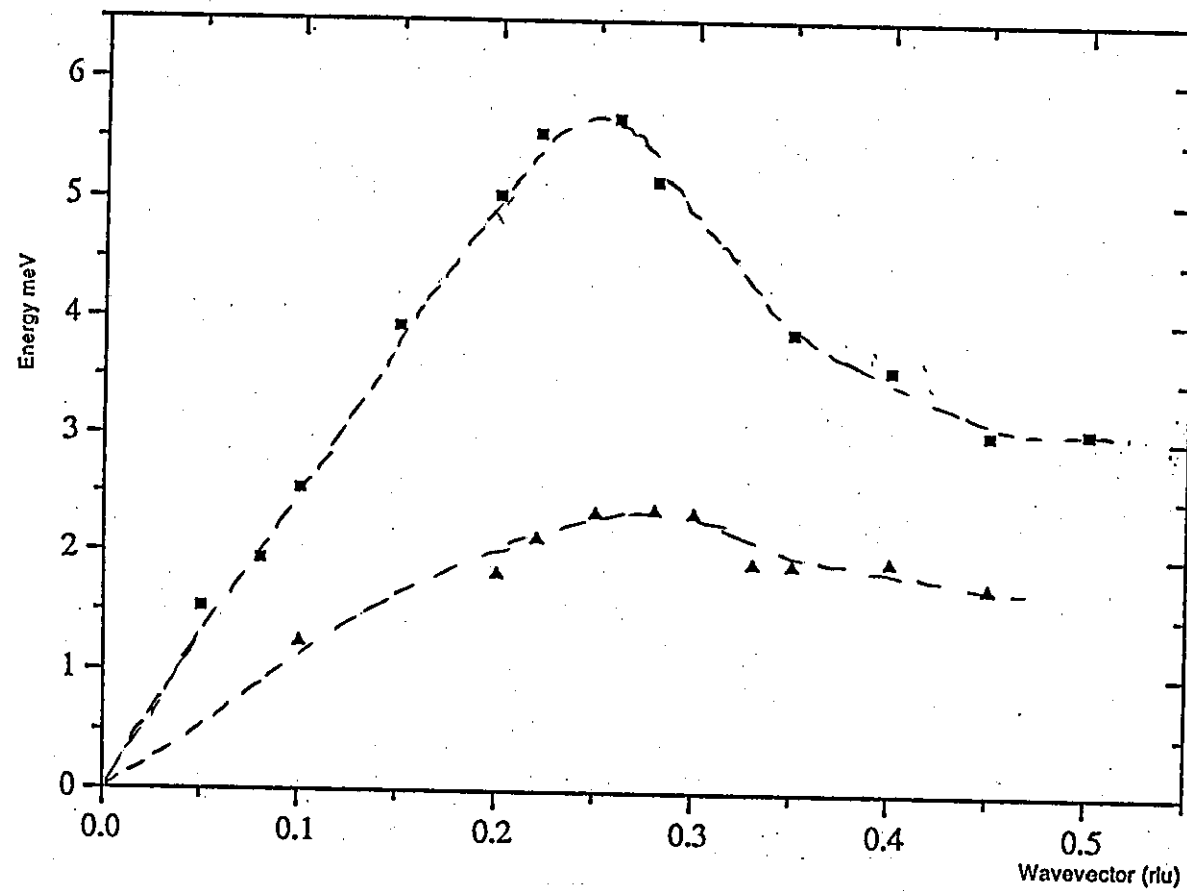


Fig. 6.2 Dispersion curves of phonon excitation perpendicular to chain direction (line as guide to the eye)

Conclusion:

Structural phase transitions in some ABX_3 ternary halides which crystallise with the hexagonal perovskite structure have been investigated. The phase transitions in TMMC, TMMB and TMMC:Cu were observed with the Brillouin scattering technique. Two acoustic anomalies have been found at $(129.6 \pm 1.0K)$, $(388.6 \pm 1.0K)$ (TMMC), $(142.6 \pm 1.0K)$, $(377 \pm 1.0K)$ (TMMB) and $(108.6 \pm 1.0K)$, $(359.6 \pm 1.0K)$ (TMMC:Cu) regarding to the phase transition temperature. These compounds show two types of phase transition that is of a second order phase transition at high temperature which is of a disorder type and a first order phase transition at lower temperature which is of a displacive type as well as order disorder type.

The influence of Cu doping (the introduction of Jahn-Teller active centres), for TMMC have also been investigated. The phase transition is shifted to lower temperature than that of the pure TMMC. The temperature dependence of the elastic constant of these compounds have been determined using the Brillouin scattering technique. The elastic constant of $RbNiCl_3$ and $CsNiCl_3$ which show no structural phase transition have also been determined as a comparison with the $TMMeX_3$ compounds.

The phase transitions of these compounds are also characterised macroscopically by Differential Scanning Calorimetry (DSC), where again two anomalies were observed in the DSC curve, the high temperature transition is of second order and the low temperature transition is of first order. The activation energies at the phase transitions were deduced with DSC measurements as 70.6 (TMMC), 49.2 (TMMC:Cu), 51.7 (TMMB) and 69.9 (d_{12} -TMMB) in kJ/mol. The change from 70.6 kJ/mol to 49.2 kJ/mol when TMMC is doped with Cu is believed to be due to the tendency of the Cu^{2+} ion to distort the surrounding Cl_6 octahedron. Deuteration of TMMB increases the activation energy by about 35%. This is believed to be due to the difference in hydrogen bonding between C-H-Cl and C-D-Cl, the deuterated compound having a greater bond strength.

Inelastic neutron scattering experiments on the hexagonal perovskite $CsFeBr_3$ have been carried out and from the curves of the longitudinal acoustic and transverse acoustic phonons were determined at room

temperature. The elastic constant have been evaluated from the initial slopes of the dispersion curves. The values of the elastic constant determined at room temperature for the compounds studied are as listed in Table 6.2.

REFERENCES

1. Achiwa N (1969) Linear antiferromagnetic chains in hexagonal $ABCl_3$ -type compounds [A:Cs or Rb, B:Cu, Ni, Co or Fe]. *Journal of Physical Society of Japan* **27**, 561.
2. Ackerman JF, Cole GM and Holt SL (1974) The physical properties of some transition metal compounds of the ABX_3 type. *Inorganica Chimica Acta* **8**, 223.
3. Adachi K and Mekata M (1973) Specific heat of antiferromagnetic $CsNiCl_3$. *Journal of Physical Society of Japan* **34**, 269.
4. Adachi K, Takeda K, Matsubara F, Mekata M and Haseda T (1983) Magnetic ordering in a partially frustrated triangular antiferromagnet $RbFeBr_3$. *Journal of Physical Society of Japan* **54**, 2202.
5. Affleck I (1989) Quantum spin chains and the Haldane gap. *Journal of Physics: Condensed Matter* **1**, 3047.
6. Alcock NW and Holt SL (1978) TMMB at 235K and 115K. *Acta Crystallography* **B34**, 1970.
7. Augis JA and Bennett JE (1978) Calculation of the Avrami parameters for heterogeneous solid state reactions using a modification of the Kissinger method. *Journal of Thermal Analysis* **13**, 283.
8. Berg RW and Skaarup S (1978) Low temperature for IR spectra of $(CH_3)_4NNiCl_3$, $(CH_3)_4NNiBr_3$ and $(CD_3)_4NNiBr_3$. *Journal of Physics and Chemistry Solids* **39**, 1193.
9. Belitto C, Dessy G, Fares V, Fiorani D and Viticolis S (1984) *Journal of Physics and Chemistry Solids* **54**, 1129.

10. Borovnik-Romanov AS and Kreines NM (1982) Brillouin-Mandelstam scattering from thermal and excited magnons. *Physics Report (Review section of Physics Letters)* **81**, 351.
11. Braud MN, Couzi M, Chanh NB, Courseille C, Gallois B, Hauw C and Meresse A (1990) Lattice dynamics and structural phase transitions in the chain compounds TMMC and TMCC:I. Structural study. *Journal of Physics: Condensed Matter* **2**, 8209.
12. Braud MN, Couzi M, Chanh NB and Gomez-Cuevas A (1990) Lattice dynamics and structural phase transitions in the chain compounds TMMC and TMCC:II. Raman scattering and ultrasonic measurements. *Journal of Physics: Condensed Matter* **2**, 8229.
13. Braud MN, Couzi M and Chanh NB (1990) Lattice dynamics and structural phase transitions in the chain compounds TMMC and TMCC:III. Landau theory. *Journal of Physics: Condensed Matter* **2**, 8243.
14. Catlow CRA, Comins JD, Germano FA, Hartley RT and Hayes W (1978) Brillouin scattering and theoretical studies of high temperature disorder in fluorite crystals. *Journal of Physics C: Solid State Physics* **11**, 3197.
15. Chandrasekharan V (1951) Thermal scattering of light in crystal. *Proceeding in Indian Academy Science Section* **A33**, 183.
16. Clark RH and Moulton WG (1971) ^{133}Cs and ^{35}Cl NMR in anti ferromagnetic CsNiCl_3 . *Physical Review* **B5**, 788.
17. Clement S, Dupas C and Renard JP (1982) Electron spin resonance in heavily doped TMMC:Cu. *Journal Physique* **43**, 767.
18. Cochran W (1959) Crystal stability and the theory of ferroelectricity. *Physical Review Letters* **3**, 412.
19. Collocott SJ and Rayne JA (1987) Low temperature heat capacity of linear chain magnetic compounds CsNiCl_3 . *Journal of Applied Physics* **61**, 4404.

20. Couzi M and Mlik Y (1986) Raman scattering study of the pressure and temperature-induced phase transitions in the chain compound $(\text{CH}_3)_4\text{NMnCl}_3$ and $(\text{CH}_3)_4\text{NCdCl}_3$. *Journal of Raman Spectroscopy* **17**, 117.
21. Cowley RA, Buyers WJL and Dolling G (1979) Relationship of normal modes of vibration of Strontium titanate and its antiferroelectric phase transition at 110K. *Solid State Communication* **7**, 181.
22. Cottam MG and Lockwood DJ (1986) Light scattering in magnetic solids. John-Wiley & Sons.
23. Dorner B (1972) The normalisation of the resolution function for inelastic neutron scattering and its application. *Acta Crystallography* **28**, 319.
24. Dorner B, Visser D, Steigenberger U, Kakurai K and Steiner M (1988) Magnetic excitations in the quasi one-dimensional antiferromagnet singlet ground state system CsFeBr_3 . *Zeitschrift fur Physik* **B72**, 487.
25. Dorner B, Visser D and Steiner M (1990) Magnetic excitations and phase transitions of CsFeBr_3 in an extended magnetic field. *Zeitschrift fur Physik* **B81**, 75.
26. Dunn AG, Jewess M, Staveley LAK and Worswick RD (1983) Heat capacity of TMMC from 1.5-300K. *Journal of Chemical Thermodynamics* **15**, 351.
27. Durvasula LN and Gammon RW (1978) Pressure scanned three pass Fabry-Perot interferometer. *Journal of Applied Optics* **17**, 3298.
28. Ganot F, Dugautier C, Moch P and Nouet J (1982) Brillouin scattering and ultrasonic propagation in the nearly cubic antiferromagnet KNiF_3 . *Journal of Applied Physics* **52**, 801.

29. Haije WG and Maaskant WJA (1988) Structural resonance harmonic and anharmonic interactions: the characterisation of local and overall chirality in TMACuCl_3 . *Journal of Physics C: Solid State Physics* **21**, 5332.
30. Harada J (1970) X-ray and neutron diffraction study of tetragonal Barium Titanate. *Acta Crystallography* **A26**, 336.
31. Harrison A, Stager CV and Visser D (1991) ND_4FeBr_3 one dimensional $S=1$ antiferromagnet. *Journal of Applied Physics* **69**, 5998.
32. Harrison A and Visser D (1992) A dynamical correlated effective field treatment of the magnetic excitations in the singlet ground state antiferromagnet RbFeBr_3 . *Journal of Physics: Condensed Matter* **4**, 6977.
33. Hatfield WE, Estes WE, Marsh WE, Pickens MW, ter Haar LW and Weller RR (1983) Extended linear chain compounds 3, ed. Miller JS (New York:Plenum).
34. Hoshino S and Montegi (1974) X-ray study on the phase transition of NaNO_2 . *Japan Journal of Applied Physics* **6**, 708.
35. Hutchings MT, Birgeneau RJ, Holt SL and Shirane G (1972) Spin dynamics in the one-dimensional antiferromagnet $(\text{CD}_3)_4\text{NMnCl}_3$. *Physical Review* **B5**, 1999.
36. Hutchings MT, Pawley GS and Stirling WG (1983) A neutron scattering investigation of some aspects of the structural phase transition in $(\text{CD}_3)_4\text{NMnCl}_3$ (TMMC). *Journal of Physics C: Solid State Physics* **16**, 115.
37. Iio K, Hyodo H and Nagata K (1980) Observations of short range order by optical birefringence in one dimensional antiferromagnets CsNiCl_3 , RbNiCl_3 and CsCoCl_3 . *Journal of Physical Society of Japan* **49**, 1336.

38. Janzen Y (1989) Report submitted to Physics Department, Loughborough University of Technology.
39. Jenkins FA and White HE (1957) Fundamentals of optics, McGraw Hill.
40. Johnson PB, Rayne JA and Friedberg SA (1979) Magnetic properties of CsNiCl_3 and RbNiCl_3 . *Journal of Applied Physics* **50**, 1853.
41. Kadowaki H, Ubukoshi K and Hirakawa K (1987) Neutron scattering study of successive phase transitions in triangular lattice antiferromagnet CsNiCl_3 . *Journal of Physical Society of Japan* **56**, 751.
42. Kakurai K, Steiner M, Regnault LP and Renard JP(1990) Inelastic neutron scattering at quasi 1-D ferromagnet TMNB. *Solid State Communication* **74**, 165.
43. Kissinger HE (1957) Reaction kinetics in differential thermal analysis. *Journal of Analytical Chemistry* **29**, 1702.
44. Kittel C (1953) Introduction to solid state physics. John-Wiley, New York.
45. Knop W, Steiner M and Day P (1983) Magnetic field induced incommensurate magnetic phases in the singlet ground state system CsFeCl_3 . *Journal of Magnetism and Magnetic Materials* **31-34**, 1033.
46. Laiho R, Natarajan M and Kaira M (1973) Some electrical and optical studies in CsCuCl_3 crystals. *Journal of Physics: Status Solidi* **15**, 311.
47. Landau LD and Lifshitz EM (1959) Statistical Physics. Pergamon:London.

48. Levola T and Laiho R (1986) Brillouin scattering investigation of structural phase transitions in TMMC and TMMC:Cu. *Journal of Physics C: Solid State Physics* **19**, 693.
49. Levola T and Laiho R (1988) Investigations of structural phase transitions of $(\text{CH}_3)_4\text{NCdCl}_3$ by Brillouin scattering. *Solid State Communication* **66**, 557.
50. Lindsay SM, Burgess S and Shephard IW (1977) Correction of Brillouin linewidths measured by multipass Fabry-Perot spectroscopy. *Applied Optics* **16**, 1404.
51. Maegawa S, Goto T and Ajiro Y (1988) ^{133}Cs NMR study of magnetic ordered phases in triangular lattice antiferromagnets CsNiCl_3 . *Journal of Physical Society of Japan* **57**, 1402.
52. Mangum BW and Uton DB (1972) Low temperature transitions in tetramethylammonium manganese chloride. *Physical Review* **B6**, 2790.
53. Matsubara F (1982) Magnetic ordering in a hexagonal antiferromagnet. *Journal of Physical Society of Japan* **51**, 2424.
54. May W, Kieft H, Couter MJ and Stegeman GJ (1978) Automated data acquisition and stabilization system of Fabry-Perot interferometry. *Journal of Applied Optics* **19**, 1603.
55. Mekata M and Adachi K (1978) Magnetic structures of CsCoCl_3 . *Journal of Physical Society of Japan* **44**, 806.
56. Mlik Y, Daoud A and Couzi M (1979) Raman spectra and structural phase transition in chain compound $(\text{CH}_3)_4\text{NMnCl}_3$ and $(\text{CH}_3)_4\text{NCdCl}_3$. *Physics Status Solidi (a)* **52**, 175.
57. Mlik Y and Couzi M (1982) On the structures of the low temperature phases of $(\text{CH}_3)_4\text{NMnCl}_3$ and $(\text{CH}_3)_4\text{NCdCl}_3$: a Raman scattering group theoretical study. *Journal of Physics C: Solid State Physics* **15**, 6591.

58. Mock R, Hillebrands B and Sandercock JR (1987) Construction and performance of a Brillouin scattering set-up using a tripel pass tandem Fabry-Perot interferometer. *Journal of Physics E: Science Instrumentation* **20**, 656.
59. Morosin B and Graeber EJ (1967) Crystal structure of tetramethylammonium manganese (II) chloride. *Acta Crystallography* **23**, 766.
60. Mountfield KR and Rayne JA (1981) Elastic moduli of linear antiferromagnet CsNiCl_3 . *Journal de Physique (Colloque)* **C6**, 468.
61. Nye JF (1957) Physical properties of crystals. Oxford Press.
62. Oohara Y, Kadowaki H and Iio K (1991) Neutron scattering study of magnetic successive phase transitions in RbNiCl_3 . *Journal of Physical Society of Japan* **60**, 393.
63. Peercy PS, Morosin B and Samara GA (1973) Phase transitions in $(\text{CH}_3)_4\text{NMnCl}_3$ (TMMC) and related compounds. *Physical Review* **B8**, 3378.
64. Rayne JA, Collins JG and White GK (1981) Low temperature thermal expansion of CsNiCl_3 and RbNiCl_3 . *Journal of Applied Physics* **52**, 1977.
65. Rehwald W (1973) The study of structural phase transitions by means of ultrasonic experiment. *Advances in Physics* **22**, 721.
66. Renard JP, Clement S and Verdauger M (1987) Recent progress in experimental one -dimensional magnetism. *Proc. Ind. Acad. Sci. (Chem. Sci.)* **98**, 131.
67. Richards PM (1974) Electron spin resonance (ESR) in the impurity doped Heisenberg linear chain $(\text{CH}_3)_4\text{NMnCl}_3\text{:Cu}$. *Physical Review* **B10**, 805.

68. Sakurai J, Cowley RA and Doling G (1970) Crystal dynamics and ferroelectric phase transitions of sodium nitrate. *Journal of Physical Society of Japan* **28**, 1426.
69. Sandercock JR (1971) The design and use of a stabilised multipassed interferometer of high contrast ratio. *Proceeding in International Conference Light scattering in Solids, Paris* **9**.
70. Sandercock JR (1975) Some recent developments in Brillouin scattering. *RCA Review* **36**, 89.
71. Sandercock JR (1976) Simple stabilisation scheme for maintenance of mirror alignment in a scanning Fabry-Perot interferometer. *Journal of Physics E: Scientific Instruments* **9**, 566.
72. Sandercock JR and Wettling W (1979) Light scattering from surface and bulk thermal magnons in iron and nickel. *Journal of Applied Physics* **50**, 7784.
73. Sandercock JR (1980) Light scattering from thermally excited surface phonons and magnons. *Proceedings in 7th International Conference on Raman spectroscopy*. Ed. Murphy WF Amsterdam:North Holland, 364.
74. Schmid R, Dörner B, Visser D and Steiner M (1992) Temperature and magnetic field dependent correlation in the singlet ground state system CsFeBr_3 . *Zeitschrift für Physik* **B86**, 257.
75. Schmid R, Dörner B, Visser D and Steiner M (1992) Magnetic field and temperature dependent correlation in the singlet ground state system CsFeBr_3 . *Journal of Magnetism and Magnetic Materials* **104-107**, 771.
76. Scott JF (1974) Soft mode spectroscopy: Experimental studies of structural phase transitions. *Review in Modern Physics* **46**, 83.
77. Sestak J, Satava V and Wendlandt WW (1973) Study of kinetics under non-isothermal conditions. *Thermochimica Acta* **7**, 447.

78. Shirane G (1974) Neutron scattering studies of structural phase transitions at Brookhaven. *Review in Modern Physics* **46**, 437.
79. Steiner M, Villain J and Windsor CG (1976) Theoretical and experimental studies on one-dimensional magnetic systems. *Advances in Physics* **25**, 87.
80. Steiner M, Kakurai K, Knop W, Dörner B, Pynn R, Happek U, Day P and Mclellan G (1981) Collective excitations in the 1-D antiferromagnet CsFeCl_3 with singlet ground state. *Solid State Communications* **38**, 1179.
81. Stucky GD (1968) The crystal structure of $(\text{CH}_3)_4\text{NNiCl}_3$. *Acta Crystallography* **24**, 330.
82. Tanaka H, Dachs H, Iio K and Nagata K (1986) Structural phase transitions in hexagonal ABCl_3 Jahn-Teller crystals I: Face sharing coupling and ground state configuration. *Journal Physics C: Solid State Physics* **19**, 4861.
83. Tsang T and Utton DB (1976) Proton magnetic relaxation and internal relations in TMCC. *Journal of Chemical Physics* **64**, 3780.
84. Unoki H and Sakudo T (1967) Electron spin resonance of Fe^{3+} in SrTiO_3 with special reference to the 110K phase transition. *Journal of Physical Society of Japan* **23**, 546.
85. Vacher R and Boyer L (1972) Brillouin scattering: A tool for the measurement of elastic and photo elastic constant. *Physical Review* **B6**, 639.
86. Visser D (1985) Unpublished results.
87. Visser D (1986) The observation of structural phase transition in AMX_3 linear chain compounds by means of magnetic susceptibility. *Journal of Magnetism and Magnetic Materials* **54-57**, 1489.

88. Visser D and Harrison A (1988) Magnetic structural correlation in the quasi one-dimensional induced moment magnets AFeX_3 . *Journal Physique Colloquium* **C8**, 1467.
89. Visser D, McIntyre GJ, Haije WG and Maaskant WJA (1989) On the low temperature structural phase transitions in $(\text{CH}_3)_4\text{NCuCl}_3$. *Physica* **B156-157**, 254.
90. Visser D, Dorner B and Steiner M (1991) Magnetic excitations of the singlet ground state antiferromagnet CsFeBr_3 in a magnetic field. *Physica* **B174**, 25.
91. Wada N, Ubukashi K and Hirakawa K (1982) Incommensurate magnetic phase transitions in the triangular XY-like antiferromagnet RbFeCl_3 . *Journal of Physical Society of Japan* **51**, 2835.
92. Weenk JW and Spek AL (1976) Tetramethylammonium trichlorocuprate $\text{C}_4\text{H}_{12}\text{Cl}_3\text{CuN}$. *Crystal Structure Communication* **5**, 805.
93. Wettling W, Cottam MG and Sandercock JR (1975) The relation between one-magnon light scattering and the complex magneto-optic effects in YIG. *Journal Physics C: Solid State Physics* **8**, 211.
94. Willet RD, Bond MR and Haije WG (1988) Crystal structure of three phases of tetramethylammonium trichlorocuprate (II) (TMCuCl_3). *Inorganic Chemistry* **27**, 614.
95. Yelon WB and Cox DE (1972) Magnetic ordering in RbNiCl_3 . *Physical Review* **B6**, 204.
96. Yelon WB and Cox DE (1973) Magnetic transitions in CsNiCl_3 . *Physical Review* **B7**, 2024.
97. Yoshizawa H, Kozukue W and Hirakawa K (1980) Neutron scattering study of magnetic excitations in pseudo one-dimensional singlet ground state ferromagnets CsFeCl_3 and RbFeCl_3 . *Journal of Physical Society of Japan* **49**, 144

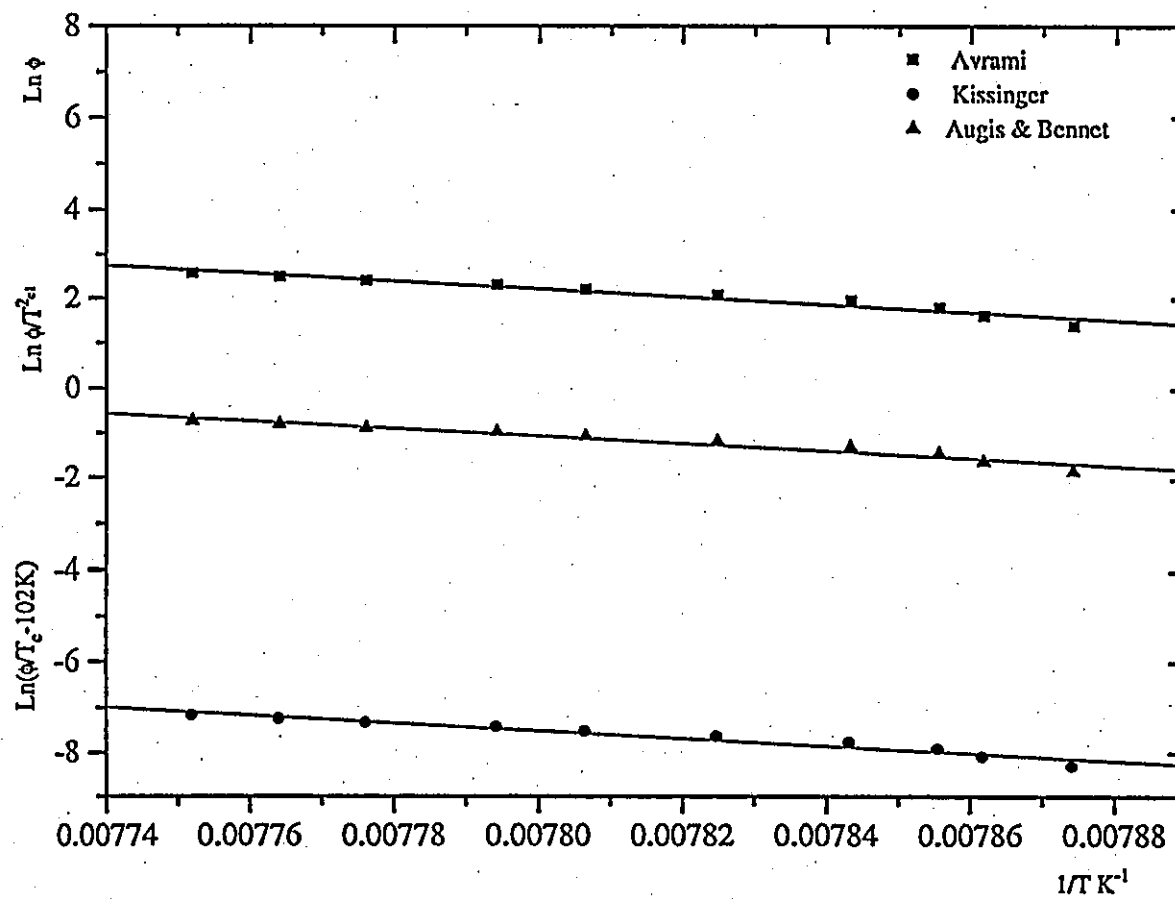


Fig. 4.11 Determination of activation energy E using Avrami, Kissinger and Augis&Bennet method for TMMC

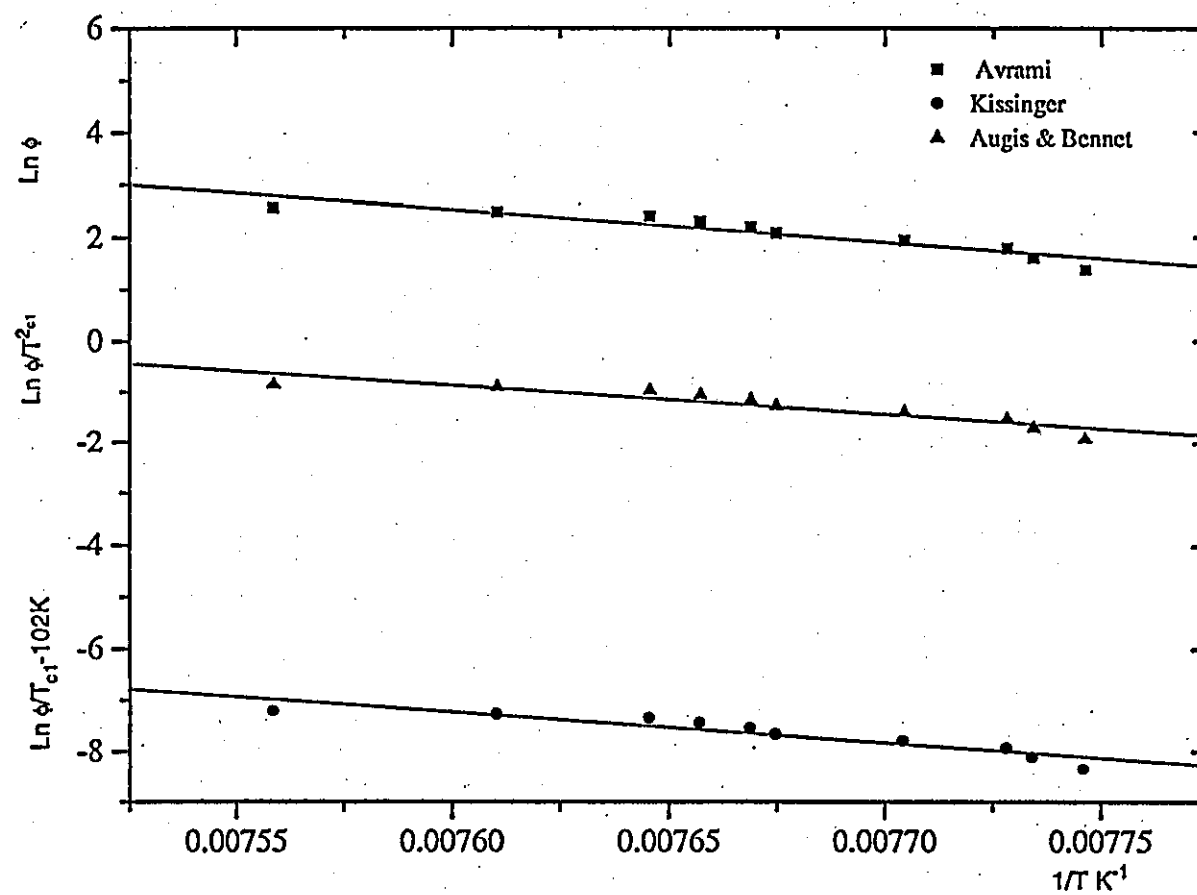


Fig. 4.12 Determination of activation energy E using Avrami, Kissinger and Augis & Bennet method for TMMC:Cu

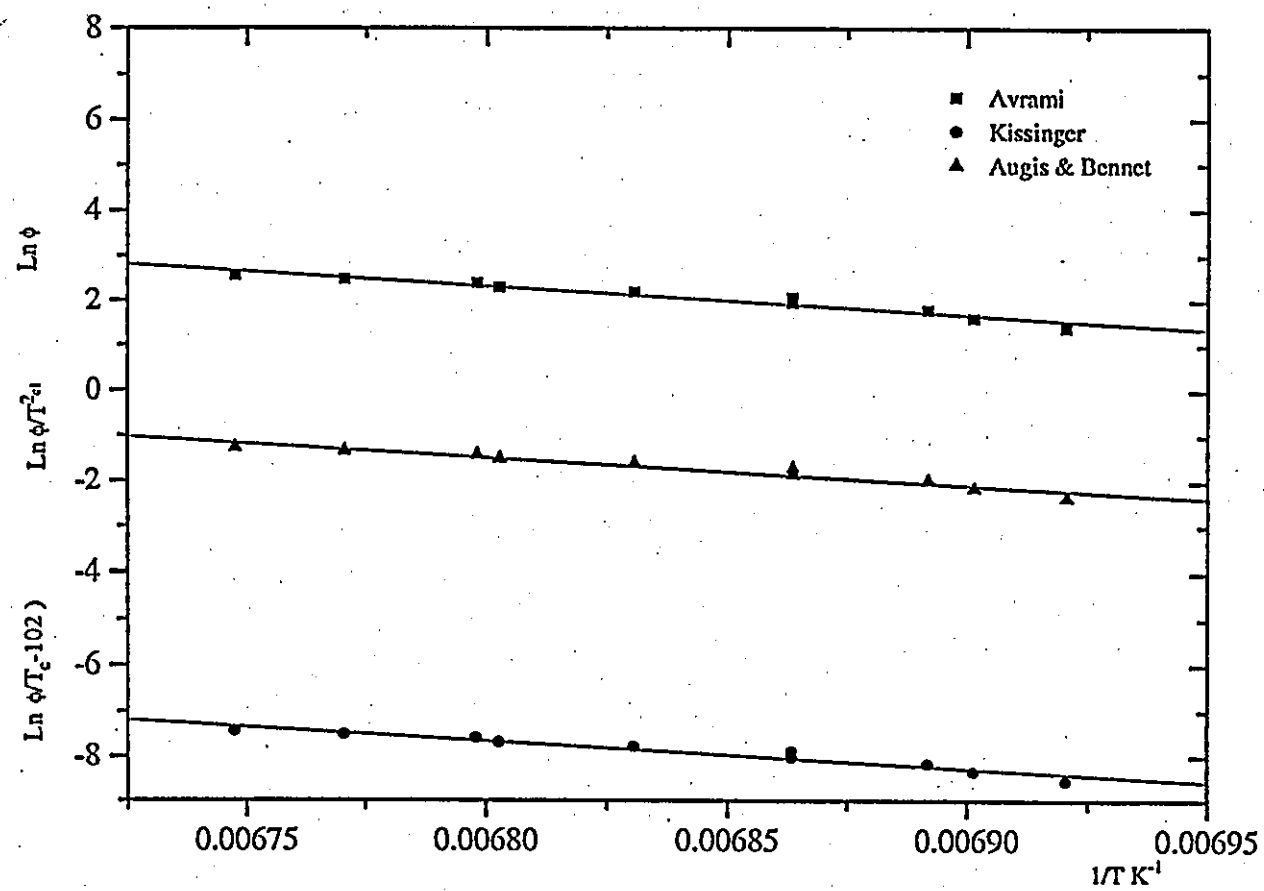


Fig. 4.13 Determination of activation energy E using Avrami, Kissinger and Augis & Bennet method for TMMB

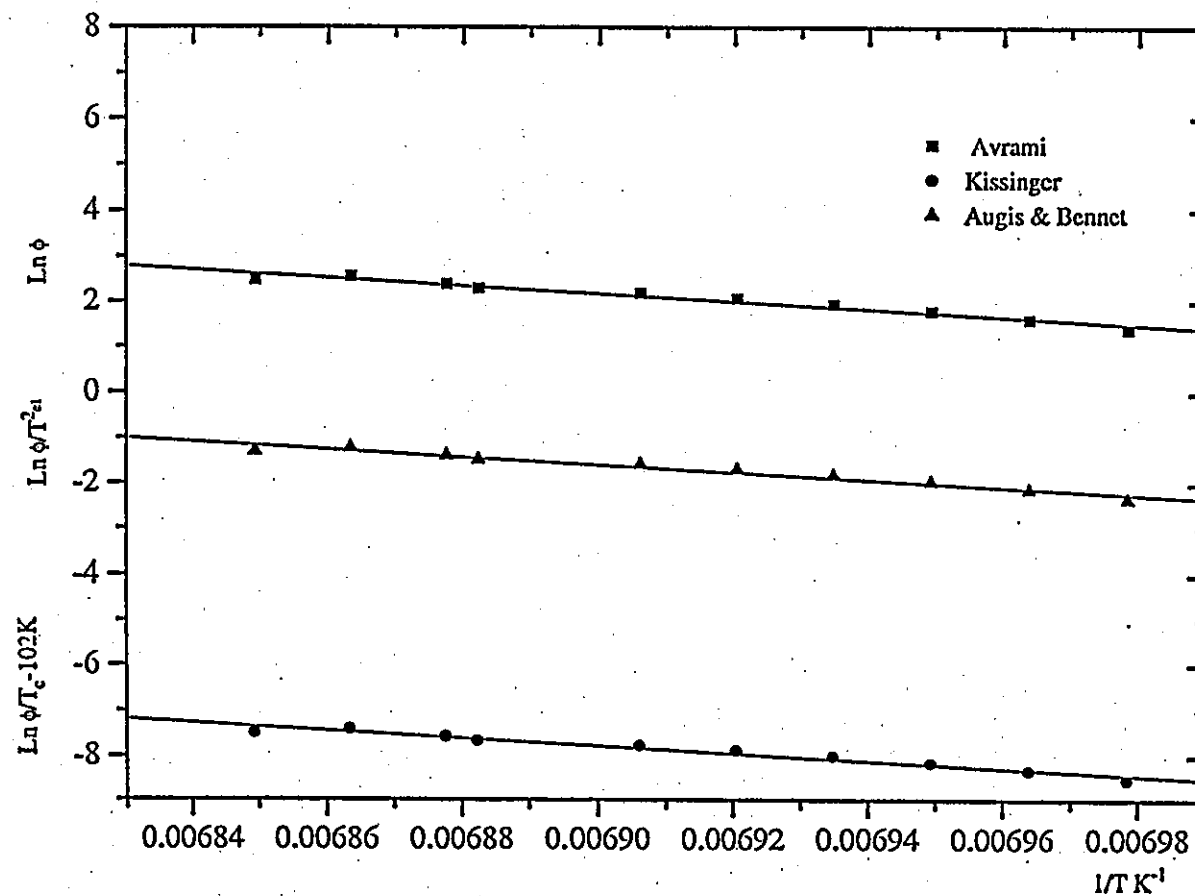


Fig. 4.14 Determination of activation energy E using Avrami, Kissinger and Augis & Bennet method for deuterated TMMB

